A study on positive electrode materials for sodium secondary batteries utilizing ionic liquids as electrolytes

Chih–Yao Chen

2014

Contents

Chapter 1

General introduction

1.1 Electrochemical energy storage

Stable supply of energy is currently a vital global issue given the continuous increase in the demand for fossil fuels and the finiteness of such non-renewable resources [1–3]. The present energy economy based on fossil fuel not only faces the future exhaustion but also the greenhouse gas problems leading global warming and series of serious climate changes. The environmental concerns over the use of fossil fuels and their finite resources have spurred society to reconsider the generation and use of electric energy in a more sustainable manner [1]. As a result, the deployment of renewable energy resources such as sun and wind as well as the development of electrified transportation with low CO_2 emissions are receiving ever-growing interest [4–7].

To compensate the intermittent nature of solar and wind power, energy storage systems are believed to play an essential part [1, 2]. Energy storage is a key enabler for the smooth integration of these renewable energy sources into the smart grid, providing electricity to electric vehicles, and improving grid reliability and utilization (see Fig. 1–1) [8, 9]. Several types of energy storage are proposed for large-scale stationary applications, namely mechanical, electrical, chemical and electrochemical storages [10, 11]. Among them, electrochemical methods based on batteries are attractive solutions due to their pollution-free operation, high round-trip efficiency, high energy density, simple maintenance and scalability [2, 10, 11].

Batteries are well-developed technologies and are at the forefront of electrochemical energy storage systems. Fig. 1–2, Table 1–1 and Table 1–2 show the technology

characteristics for batteries being considered for grid storage applications [1, 2]. Li-ion batteries (LIBs) significantly outperform other competing technologies in terms of gravimetric energy and power densities and cyclability [11–15]. Consequently, LIBs have dominated the market of portable electronic power source and the publication of battery research for the past two decades. LIB technology is now regarded as the battery of choice for transportation and stationary storage applications. However, Li resources are unevenly distributed and concentrated in South America, resulting in the risk of dependence on a single geographic area [16–18]. The anticipated astronomic demand for grid-scale applications worldwide will pose a certain challenge on it, raising concern for a possible shortage of Li resources and thus a staggering price increase, just as that faced today with fossil fuels. To loosen the dependence on LIB, there are increasing interests in developing alternative battery technologies, namely, post Li-ion batteries.

1.2 Sodium secondary batteries

Since Na positions just below Li in Group 1 of the periodic table, they share similar chemical properties. The even distribution and high abundance of Na resources across the world and consequent low cost compared to Li recommend Na secondary batteries as reasonable alternatives to LIBs. The comparison of selected properties for Na and Li is shown in Table 1–3.

1.2.1 High temperature sodium secondary batteries

Early research on Na-based batteries focused on high-temperature Na/S (NAS) and $Na/NiCl_2$ (ZEBRA) systems that utilize the beta-alumina solid electrolyte (BASE) [19–23]. Although Na/S and $Na/NiCl_2$ batteries have been commercialized, strict thermal management is indispensable for delivering satisfactory performance [24]. The sophisticated engineering

such as thermal sealing issues and the materials necessary for ensuring durability and safety during elevated-temperature operations (573–623 K) inflate the cost and decrease the total energy density of these batteries [25]. Nowadays, other electrolytes such as NASICON-type (Na-superionic conductors), ceramic and glass-ceramic electrolytes are also being investigated [23]. The recent trend of Na/S has been attempted to shift towards intermediate temperatures operation (*ca*. 373–443 K), though they are still in the early stage of development [23, 26].

1.2.2 Room temperature sodium secondary batteries

By applying a similar “rocking-chair” working principle, Na and Li secondary batteries employing non-aqueous electrolytes and intercalation chemistry have been initially explored in late 1970s and 1980s in parallel [27–30]. However, the commercial success of Li batteries spawned tremendous interest and shifted the focus of the battery community from Na. Research interest in room temperature Na secondary batteries recently has been resurrected, driven by the excellent potential for the development of affordable storage technologies, offering the prospect of lessening the dependence on LIBs [31–36]. In addition, since Na does not alloy with Al, lower cost Al current collectors can be used instead of Cu [32]. As a less expensive option, the development of Na-based batteries should accelerate the adoption of rechargeable batteries in large-scale applications. Moreover, the chemical similarity between Na and Li should facilitate cross-application of the huge body of knowledge regarding LIB technology. Most importantly, Na secondary batteries do not simply mirror the Li counterpart, but presents significant unexplored opportunity and possibility [31].

The principal concept of room temperature Na secondary batteries is illustrated in Fig. 1–3 [33]. A combination of a negative Na intercalation compound (negative electrode) with another Na intercalation compound (positive electrode) having a more positive redox

potential gives a Na ion transfer cell. The electrolyte is a pure ionic conductor that physically separates negative and positive electrodes. During charging, Na ions are extracted from the positive electrode while concurrent Na insertion occurs at the negative electrode. During the subsequent charge–discharge process the active Na ions are then shuttled between two electrodes. In sections 1.3–1.5, a brief review of recent development in positive and negative electrode materials as well as electrolytes is given.

1.3 Positive electrode materials

Na prefers 6-coordination, either in an octahedral or prismatic arrangement. There are the two major classes of positive electrode materials: layered oxides that have 2-D galleries to hold Na ions and polyanionic compounds that have octahedral interstitial sites available for Na accommodation [32].

1.3.1 Layered oxides

Layered oxides Na_xMO_2 (M = transition metal) have been most extensively investigated as positive electrode materials for Na secondary batteries because of the high capacity and simple synthesis [37–42]. The layered structure is built by sheet of edge-shared MO_6 octahedra, wherein Na ions are located between these sheets. The layer hosts are characterized by weak interlayer interactions, so that they possess structural flexibility to adapt the geometry of the intercalated guest species by free adjustment of interlayer separation. Na_xMO_2 can be categorized into two main groups using the notation designated by Delmas [43], the O3 and P2 phases. As shown in Fig. 1–4, they differ in the stacking of the oxygen layers (ABCABC for O3, and ABBA for P2) and hence the intercalation sites for Na ions (octahedral for O3 and prismatic for P2). The number 3 in O3 or 2 in P2 describes the number of transition metal (M) layers along the stacking direction in the unit cell. Through utilizing

the 3d transition metals as redox couples, $NaMnO_2$ [37], $NaCrO_2$ [39, 44, 45], $NaFeO_2$ [46], Na_xCoO_2 [38], and $NaNiO_2$ [47] have been explored so far.

In order to improve the electrochemical performance and structural stability, solid-solutions of Na_xMO_2 have been proposed [40–42, 48–51]. P2–$Na_{0.67}[Fe_{0.5}Mn_{0.5}]O_2$ and P2–$Na_{0.67}[Fe_{0.33}Mn_{0.66}]O_2$ provide the most promising electrochemical properties in terms of reversible capacity (*ca*. 190 mAh g^{-1}) and energy density (*ca*. 520 Wh kg^{-1}) for the cell operating at ambient temperatures [41, 50, 51]. However, less than 80% of initial capacity was retained after 30–40 cycles. Lately, Na-rich layered oxide prepared via delithiated Li-rich layered oxide ($0.5Li_2MnO_3 \cdot 0.5LiMn_{0.42}Ni_{0.42}Co_{0.16}O_2$) has been reported and claimed a high capacity of 234 mAh g^{-1} and high energy density (*ca*. 644 Wh kg^{-1}), though its cyclability is still insufficient [52]. On the other hand, O3–type layered oxides deliver moderate capacities of *ca*. 120 mAh g^{-1} but generally with better cyclability. The electrochemical properties of layered oxide positive electrodes described above are summarized in Table 1–4. Among them, O3–$NaCrO_2$ has been proved to possess good thermal stability even at charged state [44]. In light of these results, the author has focused on the electrochemical properties and structural variation of $NaCrO_2$ at elevated temperature (363 K), as only room temperature data is available in the literature. The results are presented in Chapter 3.

Layered oxides are widely regarded as the most plausible positive electrode candidate for Na secondary batteries. A recent computational work showed that the barriers for Na ion migration can potentially be lower than that for Li ion migration in the layered structures, revealing the enticing promise for such materials to be developed with improved kinetics [53]. However, many of those materials present complicated charge–discharge profiles accompanied with several phase transitions [37–40, 44–50], which are caused by Na-vacancy ordering and/or layer sliding [38]. Due to the competition between P and O type arrangements, the sodiation/desodiation behavior of the layered materials is not fully topotactic in many

cases [31]. Some of them have been shown to undergo an irreversible structural transition during electrochemical extraction of Na [40, 46 47, 50]. It is not clear yet to what extent these phase transitions may affect practical capacity and cyclability [54].

1.3.2 Phosphate-based polyanionic compounds

As documented in the literature, extensive research efforts have been devoted to polyanionic compounds for positive electrode materials for LIBs [14, 55–57]. Polyanionic compounds are a class of materials in which tetrahedral polyanion structure units $(XO_4)^{n-}$ (X = P, S, Si, As, Mo, or W) are combined with MO_x (M = transition metal) polyhedra. Since the oxygen atoms have strong covalent bond to X in $(XO_4)^{n-}$, such materials generally possess higher thermal stability compared to layered oxides. The considerable advantages in safety make them particularly suitable for large-scale applications [57, 58]. For Na secondary batteries, phosphates form a major class of polyanion-type electrode materials and most of them are capable of offering robust and open framework favoring facile Na ion transport [33–36].

Olivine $LiFePO_4$ is the most common polyanion-type electrode material for LIBs [55–57]. However, the thermodynamically stable Na equivalent, $NaFePO_4$, crystallizes in the maricite structure in which the sites for Na^+ and Fe^{2+} are just the opposite of those in olivine $LiFePO_4$. Maricite $NaFePO_4$ is known to be electrochemically inactive due to the lack of transport channel for Na ions [59, 60]. Meta-stable olivine $NaFePO_4$ phase has been prepared through electrochemical or chemical delithiation of $LiFePO_4$ and subsequent insertions of Na ions into $FePO_4$ [60–63]. Although olivine $NaFePO_4$ has the highest theoretical capacity (154 mAh g^{-1}) among phosphate-based electrode materials, the full capacity has not been realized. A practical capacity value of 125 mAh g^{-1} and an increase in polarization with cycling were reported [63]. It was suggested that olivine $NaFePO_4$ undergoes different reaction paths

during charging and discharging to accommodate local strains caused by the large mismatch between the end members (17.58% in volume) [61–63]. Such a large volume variation (more than twice that of $LiFePO_4$ (6.8%)) can result in inferior rate capability and cyclability. Amorphous $FePO_4$ can be directly synthesized as opposed to olivine $NaFePO_4$, delivering a capacity of *ca*. 120 mAh g^{-1} with a better cyclability [64, 65].

Pyrophosphates ($Na_2MP_2O_7$, M = transition metal) [66–75] have recently been recognized as promising active materials. The rich structural configuration for these compounds leads to several possible scaffolds for Na ion intercalation/deintercalation [33, 35]. For instance, pyrophosphate can be of layered ($Na_2CoP_2O_7$) or three-dimensional structure ($Na_2MnP_2O_7$) depending on the transition metal [68, 69]. Due to the low cost of components, $Na_2FeP_2O_7$ and its derivative $Na_{2-x}Fe_{1+x/2}P_2O_7$ ($0 < x < 0.44$) were first studied [66, 67, 70–72]. Unlike most of the other polyanion-type positive electrode materials, nanosizing and carbon coating are not necessarily required for $Na_2FeP_2O_7$ [66]. Uncoated and micron-sized $Na_2FeP_2O_7$ shows a capacity of approximately 90 mAh g^{-1} and good rate capability, which enables lowering the electrode processing cost [66, 67]. Moreover, $Na_2FeP_2O_7$ undergoes a topotactic Na intercalation/deintercalation reaction with a very small volume change (2.6%), which could provide a good stability during electrochemical cycling [67]. Furthermore, it was reported that $Na_2FeP_2O_7$ possesses good thermal stability up to 823 K even at charged state [67, 70]. Despite these impressive advantages, pyrophosphates have not yet been significantly explored as positive electrode materials for Na secondary batteries. There is still room for improvement because its theoretical capacity has not been fully realized and the practical cyclability remains unknown. Thus, the author has evaluated the charge–discharge behavior of $Na_{2-x}Fe_{1+x/2}P_2O_7$ (x = 0 and 0.44) over a wide temperature range (253–363 K for x = 0 and 298–363 K for x = 0.44) and their long-term cyclability. The results are presented in Chapters 4, 5, and 6.

It has been demonstrated that NASICON-type ($Na_3M_2(PO_4)_3$) compounds, originally proposed as solid electrolyte aiming at competing with beta-alumina [79], can be used as positive electrodes [76–78]. $Na_3V_2(PO_4)_2F_3$, one variant of NASICON compounds, recently has also been reported to be capable of delivering capacity of *ca*. 110 mAh g^{-1} along with good capacity retention [80–83]. However, such electrochemical properties can be achieved only for the vanadium-based NASICON. $Na_3Fe_2(PO_4)_2F_3$ shows an unsatisfactory capacity of 24 mAh g^{-1} [80]. Utilizing a multi-electron redox reaction and the high potential (3.8 V) of the tailored vanadium redox couple ($V^{3.8+}/V^{5+}$), $Na_{1.5}VPO_{4.8}F_{0.7}$ was reported to possess the high energy density of approximately 600 Wh kg^{-1} [84]. Nevertheless, since vanadium is considered as toxic element, these high-voltage electrode materials might be constrained for their practical applications [32]. Phosphate fluorides (Na_2MPO_4F) have recently emerged as a new choice of positive electrode materials for Na batteries [85–88]. Carbon coated Na_2FePO_4F and Na_2MnPO_4F are able to exchange one electron and deliver capacities of 110 and 120 mAh g^{-1}, respectively. However, the capacity of Na_2FePO_4F decays drastically with an increase in the current density [85].

Table 1–5 summarizes the electrochemical properties of phosphate-based positive electrode materials described. A large group of possible polyanion-type positive electrode materials for Na (Li) batteries has been systematically gathered in a recent publication [89].

1.3.3 Orthosilicate-based polyanionic compounds

The quest for new positive electrode materials with low cost and high capacity has promoted significant research efforts on orthosilicates (A_2MSiO_4; A = Li and Na) [89–93]. For LIBs, Li_2FeSiO_4 and Li_2MnSiO_4 offer the exciting possibility of realizing two-electron exchange per formula leading to a high theoretical capacity of *ca*. 330 mAh g^{-1} [92, 93]. To the author's knowledge, however, orthosilicates have not been explored for Na host matrix.

One of the peculiarities of these materials is the poor intrinsic conductivity. To facilitate ion and electron transports, some of the electrochemical data reported were recorded at intermediate temperatures (318–333 K) [91–93]. Recently, Na_2MnSiO_4 has been prepared and used as the starting material to obtain a metastable polymorph of Li_2MnSiO_4 via ion exchange, though no electrochemical data on Na cell were reported [94]. Inspired by such findings, the author has investigated the feasibility of orthosilicates as Na storage material at 298–363 K. The results are presented in Chapter 7.

1.4 Negative electrode materials

Since the present thesis does not focus on negative electrodes, only two major kinds of materials, carbon and alloy materials, are described here. In the field of LIBs, carbon materials are considered to be a mature, well-understood technology [95]. Unlike for LIBs, however, graphitic carbons are not applicable for Na secondary batteries since Na atoms are not intercalated between the graphite layers to any appreciable extent (~NaC_{70}) [95–98]. Lately, many other non-graphitic carbonaceous materials have been shown to insert Na, such as petroleum cokes [99], carbon black [100], soft carbons (small crystalline domains of ordered graphene) [95] and hard carbons (disordered with nanoscale porosity) [95, 96, 101–103]. Hard carbons are the most studied one and are regarded as the first-generation negative electrodes of choice, having capacities of 200–300 mAh g^{-1}.

During the initial Na intercalation process, part of Na reacts with the components of electrolyte to form an electronically insulating but ionically conductive layer at the surface of carbon electrodes, which is known as the solid electrolyte interface (SEI) [95]. This SEI formation is one of the primary contributors to irreversible capacity for carbon electrodes. Irreversible capacity should be as small as possible because this charge loss needs to be compensated by additional positive electrode materials in a practical cell [104].

Nanostructured carbon materials have been introduced for Na storage and the improved capacities and kinetics have been reported [105, 106]. However, problems of irreversible capacity and unsatisfactory coulombic efficiency make them difficult for practical applications. The large surface area of nanostructured materials is considered to be the main reason for the severe side reactions [33].

Storing Na through an alloy reaction has been proposed because of the high theoretical capacity compared to that based on intercalation reaction. A number of materials such as Sn [107], Sn/Cu [108], Sn/C [109], SnO_2/graphene [110], Sb/C [111], and SnSb/C [112] have attracted interest. Among them, nanocomposites of SnO_2/graphene and Sb/C and can deliver large reversible capacities of 600–700 mAh g^{-1} with good cyclability over 100 cycles [110, 111]. Recently, amorphous red phosphorous/carbon composite has been demonstrated to show a reversible capacity of 1890 mAh g^{-1} (~$Na_{2.18}P$), which is the highest value among negative electrodes for Na batteries reported to date [113]. For these composites, carbon matrix is considered to be indispensable because it provides a conductive and buffering matrix for effective release of mechanical stress caused by Na insertion/extraction [111]. In spite of the high capacity of alloy compounds, their practical applications are still challenging, because the significant volume change upon alloying-dealloying leads to the instability of the electrode, which is a common issue in LIBs [31, 98].

1.5 Electrolytes

Electrolytes play a fundamental role in terms of the electrochemical properties and the safety of batteries [115–117]. However, since Na secondary battery is an emerging technology, kinds of electrolytes which enable Na electrochemistry and investigation on this field are relatively limited [118–120]. In order to deliver the expected performance, the following requirements should be met [23, 115–117]; (i) high ionic conductivity (σ > 1 mS cm^{-1}) to

reduce the resistance polarization effect in a battery; (ii) high thermal stability for operation in a wide temperature range; (iii) physical and chemical compatibility with the electrodes; (iv) low toxicity and high safety. Three types of electrolytes for Na secondary batteries are described in this section.

1.5.1 Organic electrolytes

Conventional electrolytes consist of either $NaClO_4$ or $NaPF_6$ as salts and carbonate-based solvents such as ethylene carbonate (EC), propylene carbonate (PC) and dimethyl carbonate (DMC). The most common formulation is 1 mol dm^{-3} $NaClO_4$ in PC, because PC possesses a wider liquid range compared with EC and other linear alkyl carbonates [102, 116]. These solutions offer high ionic conductivities and low viscosities and are compatible with the operation voltage of Na secondary batteries. For negative electrodes, the use of SEI forming additive like fluoroethylene carbonate (FEC) [121] is important in order to control the surface reaction between the electrode and the electrolyte, as demonstrated in recent advances [107, 111, 113].

Although comprehensive characterization and testing have proven that hard carbon is the primary candidate for negative electrodes, its electrochemical performance shows a strong dependence on the electrolytes [102, 118, 119]. Moreover, the Na intercalated hard carbon (Na_xC_6) exhibits higher reactivity toward organic electrolytes compared with Li_xC_6, which raises imperative concerns about the stability of the organic electrolyte [122]. Formation of Na metallic dendrites on the negative electrode during charge also leads to a serious issue, because the high reactivity of Na metal with organic electrolytes and its low melting point (371 K) further put the safety into question [32, 98].

1.5.2 Aqueous electrolytes

Aside from the organic electrolytes, development of aqueous Na secondary batteries is another perspective in specific applications wherein cost is the main concern [33]. For instance, inexpensive inorganic Na salt such as Na_2SO_4 and $NaNO_3$ can be used [123–125]. Moreover, aqueous electrolytes have much higher ionic mobility than organic solvents. These systems provide high power, high efficiency, and superior cycle life. Nevertheless, the lower potential range of water constraints the possible cell voltage and thus the energy density (30–45 Wh kg^{-1}) [33, 35].

1.5.3 Ionic liquid electrolytes

Ionic liquids (ILs), entirely composed of ions, have attracted great interest because of their advantages against organic solvents such as nonflammability, non-detectable vapor pressure, good chemical, electrochemical and thermal stabilities [126–128]. ILs are characterized as task-specific reaction media and provide several attractive properties when exploited as electrolytes for secondary batteries. Their merits include (i) an inherent good thermal stability and wide liquid range that enable the device to operate in extreme temperature conditions; (ii) nonflammability that provides high safety; and (iii) nonvolatility that prevents the electrolyte from drying or generating pressure at elevated temperatures. Since most research efforts from the scientific community have targeted electrode materials, the adoption of ionic liquid electrolytes for Na secondary batteries received less attention [129–131].

Hagiwara *et al*. have investigated a series of ILs based on bis(fluorosulfonyl)amide (FSA) anions and bis(trifluoromethylsulfonyl)amide (TFSA) anions for battery applications at 340–440 K [132–135]. For instance, the Na[FSA]–K[FSA] system is suitable for Na battery operating around 363 K [136–138], while the Na[TFSA]–Cs[TFSA] system can be employed

at 423 K [139]. In contrast to conventional ILs that usually contain expensive organic cations, Na[FSA] and K[FSA] are simple inorganic compounds. It should be noted that, unlike TFSA salts, FSA salts can be synthesized without the costly electrochemical fluorination process. Thus, FSA salts are well expected to be produced at a reasonably low price in the near future. Recently, the Na[FSA]–[C_3C_1pyrr][FSA] (C_3C_1pyrr = *N*-methyl-*N*-propylpyrrolidinium) IL has been proposed because of the low melting point (264 K), high conductivity, and good thermal stability of [C_3C_1pyrr][FSA] [140]. The structures of FSA anion and C_3C_1pyrr cation are shown in Fig. 1–5. It has been demonstrated that the Na[FSA]–[C_3C_1pyrr][FSA] (20:80 molar ratio) exhibit an electrochemical window of 5.2 V and an ionic conductivity of 15.6 mS cm^{-1} at 353 K [141]. By utilizing this IL as an electrolyte, good electrochemical properties have been obtained for $NaCrO_2$ positive electrode over 298–353 K [141] and hard carbon negative electrodes at 363 K [142].

1.6 Aims of this study

As concluded by a recent review, the greatest technical bottlenecks for Na electrochemical systems to overcome are the lack of high-performance electrode and electrolyte materials that are easy to synthesize, safe, long-lasting, and are of reasonable cost [32]. Therefore, the present study is aiming at developing economic positive electrode materials, and investigating their electrochemical properties in intrinsically safe ionic liquid electrolytes.

In Chapter 3, electrochemical properties and structural variation of a layered oxide $NaCrO_2$ are investigated in the Na[FSA]–K[FSA] IL at 363 K, with the objective of understanding the sodiation/desodiation mechanism. The obtained results are compared with previous reports in which conventional organic electrolytes were employed at room temperature.

In Chapter 4, the charge–discharge behavior and long term cyclability of phosphate-based polyanionic compound $Na_2FeP_2O_7$ are evaluated in the Na[FSA]–K[FSA] IL at 363 K. The mechanism of Na extraction from $Na_2FeP_2O_7$ is also studied by ex-situ X-ray absorption spectroscopy (XAS).

In Chapters 5, the charge–discharge behavior of $Na_2FeP_2O_7$ is investigated in the Na[FSA]–[C_3C_1pyrr][FSA] IL at 253–363 K. The purpose of this chapter is to evaluate the viability of the IL electrolyte for wide-temperature Na secondary battery applications. The temperature dependence of the rate capability and cyclability is also examined.

In Chapter 6, electrochemical properties of $Na_{1.56}Fe_{1.22}P_2O_7$ are investigated using Na[FSA]–[C_3C_1pyrr][FSA] IL at 298–363 K. The obtained results are compared with that of $Na_2FeP_2O_7$ to understand the effect of tailoring the Na/Fe stoichiometric ratio of a polyanion-type positive electrode.

In Chapter 7, the feasibility of orthosilicate-based polyanionic compound Na_2MnSiO_4 as Na storage material is assessed using the Na[FSA]–[C_3C_1pyrr][FSA] IL electrolyte. The structural variation and thermal stability of this material are also evaluated.

References

[1] Z.G. Yang, J.L. Zhang, M.C.W. Kintner-Meyer, X.C. Lu, D.W. Choi, J.P. Lemmon, J. Liu, Chem. Rev. 111 (2011) 3577–3613.

[2] B. Dunn, H. Kamath, J.M. Tarascon, Science 334 (2011) 928–935.

[3] J. Liu, J.G. Zhang, Z.G. Yang, J.P. Lemmon, C. Imhoff, G.L. Graff, L.Y. Li, J.Z. Hu, C.M.Wang, J. Xiao, G. Xia, V.V. Viswanathan, S. Baskaran, V. Sprenkle, X.L. Li, Y.Y. Shao, B. Schwenzer, Adv. Funct. Mater. 23 (2013) 929–946.

[4] J.P. Holdren, Science 315 (2007) 737–737.

[5] P. Simon, Y. Gogotsi, Nat. Mater. 7 (2011) 845–854.

[6] T.R. Cook, D.K. Dogutan, S.Y. Reece, Y. Surendranath, T.S. Teets, D.G. Nocera, Chem. Rev. 110 (2010) 6474–6502.

[7] D. Ginley, M.A. Green, R. Collins, MRS Bull. 33 (2008) 355–364.

[8] J. Tollefson, Nature 456 (2008) 436–440.

[9] E. Marris, Nature 454 (2008) 570–573.

[10] M. Winter, R.J. Brodd, Chem. Rev. 104 (2004) 4245–4269.

[11] G.L. Soloveichik, Annu. Rev. CHem. Biomol. Eng. 2 (2011) 503–527.

[12] V. Etacheri, R. Marom, R. Elazari, G. Salitra, D. Aurbach, Energy Environ. Sci. 4 (2011) 3243–3262.

[13] J.B. Goodenough, Y. Kim, Chem. Mater. 22 (2010) 587–603.

[14] J.M. Tarascon, M. Armand, Nature 414 (2001) 359–367.

[15] B. Scrosati, J. Hassoun, Y.K. Sun, Energy Environ. Sci. 4 (2011) 3287–3295.

[16] J.M. Tarascon, Nat. Chem. 2 (2010) 510–510.

[17] W. Tahil, The Trouble with Lithium: Implications of Future PHEV Production for Lithium Demand (Meridian International Research, 2007). http://go.nature.com/jhDqLH

[18] W. Tahil, The Trouble with Lithium 2: Under the Microscope (Meridian International Research, 2006). http://go.nature.com/AWITRo

[19] Y.F.Y. Yao, J.T. Kummer, J. Inorg. Nucl. Chem. 29 (1967) 2453–2475.

[20] J.L. Sudworth, J. Power Sources 11 (1984) 143–154.

[21] J. Coetzer, J. Power Sources 18 (1986) 377–380.

[22] C.H. Dustmann, J. Power Sources 127 (2004) 85–92.

[23] K.B. Hueso, M. Armand, T. Rojo, Energy Environ. Sci. 6 (2013) 734–749.

[24] X.C. Lu, G.G. Xia, J.P. Lemmon, Z.G. Yang, J. Power Sources 195 (2010) 2431–2442.

[25] S.F Song, Z.Y. Wen, Y. Liu, J. Lin, X.G. Xu, Q.X. Zhang, J. Solid State Electrochem. 14 (2010) 1735–1740.

[26] X.C. Liu, B.W. Kirby, W. Xu, G.S. Li, J.Y. Kim, J.P. Lemmon, V.L. Sprenkle, Z.G. Yang, Energy Environ. Sci. 6 (2013) 299–306.

[27] M.S. Whittingham, Prog. Solid State Chem. 12 (1978) 41–99.

[28] K.M. Abraham, Solid State Ionics 7 (1982) 199–212.

[29] C. Delmas, JJ. Braconnier, C. Fouassier, P. Hagenmuller, Solid State Ionics 3–4 (1983) 165–169.
[30] J.M. Tarascon, G.W. Hull, Solid State Ionics 22 (1986) 85–96.
[31] S.W. Kim, D.H. Seo, X.H. Ma, G. Ceder, K. Kang, Adv. Energy Mater. 2 (2012) 710–721.
[32] M.D. Slater, D. Kim, E. Lee, C.S. Johnson, Adv. Funct. Mater. 23 (2013) 947–958.
[33] H.L. Pan, Y.S. Hu, L.Q. Chen, Energy Environ. Sci. 6 (2013) 2338–2360.
[34] B.L. Ellis, L.F. Nazar, Curr. Opin, Solid State Mater. Sci. 16 (2012) 168–177.
[35] V. Palomares, M. Casas-Cabanas, E. Castillo-Martinez, M.H. Han, T. Rojo, Energy Environ. Sci. 6 (2013) 2312–2337.
[36] V. Palomares, P. Serras, I. Villaluenga, K.B. Hueso, J. Carretero-Gonzalez, T. Rojo, Energy Environ. Sci. 5 (2012) 5884–5901.
[37] X.H. Ma, H.L. Chen, G. Ceder, J. Electrochem. Soc. 158 (2011) A1307–A1312.
[38] R. Berthelot, D. Carlier, C. Delmas, Nat. Mater. 10 (2011) 74–80.
[39] S. Komaba, C. Takei, T. Nakayama, A. Ogata, N. Yabuuchi, Electrochem. Commun. 12 (2012) 355–358.
[40] S. Komaba, N. Yabuuchi, T. Nakayama, A. Ogata, T. Ishikawa, I. Nakai, Inorg. Chem. 51 (2012) 6211–6220.
[41] N. Yabuuchi, M. Kajiyama, J. Iwatate, H. Nishikawa, S. Hitomi, R. Okuyama, R. Usui, Y. Yamada, S. Komaba, Nat. Mater. 11 (2012) 512–517.
[42] J. Billaud, G. Singh, A.R. Armstrong, E. Gonzalo, V. Roddatis, M. Armand, T. Rojob, P.G. Bruce, Energy Environ. Sci. 7 (2014) 1387–1391.
[43] C. Delmas, C. Fouassier, P. Hagenmuller, Physica B & C 99 (1980) 81–85.
[44] X.Xia, J.R. Dahn, Electrochem. Solid State Lett. 15 (2012) A1–A4.
[45] J.J. Ding, Y.N. Zhou, Q. Sun, Z.W. Fu, Electrochem. Commun. 22 (2012) 85–88.
[46] N. Yabuuchi, H. Yoshida, S. Komaba, Electrochemistry 80 (2012) 716–719.
[47] P. Vassilaras, X.H. Ma, X. Li, G. Ceder, J. Electrochem. Soc. 160 (2013) A207–A211.
[48] M. Sathiya, K. Hemalatha, K. Ramesha, J.M. Tarascon, A.S. Prakash, Chem. Mater. 24 (2012) 1846–1853.
[49] H. Yoshida, N. Yabuuchi, S. Komaba, Electrochem. Commun. 34 (2013) 60–63.
[50] B.M. de Boisse, D. Carlier, M. Guignard, C. Delmas, J. Electrochem. Soc. 160 (2013) A569–A574.
[51] J. Zhao, J. Xu, D.H. Lee, N. Dimov, Y.S. Meng, S. Okada, J. Power Sources 264 (2014) 235–239.
[52] Z. L. Jian, H.J. Yu, H.S. Zhou, Electrochem. Commun. 34 (2013) 215–218.
[53] S.P. Ong, V.L. Chevrier, G. Hautier, A. Jain, C. Moore, S. Kim, X.H. Ma, G. Ceder, Energy Environ. Sci. 4 (2011) 3680–3688.
[54] H.L. Chen, Q. Hao, O. Zivkovic, G. Hautier, L.S. Du, Y.Z. Tang, Y.Y. Hu, H.X. Ma, C.P. Grey, G. Ceder, Chem. Mater. 25 (2013) 2777–2786.
[55] A.K. Padhi, K.S. Nanjundaswamy, J.B. Goodenough, J. Electrochem. Soc. 144 (1997) 1188–1194.
[56] A.K. Padhi, K.S. Nanjundaswamy, C. Masquelier, S. Okada, J.B. Goodenough, J. Electrochem. Soc. 144 (1997) 1609–1613.

[57] Z.L. Gong, Y. Yang, Energy Environ. Sci. 4 (2011) 3223–3242.
[58] J. Xu, D.H. Lee, Y.S. Meng, Funct. Mater. Lett. 6 (2013) 1330001–1–1330001–7.
[59] B.L. Ellis, W.R.M. Makahnouk, Y. Makimura, K. Toghill, L.F. Nazar, Nat. Mater. 6 (2007) 749–753.
[60] K. Zaghib, J. Trottier, P. Hovington, F. Brochu, A. Guerfi, A. Mauger, C.M. Julien, J. Power Sources 196 (2011) 9612–9617.
[61] P. Moreau, D. Guyomard, J. Gaubicher, F. Boucher, Chem. Mater. 22 (2010) 4126–4128.
[62] M. Casas-Cabansa, V.V. Roddatis, D. Saurel, P. Kubiak, J. Carretero-Gonzalez, V. Palomares, P. Serras, T. Rojo, J. Mater. Chem. 22 (2012) 17421–17423.
[63] S.M. Oh, S.T. Myung, J. Hassoun, B. Scrosati, Y.K. Sun, Electrochem. Commun. 22 (2012) 149–152.
[64] T. Shiratsuchi, S. Okada, J. Yamaki, T. Nishida, J. Power Sources 159 (2006) 268–271.
[65] Y.L. Liu, Y.H. Xu, X.G. Han, C. Pallegrinelli, Y.J. Zhu, H.L. Zhu, J.Y. Yang, A.C. Chung, O. Vaaland, C.S. Wang, L.B. Hu, Nano. Lett. 12 (2012) 5664–5668.
[66] P. Barpanda, T. Ye, S. Nishimura, S.C. Chung, Y. Yamada, M. Okubo, H.S. Zhou, A. Yamada, Electrochem. Commun. 24 (2012) 116–119.
[67] P. Barpanda, G. Liu, C.D. Ling, M. Tamaru, M. Avdeev, S.C. Chung, Y. Yamada, A. Yamada, Chem. Mater. 25 (2013) 3480–3487.
[68] P. Barpanda, T. Ye, M. Avdeev, S.C. Chung, A. Yamada, J. Mater. Chem. A 1 (2013) 4194–4197.
[69] P. Barpanda, J.C. Lu, T. Ye, M. Kajiyama, S.C. Chung, N. Yabuuchi, S. Komaba, A. Yamada, RSC Adv. 3 (2013) 3857–3860.
[70] H. Kim, R.A. Shakoor, C. Park, S.Y. Lim, J.S. Kim, W. Cho, K. Miyasaka, R. Kahraman, Y. Jung, J. W. Choi, Adv. Funct. Mater. 23 (2013) 1147–1155.
[71] K.H. Ha, S.H. Woo, D. Mok, N.S. Choi, Y. Park, S.M. Oh, Y. Kim, J. Kim, J. Lee, L.F. Nazar, K.T. Lee, Adv. Energy Mater. 3 (2013) 770–776.
[72] T. Honma, N. Ito, T. Togashi, A. Sato, T. Komatsu, J. Power Sources 227 (2013) 31–34.
[73] P. Barpanda, S. Nishimura, A. Yamada, Adv. Energy Mater. 2 (2012) 841–859.
[74] H. Kim, I. Park, D.H. Seo, S. Lee, S.W. Kim, W.J. Kwon, Y.U. Park, C.S. Kim, S. Jeon, K. Kang, J. Am. Chem. Soc. 134 (2012) 10369–10372.
[75] H. Kim, I. Park, S. Lee, H. Kim, K.Y. Park, Y.U. Park, H. Kim, J. Kim, H.D. Lim, W.S. Yoon, K.Kang, Chem. Mater. 25 (2013) 3614–3622.
[76] K. Saravanan, C.W. Mason, A. Rudola, K.H. Wong, P. Balaya, Adv. Energy Mater. 3 (2013) 444–450.
[77] Z.L. Jian, W.Z. Han, X. Lu, H.X. Yang, Y.S. Hu, J. Zhou, Z.B. Zhou, J.Q. Li, W. Chen, D.F. Chen, L.Q. Chen, Adv. Energy Mater. 3 (2013) 156–160.
[78] Y.H. Jung, C.H. Lim, D.K. Kim, J. Mater. Chem. A 1 (2013) 11350–11354.
[79] J.B. Goodenough, H.Y. Hong, J.A. Kafalas, Mater. Res. Bull. 11 (1976) 203–220.
[80] K. Chihara, A. Kitajou, I.D. Gocheva, S. Okada, J. Yamaki, J. Power Sources 227 (2013) 80–85.
[81] P. Serras, V. Palomares, A. Goni, I.G. de Muro, P. Kubiak, L. Lezama, T. Rojo, J. Mater. Chem. 22 (2012) 22301–22308.
[82] R.A. Shakoor, D.H. Seo, H. Kim, Y.U. Park, J. Kim, S.W. Kim, H. Gwon, S. Lee, K. Kang, J. Mater.

Chem. 22 (2012) 20535–20541.

[83] W.S. Cong, X.B. Ji, Z.P. Wu, Y.C. Yang, Z. Zhou, F.Q. Li, Q.Y. Chen, C.E. Banks, J. Power Sources 256 (2014) 258–263.

[84] Y.U. Park, D.H. Seo, H.S. Kwon, B. Kim, J. Kim, H. Kim, I. Kim, H.I. Yoo, K. Kang, J. Am. Chem. Soc. 135 (2013) 13870–13878.

[85] Y. Kawabe, N. Yabuuchi, M. Kajiyama, N. Fukuhara, T. Inamasu, R. Okuyama, I. Nakai, S. Komaba, Electrochem. Commun. 13 (2011) 1225–1228.

[86] S.W. Kim, D.H. Seo, H. Kim, K.Y. Park, K. Kang, Phys. Chem. Chem. Phys. 14 (2012) 3299–3303.

[87] A. Langrock, Y.H. Xu, Y.H. Liu, S. Ehrman, A. Manivannan, C.S. Wang, J. Power Sources 223 (2013) 62–67.

[88] N. Recham, J.N. Chotard, L. Dupont. K. Djellab, M. Armand, J.M. Tarascon, J. Electrochem. Soc. 156 (2009) A993–A999.

[89] C. Masquelier, L. Croguennec, Chem. Rev. 113 (2013) 6552–6591.

[90] R. Dominko, M. Bele, M. Gaberscek, A. Meden, M. Remskar, J. Jamnik, Electrochem. Commun. 8 (2006) 217–222.

[91] A. Nyten, A. Abouimrane, M. Armand, T. Gustafsson, J.O. Thomas, Electrochem. Commun. 7 (2005) 156–160.

[92] T. Muraliganth, K.R. Stroukoff, A. Manthiram, Chem. Mater. 22 (2010) 5754–5761.

[93] D. Rangappa, K.D. Murukanahally, T. Tomai, A. Unemoto, I. Honma, Nano Lett. 12 (2012) 1146–1151.

[94] H. Duncan, A. Kondamreddy, P.H.J. Mercier, Y. Le Page, Y. Abu-Lebdeh, M. Couillard, P.S. Whitfield, I.J. Davidson, Chem. Mater. 23 (2011) 5446–5456.

[95] D.A. Stevens, J.R. Dahn, J. Electrochem. Soc. 148 (2001) A803–A811.

[96] D.A. Stevens, J.R. Dahn, J. Electrochem. Soc. 147 (2000) A1271–A1273.

[97] G.E. Pascal, M. Fouletier, Solid State Ionics 28 (1988) 1172–1175.

[98] V.L. Chevrier, G. Ceder, J. Electrochem. Soc. 158 (2011) A1011–A1014.

[99] M.M. Doeff, Y.P. Ma, S.J. Visco, L.C. Dejonghe, J. Electrochem. Soc. 140 (1993) L169–L179.

[100] R. Alcantara, J.M. Jimenez-Mateos, P. Lavela, J.L. Tirado, Electrochem. Commun. 3 (2001) 639–642.

[101] P. Thomas, D. Billaud, Electrochim. Acta 47 (2002) 3303–3307.

[102] S. Komaba, W. Murata, T. Ishikawa, N. Yabuuchi, T. Ozeki, T. Nakayama, A. Ogata, K. Gotoh, K. Fujiwara, Adv. Funct. Mater. 21 (2011) 3859–3867.

[103] K. Gotoh, T. Ishikawa, S. Ishikawa, S. Shimadzu, N. Yabuuchi, S. Komaba, K. Takeda, A. Goto, K. Deguchi, S. Ohki, H. Hashi, T. Shimizu, H. Ishida, J. Power Sources 225 (2013) 137–140.

[104] S. Wenzel, T. Hara, J. Janek, P. Adelhelm, Energy Environ. Sci. 4 (2011) 3342–3345.

[105] K. Tang, L.J. Fu, R.J. White, L.H. Yu, M.M. Titirici, M. Antonietti, J. Maier, Adv. Energy Mater. 2 (2012) 873–877.

[106] Y.L. Cao, L.F. Xiao, M.L. Sushko, W. Wang, B. Schwenzer, J. Xiao, Z.M. Nie, L.V. Saraf, Z.G. Yang,

J. Liu, Nano. Lett. 12 (2012) 3783–3787.

[107] S. Komaba, Y. Matsuura, T. Ishikawa, N. Yabuuchi, W. Murata, S. Kuze, Electrochem. Commun. 21 (2012) 65–68.

[108] Y.M. Lin, P.R. Abel, A. Gupta, J.B. Goodenough, A. Heller, C.B. Mullins, ACS. Appl. Mater. Interfaces 5 (2013) 8273–8277.

[109] Y.H. Xu, Y.J. Zhu, Y.H. Liu, C.S. Wang, Adv. Energy Mater. 3 (2013) 128–133.

[110] D.W. Su, H.J. Ahn, G.X. Wang, Chem. Commun. 49 (2013) 3131–3133.

[111] L. Wu, X.H. Hu, J.F. Qian, F. Pei, F.Y. Wu, R.J. Mao, X.P Ai, H.X. Yang, Y.L. Cao, Energy Environ. Sci. 7 (2014) 323–328.

[112] L.F. Xiao, Y.L. Cao, J. Xiao, W. Wang, L. Kovarik, Z.M. Nie, J. Liu, Chem. Commun. 48 (2012) 3321–3323.

[113] Y. Kim, Y. Park, A. Choi, N.S. Choi, J. Kim, J. Lee, J.H. Ryu, S.M. Oh, K.T. Lee, Adv. Mater. 25 (2013) 3045–3049.

[114] A. Darwiche, C. Marino, M.T. Sougrati, B. Fraisse, L. Stievano, L. Monconduit, J. Am. Chem. Soc. 134 (2012) 20805–20811.

[115] J.B. Goodenough, Y. Kim, Chem. Mater. 22 (2010) 587–603.

[116] D. Yaakov, Y. Gofer, D. Aurbach, I.C. Halalay, J. Electrochem. Soc. 157 (2010) A1383–A1391.

[117] K. Xu, Chem. Rev. 104 (2004) 4303–4417.

[118] A. Ponrouch, E. Marchante, M. Courty, J.M. Tarascon, M.R. Palacin, Energy Environ. Sci. 5 (2012) 8572–8583.

[119] A. Ponrouch, R. Dedryvere, D. Monti, A.E. Demet, J.M.A. Mba, L. Croguennec, C. Masquelier, P. Johansson, M.R. Palacin, Energy Environ. Sci. 6 (2013) 2361–2369.

[120] K. Kuratani, N. Uemura, H. Senoh, H.T. Takeshita, T. Kiyobayashi, J. Power Sources 223 (2013) 175–182.

[121] S. Komaba, T. Ishikawa, N. Yabuuchi, W. Murata, A. Ito, Y. Ohsawa, ACS. Appl. Mater. Interfaces 3 (2011) 4165–4168.

[122] X. Xia, M.N. Obrovac, J.R. Dahn, Electrochem. Solid-State Lett. 14 (2011) A130–A130.

[123] J.F. Whitacre, A. Tevar, S. Sharma, Electrochem. Commun. 12 (2010) 463–466.

[124] Z. Li, D. Young, K. Xiang, W.C. Carter, Y.M. Chiang, Adv. Energy Mater. 3 (2013) 290–294.

[125] C.D. Wessells, S.V. Peddada, R.A. Huggins, Y. Cui, Nano Lett. 11 (2011) 5421–5425.

[126] M. Armand, F. Endres, D.R. MacFarlane, H. Ohno, B. Scrosati, Nat. Mater. 8 (2009) 621–629.

[127] M. Galinski, A. Lewandowski, I. Stepniak, Electrochim. Acta 51 (2006) 5567–5580.

[128] S. Passerini, G.B. Appetecchi, MRS Bull. 38 (2013) 540–547.

[129] L.G. Chagas, D. Buchholz, L.M. Wu, B. Vortmann, S. Passerini, J. Power Sources 247 (2014) 377–383.

[130] D. Monti, E. Jonsson, M.R. Palacin, P. Johansson, J. Power Sources 245 (2014) 630–636.

[131] N. Wongittharom, T.C. Lee, C.H. Wang, Y.C. Wang, J.K. Chang, J. Mater. Chem. A 2 (2014) 5655–5661.

[132] K. Kubota, T. Nohira, T. Goto, R. Hagiwara, Electrochem. Commun. 10 (2008) 1886–1888.

[133] K. Kubota, T. Nohira, R. Hagiwara, J. Chem. Eng. Data 55 (2010) 3142–3146.

[134] K. Kubota, T. Nohira, R. Hagiwara, Electrochim. Acta 66 (2012) 320–324.

[135] R. Hagiwara, K. Tamaki, K. Kubota, T. Goto, T. Nohira, J. Chem. Eng. Data 53 (2008) 355–358.

[136] A. Fukunaga, T. Nohira, Y. Kozawa, R. Hagiwara, S. Sakai, K. Nitta, S. Inazawa, J. Power Sources 209 (2012) 52–56.

[137] T. Yamamoto, T. Nohira, R. Hagiwara, A. Fukunaga, S. Sakai, K. Nitta, S. Inazawa, J. Power Sources 217 (2012) 479–484.

[138] T. Yamamoto, T. Nohira, R. Hagiwara, A. Fukunaga, S. Sakai, K. Nitta, S. Inazawa, J. Power Sources 237 (2013) 98–103.

[139] T. Nohira, T. Ishibashi, R. Hagiwara, J. Power Sources 205 (2012) 506–509.

[140] Q. Zhou, W.A. Henderson, G.B. Appetecchi, M. Montanino, S. Passerini, J. Phys. Chem. B 112 (2008) 13577–13580.

[141] C.S. Ding, T. Nohira, K. Kuroda, R. Hagiwara, A. Fukunaga, S. Sakai, K. Nitta, S. Inazawa, J. Power Sources 238 (2013) 296–300.

[142] A. Fukunaga, T. Nohira, R. Hagiwara, K. Numata, E. Itani, S. Sakai, K. Nitta, S. Inazawa, J. Power Sources 246 (2014) 387–391.

Table 1–1 The comparison of energy and power characteristics of potential batteries for grid-scale energy storage applications [1, 2].

Battery type	Voltage Range (V)	Operating Temp. (K)	Energy Density (Wh/L)	Specific Energy (Wh/kg)	Specific Power (W/kg)	Cyclability
Lithium ion $LiCoO_2$–C	2.5–4.2	248–313	200–250	120–160	200–300	300–1000
Lithium ion $LiFePO_4$–C	2.5–3.5	248–313	120–150	80–90	200–300	1500–2000
Lithium metal–polymer	2.4–4.0	-	100–110	100–110	130–170	600
Sodium–sulfur	1.8–2.1	573–623	70–150	60–120	15–70	4000
Sodium–metal chloride	2.6	573–623	20–140	50–100	30–150	3000
Lead acid	1.8–2.1	233–333	60–75	30–40	60–110	100–500
Nickel–cadmium	0.8–1.3	263–318	130–150	40–60	40–100	2000
Nickel–metal hydride	0.9–1.3	-	250–300	70–100	70–200	1000
Vanadium redox flow	1.1–1.6	283–313	10–20	10–20	1–4	5000

Table 1–2 Main applications, advantages and limitations of different battery technologies [3, 23].

Battery type	Main application	Advantages	Limitations
Lithium ion	Transportation and portable electronics, targets grid-scale storage	High efficiency High energy density High power	High cost (~\$700 kWh^{-1}) Safety/reliability problems Small temperature range of operation
Sodium–sulfur Sodium–metal chloride	Targets grid-scale storage	High efficiency High energy density	Operating at 573–623 K High production cost Weight and size specification Safety and durability concerns due to fracture of beta-alumina and molten sodium electrode
Lead acid	Current automobile and industrial application, backup power	Least expensive	Short cycle life High maintenance Low energy density
Redox flow	Targets grid-scale storage	MW storage system Potential long cycle life	High cost Unknown long term durability Capacity loss issues

Table 1–3 The comparison between Na and Li [31–33].

	Na	Li
E^0 (vs. SHE)	–2.71 V	–3.04 V
Atomic weight	23 g mol^{-1}	6.9 g mol^{-1}
Ionic radius	1.02 Å	0.76 Å
A–O coordination	Octahedral, prismatic	Octahedral, tetrahedral
Melting point of metal	371 K	454 K
Price of carbonates	150 USD T^{-1}	5000 USD T^{-1}
Crustal abundance	23000 mg kg^{-1}	20 mg kg^{-1}
Distribution	Evenly worldwide	70% in South America

Table 1–4 Selected layered oxides that have been investigated as positive electrode for Na secondary batteries [39, 40, 41, 44, 45, 47–51].

Active material	Voltage range (V)	Reversible capacity (mAh g^{-1})	Current rate (mA g^{-1})	Cyclability
O3–$NaCrO_2$ [39, 44, 45]	2.0–3.6	120	25	Moderate
O3–$NaNiO_2$ [47]	1.25–3.75	120	23.5	Good
O3–$Na[Ni_{0.5}Mn_{0.5}]O_2$ [40]	2.2–3.8	125	4.8	Moderate
O3–$Na[Ni_{0.33}Mn_{0.33}Co_{0.33}]O_2$ [48]	2.0–3.75	120	24	Good
O3–$Na[Fe_{0.5}Co_{0.5}]O_2$ [49]	2.5–4.0	160	12	Good
P2–$Na_{0.67}[Fe_{0.5}Mn_{0.5}]O_2$ [41, 50]	1.5–4.3	190	12	Poor
P2–$Na_{0.67}[Fe_{0.33}Mn_{0.66}]O_2$ [50, 51]	1.5–4.3	191	12	Poor

Table 1–5 Selected phosphates that have been investigated as positive electrode for Na secondary batteries [62, 63, 67, 71, 74, 76, 77, 82, 59, 84, 85].

Active material	Average potential (V)	Reversible capacity (mAh g^{-1})	Current rate (mA g^{-1})	Volume change (%)	Carbon coating	Cyclability
Olivine $NaFePO_4$ [62, 63]	2.7	125	7.5	17.6	Need	Moderate
$Na_2FeP_2O_7$ [67]	2.9	90	9.7	2.6	No need	Good
$Na_{1.56}Fe_{1.22}P_2O_7$ [71]	3.0	85	4.8	1.9	No need	Good
$Na_4Fe_3(PO_4)_2P_2O_7$ [74]	3.2	110	3.2	4.0	Need	Good
$Na_3V_2(PO_4)_3$ [76, 77]	3.4	116	11.7	8.3	Need	Good
$Na_3V_2(PO_4)_2F_3$ [82]	3.95	110	12.8	1.8	Need	Good
Na_2FePO_4F [59, 85]	3.0	110	6.2	3.7	Need	Moderate
$Na_{1.5}VPO_{4.8}F_{0.7}$ [84]	3.8	134	13	2.9	Need	Good

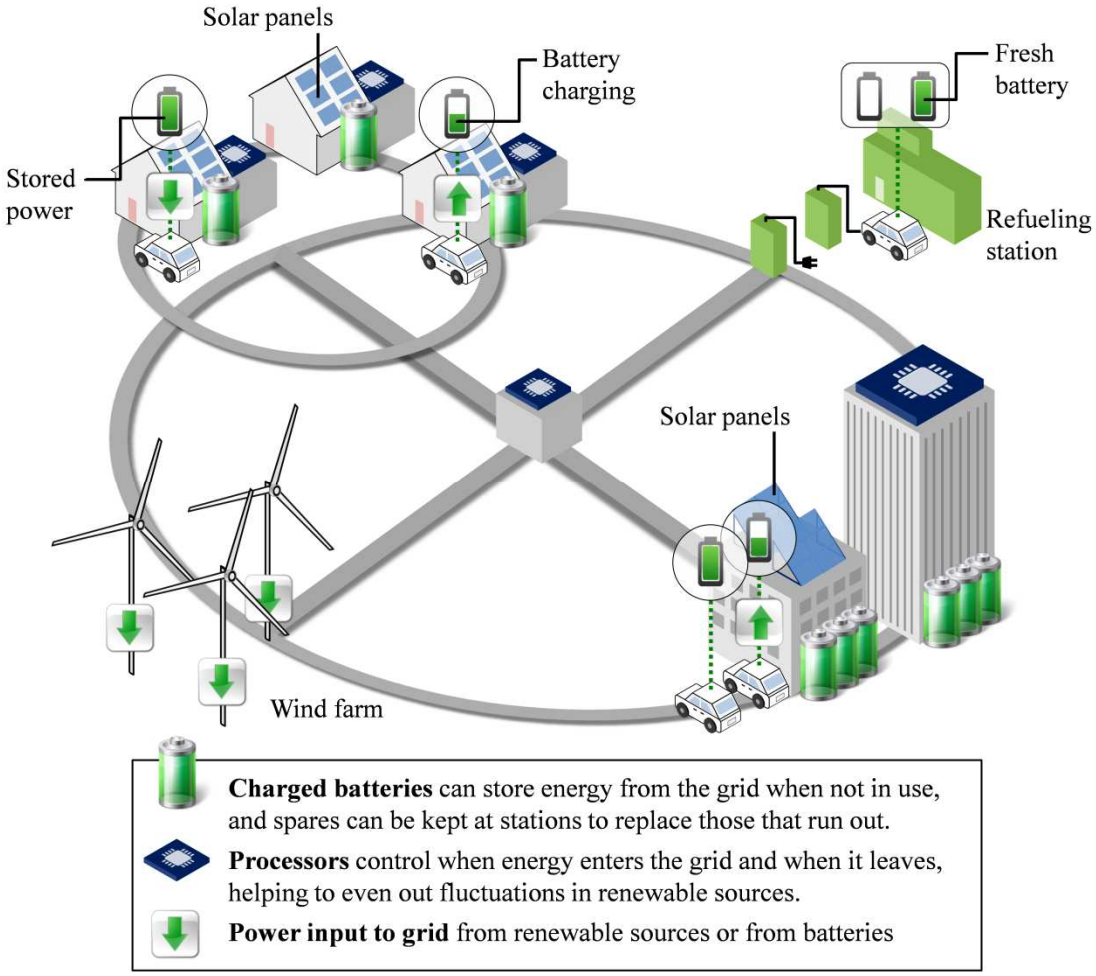

Fig. 1–1 An illustration for the smart grid concept [8, 9].

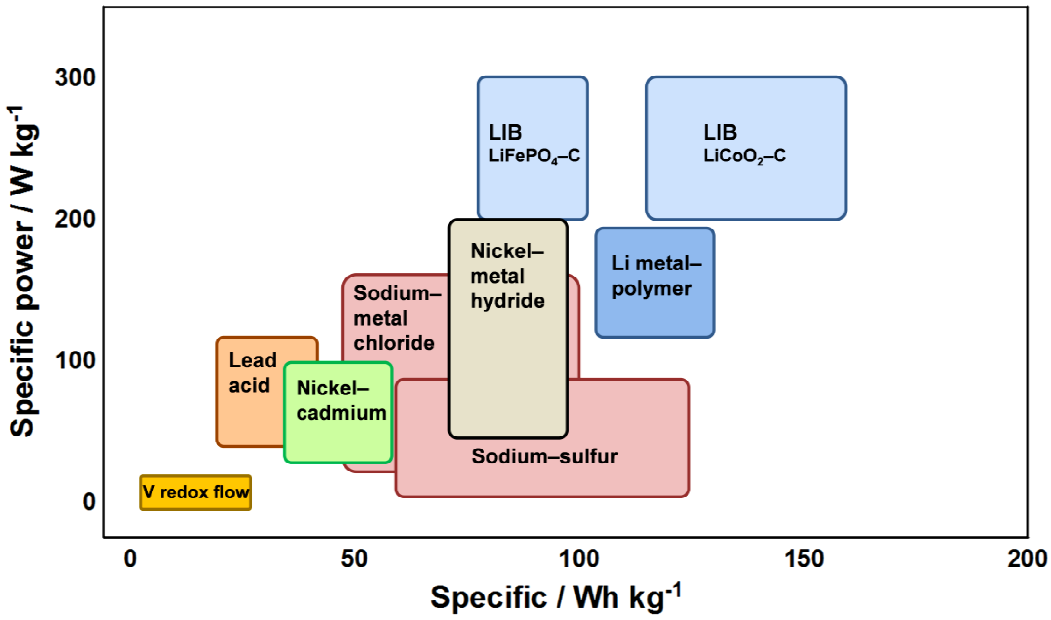

Fig. 1–2 Gravimetric energy and power densities for presently available batteries being considered for grid scale energy storage applications [2].

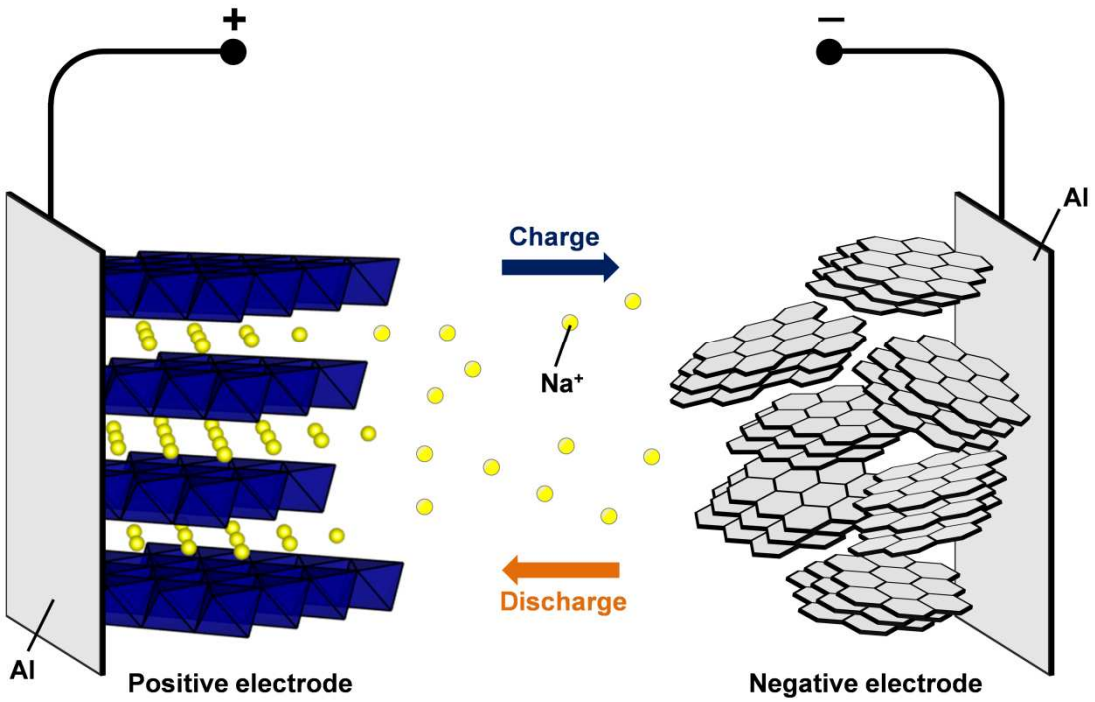

Fig. 1–3 A schematic illustration depicting the working principle of rocking-chair type Na secondary batteries [33, 102].

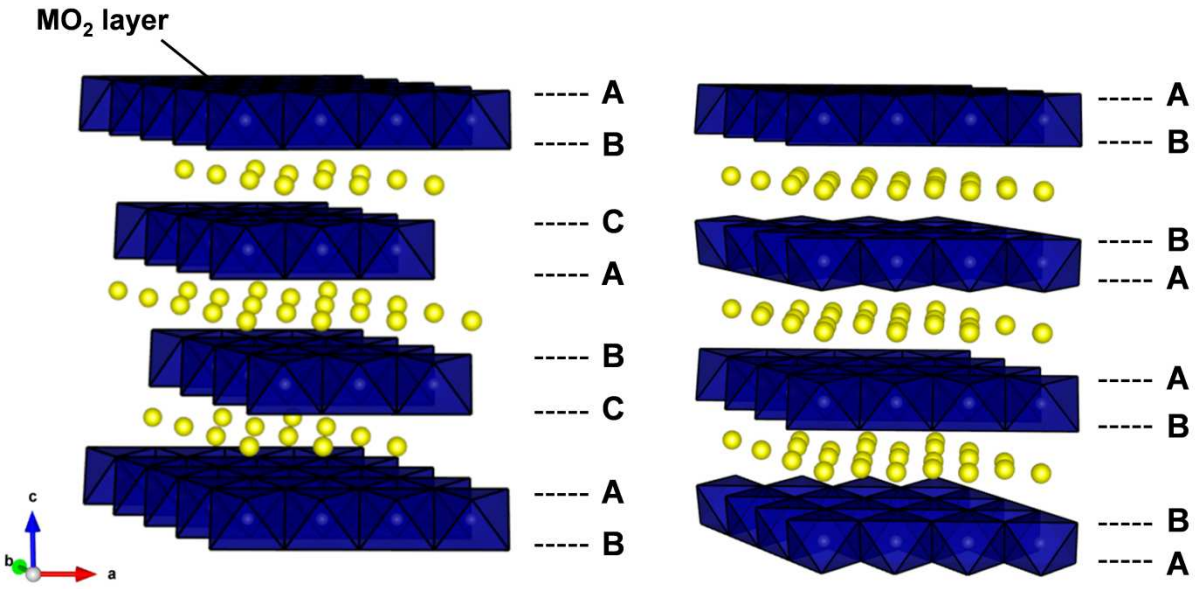

Fig. 1–4 The crystalline structure of O3–type (left) and P2–type (right) layered oxide $NaMO_2$. Symbols A, B and C in the schematics represent the three different oxygen layers [41].

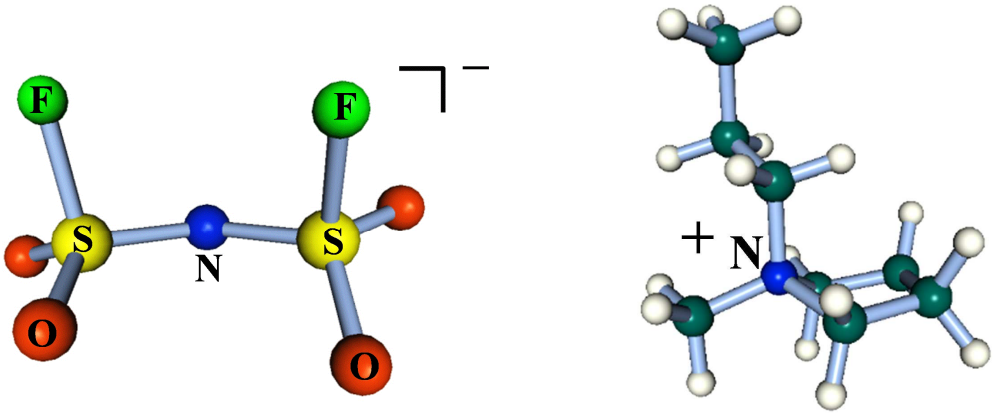

Fig. 1–5 The structures of FSA anions (left) and C_3C_1pyrr cations (right).

Chapter 2

Experimental

2.1 Apparatus

Air- and moisture-sensitive materials were handled in a glove box (Miwa Manufacturing Co., Ltd. DBO-2LKH-HNBR) with a gas-refining instrument filled with dried and deoxygenated argon gas (99.995%). The dew point (*ca*. 163 K) and concentration of oxygen (*ca*. 1 ppm) were always monitored during the experiment (Oxygen Analyzer DF-150E, General Electric Company). Electric balances (CPA225D, Sartorius; WMC25-SH, Mettler Toledo) were equipped in the glove box to weigh reagents and samples.

For the purposes of drying the materials and impregnation of ionic liquids into a separator and electrodes, a vacuum line and vessels were used. Their schematic illustrations are shown in Figs. 2–1 and 2–2. The main line was made of corrosion-resistant stainless steel pipes (SUS316, 1/2 inch o.d.) connected by the stainless unions and valves with a Kel-F (polychlorotrifluoroethylene) tip (Swagelok Co.). Metal and PFA (tetrafluoroethylene-perfluoroalkylvinylether copolymer) tube (1/4 inch o.d.) were used as the connecting parts to a vacuum vessel. The line was connected to a rotary vacuum pump through a Pyrex glass cold trap. The typical degree of vacuum in this system was below 2 Pa. The pressure was monitored by Bourdon and Pirani gauges.

2.2 Synthesis of active materials

All chemicals used in this study were of analytical-grade. For solid-state method,

specific precursors were thoroughly mixed with acetone via a high-energy planetary ball-milling (Pulverisette 7 Premium Line, Fritsch). The grinding chamber and balls (diameter of 3 mm) were made of zirconia. The ball-to-powder weight ratio was fixed at 20. The ball-milling was carried out at a speed of 600 rpm. The milling time lasted for 24 h with 15 min of grinding and 15 min of rest. The grinding was alternately clockwise and anti-clockwise for the production of homogeneously mixed precursors. After evaporating the acetone, the mixture was ground in an agate mortar and placed inside a tube furnace (KTF045N1, Koyo). Before sintering, the furnace was vacuum pumped for 30 min and underwent steady Ar flow for 30 min. The heating and cooling rates were 5 and 2 K min^{-1}, respectively. The schematic illustration of the tube furnace is shown in Fig. 2–3. The detailed procedures are described in each chapter.

2.3 Materials characterization

2.3.1 X-ray diffraction analysis

The structure of as-synthesized $NaCrO_2$, $Na_{2-x}Fe_{1+x/2}P_2O_7$, and Na_2MnSiO_4 was characterized by powder X-ray diffraction (XRD) using Rigaku Ultima IV or Rigaku SmartLab instruments equipped with Cu-Kα radiation and a one-dimensional high speed detector (D/teX Ultra) in the Bragg-Brentano geometry. The measurements were performed at 40 kV–40 mA for Rigaku Ultima IV and 40 kV–30 mA for Rigaku SmartLab, respectively. The structure refinement was carried out by the Rietveld method in an iterative procedure using the RIETAN–FP software package [1]. The crystal structures were visualized using the VESTA software [2].

The structural variation during charge–discharge test was studied by ex-situ X-ray diffraction analysis. The samples were prepared in the half cells by applying a constant

current for a given duration to fix the amount of extracted (or inserted) sodium. Subsequently, the electrodes removed from the cells were rinsed with dehydrated tetrahydrofuran (THF; Wako, water content < 10 ppm, oxygen content < 1 ppm) to remove the electrolyte and placed in an air-tight cell with Be windows to avoid exposure to the air. XRD patterns were recorded in Ar or He atmosphere at room temperature.

2.3.2 Electron microscopy observation

The morphology of the as-synthesized $NaCrO_2$, $Na_{2-x}Fe_{1+x/2}P_2O_7$, and Na_2MnSiO_4 was observed with a field emission scanning electron microscope (FE-SEM, Hitachi SU-8020) operating at 10 kV (or less) to avoid the charging effect. For carbon-coated Na_2MnSiO_4/C samples, the morphology was also observed by transmission electron microscope (TEM, Hitachi H-9000UHR).

2.3.3 Thermogravimetric analysis

The thermal stability of as-synthesized Na_2MnSiO_4 and desodiated $Na_{0.8}MnSiO_4$ was evaluated by thermogravimetric analysis (TGA, Rigaku, Thermo plus EVOII TG8120). The measurements were conducted from 298 to 773 K under Ar flow with a heating rate of 5 K min^{-1}. Before heating up, the balance purge was performed for 30 min (1 L min^{-1} for inlet gas, 800 mL min^{-1} for evacuation side), followed by the sample purge for 30 min (1 L min^{-1} for inlet gas, 200 mL min^{-1} for evacuation side). During the measurements, the temperature difference between the specimen and reference pan (differential thermal analysis, DTA) was also recorded.

2.3.4 Nitrogen adsorption measurement

The specific surface area of as-synthesized Na_2MnSiO_4 and Na_2MnSiO_4/C was deduced from the results of nitrogen adsorption/desorption measurement by a Micromeritics TriStar II 3020 analyzer at 77 K. The Brunauer Emmett and Teller (BET) model was used [3]. Since BET theory ignores inhomogeneity of the surface and lateral adsorbate-adsorbate interactions, high energy sites at lower relative pressures ($P/P_0 < 0.05$) may cause the nonlinearity of BET plots. Relative pressure near completed monolayers ($0.05 < P/P_0 < 0.30$) was used for the surface area determination.

2.3.5 Inductively coupled plasma atomic emission spectroscopy and atomic absorption spectroscopy

The compositional analysis of as-synthesized $Na_{2-x}Fe_{1+x/2}P_2O_7$ was evaluated by inductively coupled plasma atomic emission spectroscopy (ICP-AES, SII SPS4000). Nitric acid, perchloric acid, and sulfuric acid were used to ensure the complete dissolution of samples. For the composition study of Na, atomic absorption spectrometry (AAS, Hitachi Z2300) was performed.

2.3.6 X-ray absorption spectroscopy

The variation of electronic structure and local geometric environment of $Na_2FeP_2O_7$ was characterized by X-ray absorption spectroscopy (XAS). XAS experiments were performed at the beam line BL01B1 of the synchrotron radiation facility in SPring–8 (Hyogo, Japan). The Fe *K*-edge spectra were measured in a transmission mode using a Si(111) monochromator. An Fe metal foil was used for the calibration of the absorption energy scale. The experimental data of all samples were analyzed with the program REX–2000 (Rigaku). The backscattering

phases and the amplitude were theoretically calculated by the code FEFF8 [4]

2.4 Electrochemical measurements

2.4.1 Ionic liquid electrolytes

The ionic liquid (IL) electrolytes used in this study consist of alkali metal cations or *N*-methyl-*N*-propylpyrrolidinium (C_3C_1pyrr) cations and bis(fluorosulfonyl)amide (FSA) anions. Na[FSA] (Mitsubishi Materials Electronic Chemicals CO., Ltd., purity >99%) and K[FSA] (Mitsubishi Materials Electronic Chemicals CO., Ltd., purity >99%) were purchased and dried under vacuum at 353 K and 333 K for 48 h, respectively. [C_3C_1pyrr][FSA] (Kanto Chemical Co., Inc., purity >99.9%) were dried under vacuum for 24 h at 333 K prior to use. The IL mixtures, Na[FSA]–K[FSA] (56:44 molar ratio) and Na[FSA]–[C_3C_1pyrr]FSA (20:80 molar ratio), were utilized as the electrolyte. Detailed characterization of these ILs has been reported in previous studies [5–8].

2.4.2 Electrodes and cell configurations

The positive electrodes were fabricated by mixing as-synthesized $NaCrO_2$, $Na_{2-x}Fe_{1+x/2}P_2O_7$, or Na_2MnSiO_4/C with acetylene black (AB; Wako, purity >99.99%) as a conductive additive and polytetrafluoroethylene (PTFE; Aldrich) as a binder at a fixed weight ratio. Metallic sodium discs (Aldrich, purity 99.95%) pressed onto aluminum or nickel current collectors were used as reference and counter electrodes. Borosilicate glass microfiber filters (Whatman GF/A, thickness of 260 μm) were used as the separators and soaked with Na[FSA]–K[FSA] or Na[FSA]–[C_3C_1pyrr]FSA under vacuum at 363 K and 333 K, respectively, for 2 d to achieve full impregnation. Since Na[FSA]–K[FSA] is solid at room temperature, a customized two-electrode cell (Tomcell Japan Co., Ltd.) was used to favor the

cell assembling. A schematic illustration of the two-electrode cell is shown in Fig. 2–4. For the cells utilized Na[FSA]–[C_3C_1pyrr]FSA electrolyte, conventional CR2032 type coin cells were used. All cells were assembled in the Ar-filled glove box.

2.4.3 Galvanostatic charge–discharge test

The specific capacity of the as-synthesized $NaCrO_2$, $Na_{2-x}Fe_{1+x/2}P_2O_7$, and Na_2MnSiO_4/C was evaluated by galvanostatic charge–discharge test conducted by a Bio-Logic VSP potentiostat/galvanostat or a computer-controlled charge–discharge unit (HJ1001SD8, Hokuto Denko). The cells were aged for 2 h before charge–discharge to ensure full absorption of the electrolyte in the electrode and also to reach a thermal equilibrium. The test was typically carried out at a rate of 10 mA g^{-1} or C/10 (fully charging in 10 h), and the current density during galvanostatic cycling was maintained constant for both charge and discharge. The operating temperature was controlled by an ESPEC SU221 Environmental Test Chamber or a mantle heater. All of the specific capacities in the following chapters are calculated based on the mass of active material.

2.4.4 Galvanostatic intermittent titration technique

The electrochemical measurement using Galvanostatic intermittent titration technique (GITT) was conducted by a Bio-Logic VSP potentiostat/galvanostat to acquire charge–discharge curves of the $Na_2FeP_2O_7$ electrode close to the thermodynamic equilibrium [9]. GITT measurements were consisting of a series of small current pulses (C/20 rate), each followed by a relaxation period allowing material homogenization. The relaxation time lasted until the voltage shift below 10 mV h^{-1}.

2.4.5 Electrochemical impedance spectroscopy

For $Na_2FeP_2O_7$ and Na_2MnSiO_4 electrodes, electrochemical impedance spectroscopy (EIS) measurements were carried out using a Bio-Logic VSP potentiostat/galvanostat over a frequency range from 200 kHz to 5 mHz with an AC perturbation voltage of 10 mV.

References

[1] F. Izumi, K. Momma, Solid State Phenom. 130 (2007) 15–20.

[2] K. Momma, F. Izumi, J. Appl. Crystallogr. 44 (2011) 1272–1276.

[3] S. Brunauer, P.H. Emmett, E. Teller, J. Am. Chem. Soc. 60 (1938) 309–319.

[4] J.J. Rehr, C. Albers, Rev. Mod. Phys. 72 (2000) 621–654.

[5] K. Kubota, T. Nohira, T. Goto, R. Hagiwara, Electrochem. Commun. 10 (2008) 1886–1888.

[6] K. Kubota, T. Nohira, R. Hagiwara, J. Chem. Eng. Data 55 (2010) 3142–3146.

[7] A. Fukunaga, T. Nohira, Y. Kozawa, R. Hagiwara, S. Sakai, K. Nitta, S. Inazawa, J. Power Sources 209 (2012) 52–56.

[8] C.S. Ding, T. Nohira, K. Kuroda, R. Hagiwara, A. Fukunaga, S. Sakai, K. Nitta, S. Inazawa, J. Power Sources 238 (2013) 296–300.

[9] W. Weppner, R.A. Huggins, J. Electrochem. Soc. 124 (1977) 1569–1578.

[10] Kosuke Takagi, Master Thesis, Kyoto University (2012).

[11] Toshinari Koketsu, Master Thesis, Kyoto University (2012).

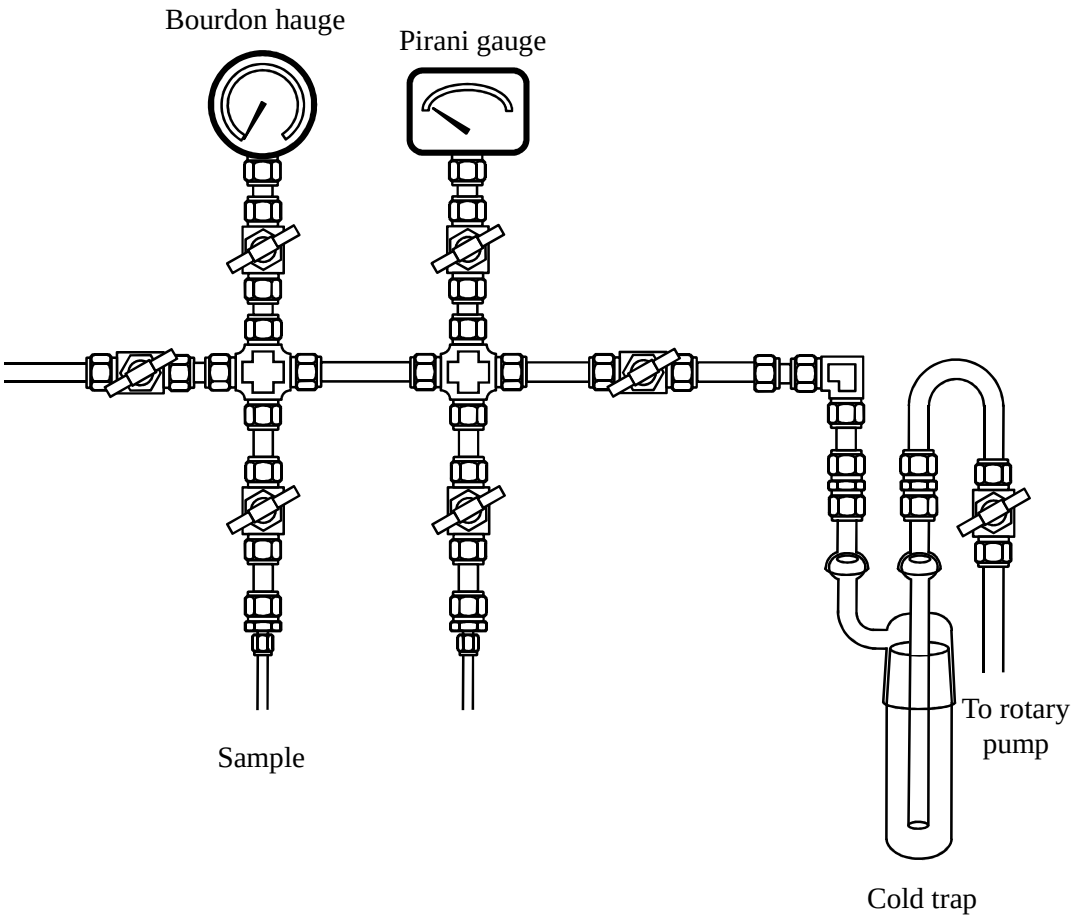

Fig. 2–1 A schematic illustration of a vacuum line [10].

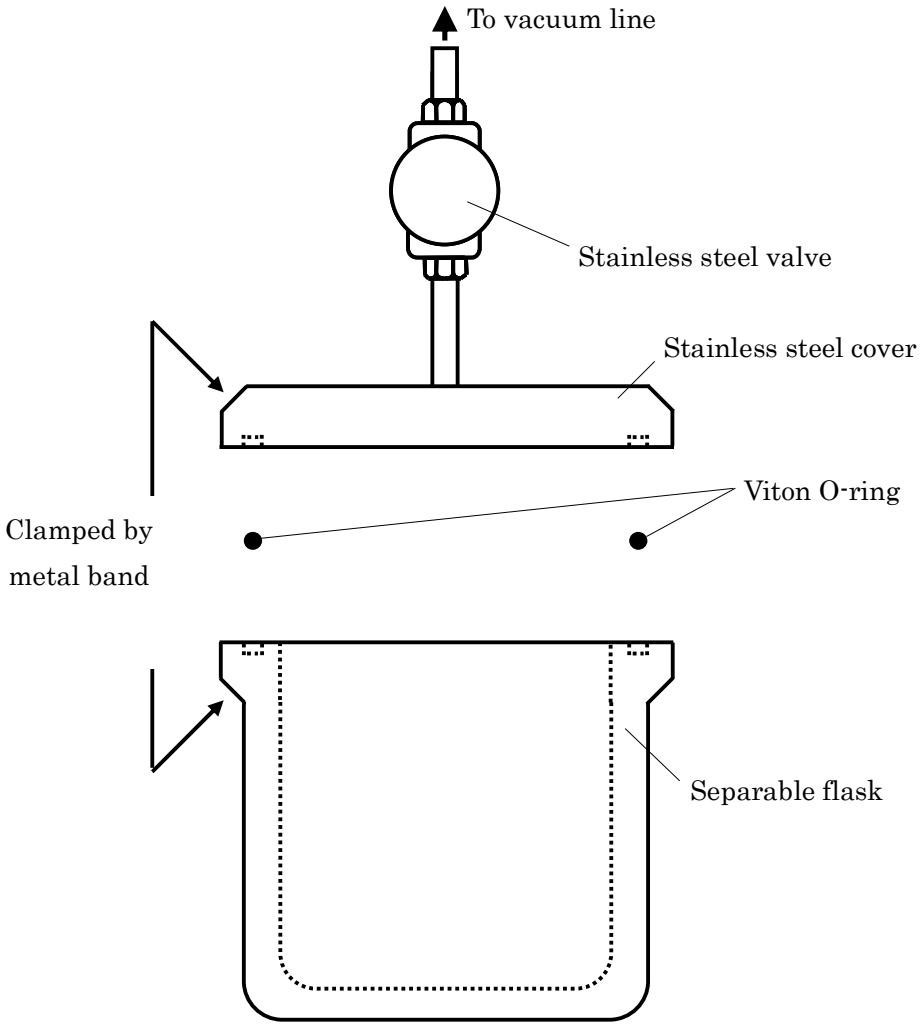

Fig. 2–2 A schematic illustration of a vessel for vacuum drying [11].

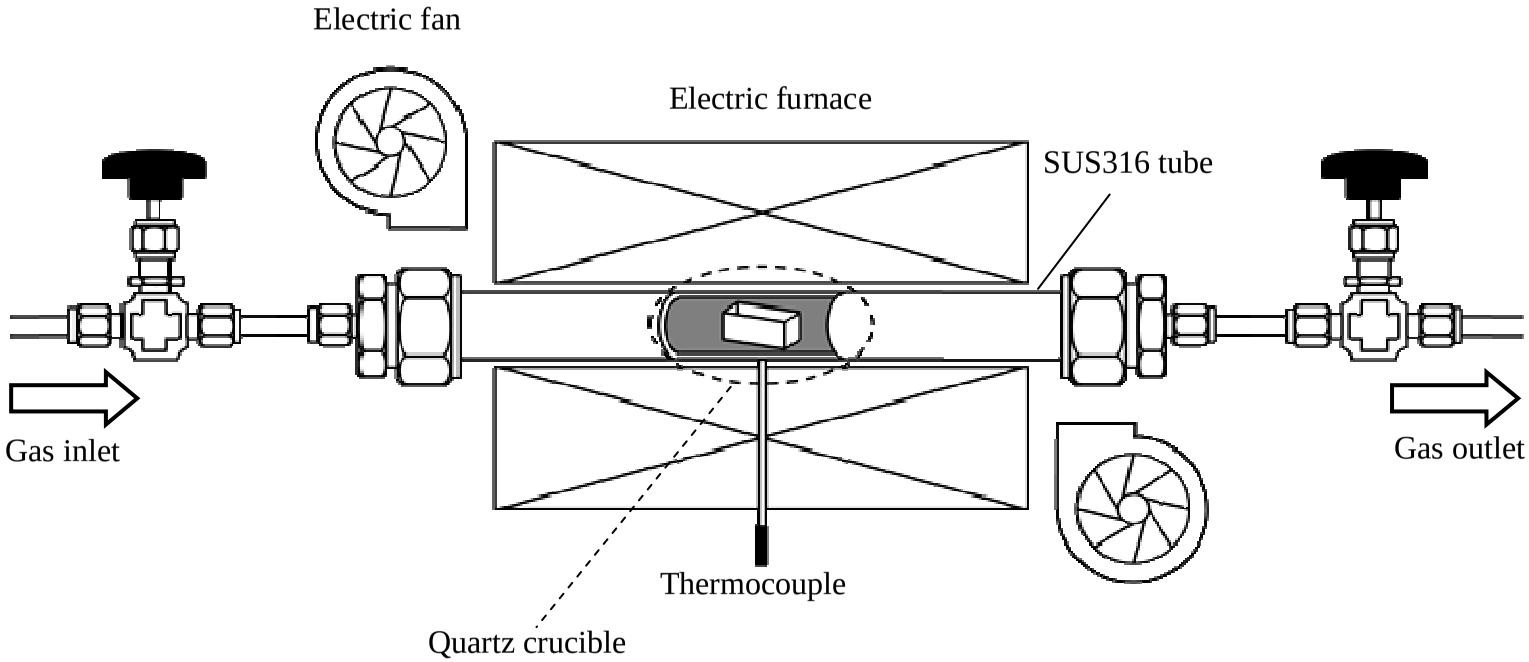

Fig. 2–3 A schematic illustration of a tube furnace [10].

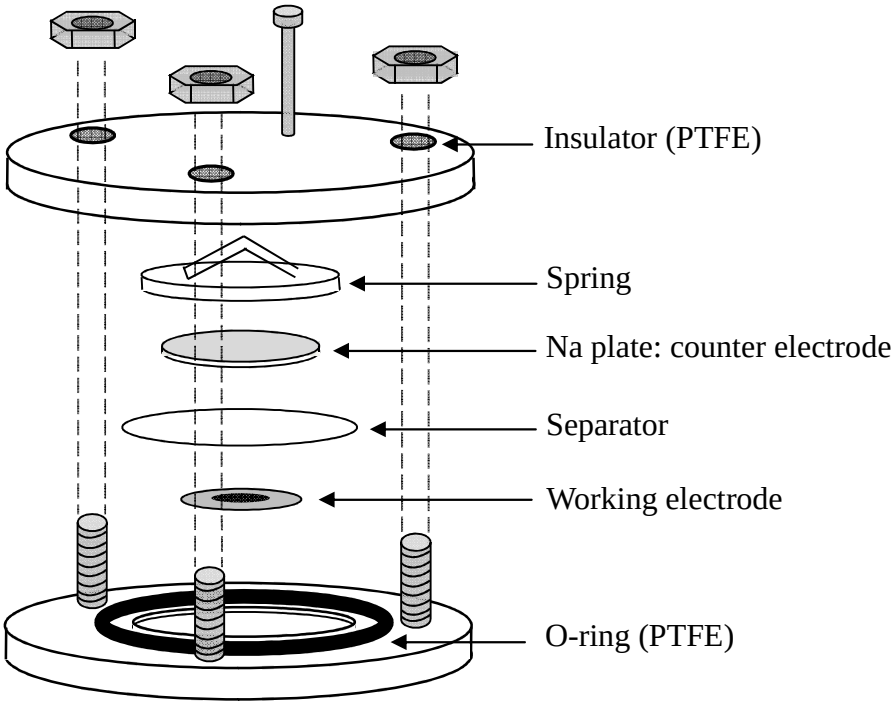

Fig. 2–4 A schematic illustration of the customized two-electrode cell (Tomcell Japan Co., Ltd.) for charge–discharge tests [11].

Chapter 3

Layered oxide $NaCrO_2$ positive electrode in Na[FSA]–K[FSA]

3.1 Introduction

The performance and operational safety of a battery are directly linked to the choice of electrolyte and finding suitable active materials for both positive and negative electrodes are essential for improving the overall performance of a battery. Sodium, being larger in size than lithium and also due to its greater screening effect, has a strong tendency to favor the formation of layered compounds [1]. The sodium layered oxide positive electrode materials (generally formulated as Na_xMO_2) evaluated thus far can be classified into two main groups, i.e., the O3–type and P2–type, in which the sodium ions are coordinated in octahedral and prismatic environments, respectively [2, 3]. The number in this expression (e.g., 3 in O3) describes the number of transition metal (M) layers along the stacking direction in the unit cell [3]. During battery operation, the Na ions are reversibly intercalated/deintercalated into/from these compounds. The cycle property and rate capability are thus directly associated with the intercalation mechanisms. More in-depth research into and fundamental understanding of the structural evolution of the electrode during the entire Na intercalation/deintercalation process are needed to push the technology forward.

Efforts towards this end by Delmas *et al*. have demonstrated the occurrence of reversible phase transitions of various Na_xCoO_2 polymorphs occurred reversibly in electrochemical sodium cells [4, 5]. For example, P2–Na_xCoO_2 exhibited numerous two-phase regions in the potential curve during electrochemical desodiation. The formation of Na^+/vacancy ordered

lamellar structures was confirmed via in-situ X-ray diffraction analysis [4] and it was also shown that the rhombohedral O3–$NaCoO_2$ can undergo transformation to a monoclinic distorted P'3 structure [5]. The phase transition between O3 and P3 is associated with the gliding of MO_2 slabs with respect to each other, and it is generally sensitive to the sodium content. Besides, the temperature may also play a role. It is reported that the monoclinic P'3–Na_xCoO_2 spontaneously converted into a rhombohedral structure at temperatures greater than 350 K [6]. Recently, Komaba *et al*. showed that the electrochemically driven Na intercalation/deintercalation into/from $NaCrO_2$ was associated with the O3, distorted O'3 and P'3 phase transitions [7]. Similar interconvertions between O–type and P–type have also been observed in solid solutions of Na_xMO_2 such as $Na[Ni_{0.5}Mn_{0.5}]O_2$ [8], $Na[Ni_{1/3}Mn_{1/3}Co_{1/3}]O_2$ [1], $Na_{2/3}[Ni_{1/3}Mn_{2/3}]O_2$ [9, 10], $Na_{0.80}[Li_{0.12}Ni_{0.22}Mn_{0.66}]O_2$ [11], although little is understood about this transformation and its effect on the kinetics of sodiation/desodiation.

In previous works, the cell performance of a sodium secondary battery using the $NaCrO_2$ positive electrode in Na[TFSA]–Cs[TFSA] at 423 K [12] and in Na[FSA]–K[FSA] at 353 K [13] were reported. The present study focuses on the detailed electrochemical and structural behavior of $NaCrO_2$ in Na[FSA]–K[FSA] at 363 K with the objective of understanding the sodiation/desodiation mechanisms. The obtained structural characterization and electrochemical properties are compared with previous reports in which a conventional organic electrolyte was employed at room temperature.

3.2 Experimental

The $NaCrO_2$ powder was synthesized by means of the conventional solid-state reaction of stoichiometric Na_2CO_3 (Wako, > 99.9%) and Cr_2O_3 (Wako, > 98%) at 1123 K for 5 h under Ar flow [13].

The positive electrode was fabricated by mixing $NaCrO_2$ with acetylene black (AB) and polytetrafluoroethylene (PTFE) at a weight ratio of 85:10:5. The active material load was about 2.5 mg cm^{-2}. A metallic sodium disc (Aldrich, purity 99.95%) were pressed on nickel current collector and used as the reference and counter electrodes. Na[FSA] and K[FSA] (56:44, molar ratio) was used as the electrolyte. Galvanostatic charge–discharge cycles were performed with a half-cell in the voltage range between 2.5 and 3.5 V. Cyclic voltammetry (CV) experiments were also carried out at various different scan rates (0.1, 0.2, and 0.5 mV s^{-1}).

For the ex-situ XRD study, the Na_xCrO_2 samples were prepared in the sodium cells by applying a constant oxidation current (10 mA g^{-1}) to $NaCrO_2$ for a given duration to fix the amount of extracted sodium. Subsequently, the electrodes removed from the cells were rinsed with anhydrous tetrahydrofuran (THF) to remove the electrolyte and placed in an air-tight cell inside a glove box.

3.3 Results and discussion

$NaCrO_2$ was obtained as fine-grain powder with a gray-green color. All the peaks in the XRD pattern shown in Figure 3–1 can be indexed to rhombohedral O3–type $NaCrO_2$ (*R*–3*m* space group, JCPDS card No. 25-0819). A typical scanning electron microscope (SEM) image of the $NaCrO_2$ powder is shown in Fig. 3–2. The individual particles consist of primary particles of $NaCrO_2$ with diameters of about 10 μm.

The cyclic voltammetry (CV) curves for the $NaCrO_2$ electrode recorded at scan rates of 0.1, 0.2, and 0.5 mV s^{-1} are shown in Fig. 3–3. The $NaCrO_2$ electrode underwent Na intercalation/deintercalation with several reversible phase transitions evidenced as pairs of redox peaks that are clearly observed in each CV profile. The clear peak separation in each of the CV profiles indicates that the Na intercalation/deintercalation processes into/from $NaCrO_2$

are associated with the formation of distinct phases [14, 15]. The shapes and areas of the redox waves remain largely unchanged during the successive scans at the various rates, indicating that reversible redox reactions occur within this potential range. It should be noted that the signal-to-noise ratio of CV in the present work is better than previous results obtained at room temperature [16], reflecting the faster electrode kinetics at the intermediate temperature of 363 K. The potential difference (ΔE_p) between the anodic peak and the corresponding cathodic peak gradually increases with increasing scan rate, comparable to previous reports for lamellar Na_xMO_2 materials [14].

The discharge capacity and the rate capability of the $NaCrO_2$ electrode were examined as shown in Fig. 3–4. A large specific capacity of 113 mAh g^{-1} was observed at a current density of 125 mA g^{-1}. Even at the very high current density of 2000 mA g^{-1}, a reversible capacity of 63 mAh g^{-1} was retained. This rate capability is comparable to the layered positive electrode for lithium ion batteries [17], which is attributed to faster kinetics at the elevated temperature (363 K). The result confirms that a moderately elevated operating temperature effectively enhances the kinetics of the Na intercalation/deintercalation processes.

The $NaCrO_2$ electrode also exhibits stable cycling properties as shown in Fig. 3–5a and b. Approximately 98% of the initial capacity is maintained at the 100th cycle with a Coulombic efficiency of 99.6% at a cycling current of 125 mA g^{-1}. The average capacity fading is less than 0.02% per cycle. A discharge capacity of 112 mAh g^{-1} is maintained at the 100th cycle, which is higher than that of the $NaCrO_2$ reported previously [16, 18].

It was recently reported that the cyclability of positive electrodes in sodium secondary batteries depends strongly on the solvents used [19]. For example, reduction products, such as sodium propyl carbonate, are reportedly generated on the sodium negative electrode surface by the reaction with PC that is the most commonly utilized solvent in sodium batteries. This species dissolves (although very slightly) into the electrolyte and can be oxidized on the

positive electrode at top-of-charge, thereby limiting capacity utilization and causing low coulombic efficiency. Even when carbon materials were utilized as a negative electrode in lieu of sodium metal, Na_2CO_3 and sodium alkyl carbonates were still found on the electrode surface as a major part of the SEI film [20, 21]. Moreover, destructive oxidative decomposition of the electrolyte solution ($NaClO_4$/PC) and co-intercalation of solvent molecules are speculated to play a role in capacity fading [18]. Consequently, practical application requires either positive electrode surface treatments [16] or the use of electrolyte additives such as fluoroethylene carbonate (FEC) [21]. In contrast to the carbonate-based electrolytes, the Na[FSA]–K[FSA] ionic liquid possesses good chemical and thermal stability, and it can be applied without the use of an additive.

The Na-driven structural transformation and the changes in the sodium composition at an intermediate temperature were evaluated using ex-situ XRD. Fig. 3–6 shows the XRD patterns of $Na_{1-x}CrO_2$ prepared at different states of charge. The $(003)_{hex}$ and $(104)_{hex}$ diffraction peaks (these peaks are indexed in the hexagonal setting), which belong only to the rhombohedral phase, are absent when $x > 0.2$. New diffraction peaks such as (001) for a monoclinic cell appear during further desodiation. Overall, the characteristic diffraction lines of the layered structure are observed at all compositions, indicating that the phase transitions occur as a consequence of slippage of the CrO_2 slabs without breaking of the Cr–O bonding. The composition-driven structural change is in the following sequence: rhombohedral O3 → monoclinic O'3 → monoclinic P'3. Schematic illustrations of the $Na_{1-x}CrO_2$ crystal structures are shown in Fig. 3–7. The lattice is made up of slabs of edge-sharing CrO_6 octahedra, between which Na^+ ions are inserted in an octahedral (O3) or trigonal prismatic (P3) environment. For each composition, the cationic distribution would thus result from the energy minimization between (1) the electrostatic repulsion that tends to separate the Na^+ ions in the *ab* plane, (2) the electron–electron interaction in the Cr layer, and (3) the Na^+–$Cr^{3+/4+}$

repulsion through the common face between the NaO_6 and CrO_6 polyhedra [4]. In order to facilitate comparison of the cell parameters, all samples were indexed in the monoclinic system. The hexagonal lattice parameters for the rhombohedral cell are related to the monoclinic cell parameters by the following relations [22]:

$$a_{\text{hex.}} = a_{\text{mon.}} / \sqrt{3}$$

$$b_{\text{hex.}} = b_{\text{mon.}}$$

$$c_{\text{hex.}} = 3c_{\text{mon.}} \sin \beta$$

The calculated Cr–Cr (in-plane distances, corresponding to the a_{mon} lattice parameter) and interslab distances (corresponding to c_{mon}) as a function of x in $Na_{1-x}CrO_2$ are plotted in Fig. 3–8. Notably, the interslab *d*–spacing increases significantly when the Na ions are removed, as a result of the interruption of the balance of attractive forces between the Na ions and oxide anions and the repulsive forces between the oxide ions in the neighboring layers. The Cr–Cr intrasheet distance concomitantly declines as expected due to the oxidation of Cr^{3+} to the slightly smaller Cr^{4+} ions. These changes are in good agreement with those observed for most Na_xMO_2 layered oxides, implying that the sodium content is positively correlated to the structural cohesion [1, 7, 8, 22].

There is a subtle difference between the sodium content at which phase transition begins in the present study compared to previous reports of room temperature evaluations. The onset of the phase transition seems to be more favorable at 363 K. In particular, the monoclinic P’3 structure of $Na_{1-x}CrO_2$ is detected at x = 0.3 in this study, whereas it is observed at x = 0.4 and 0.5 at room temperature [7]. It is not surprising that the desodiation kinetics is enhanced at the higher operating temperature used herein, and that the phase transitions are also facilitated. Given that Na ions in a prismatic coordination environment often exhibit higher ionic mobility than octahedrally coordinated congeners [5, 23], a synergistic effect is clearly demonstrated by the enhanced rate capability obtained herein.

3.4 Conclusions

In summary, the charge–discharge behavior and phase transitions of the $NaCrO_2$ positive electrode were investigated in an intermediate temperature ionic liquid Na[FSA]–K[FSA] at 363 K. Electrochemical characterization revealed that the kinetics of the Na intercalation/deintercalation processes was enhanced and good cyclability over 100 cycles was achieved versus when the same materials utilized in a conventional organic electrolyte at room temperature. The desodiation of $NaCrO_2$ resulted in the phase transition following the same sequence as in the case of room temperature charging: rhombohedral O3 → monoclinic O’3 → monoclinic P’3. The phase transitions were facilitated at high temperature relative to room temperature. The enhanced rate capability was attributed primarily to the facilitated Na intercalation/deintercalation kinetics.

References

[1] M. Sathiya, K. Hemalatha, K. Ramesha, J.M. Tarascon, A.S. Prakash, Chem. Mater. 24 (2012) 1846–1853.

[2] N. Yabuuchi, M. Kajiyama, J. Iwatate, H. Nishikawa, S. Hitomi, R. Okuyama, R. Usui, Y. Yamada, S. Komaba, Nat. Mater. 11 (2012) 512–517.

[3] C. Delmas, C. Fouassier, P. Hagenmuller, Physica B&C 99 (1980) 81–85.

[4] R. Berthelot, D. Carlier, C. Delmas, Nat. Mater. 10 (2011) 74–80.

[5] C. Delmas, J.J. Braconnier, C. Foussier, P.Hagenmuller, Solid State Ionics 3–4 (1981) 165–169.

[6] M. Blangero, D. Carlier, M. Pollet, J. Darriet, C. Delmas, J.P. Doumerc, Phys. Rev. B 77 (2008) 184116–1–184116–8.

[7] S. Komaba, T. Nakayama, A. Ogata, T. Shimizu, C. Takei, S. Takada, A. Hokura, I. Nakai, ECS Trans. 16 (2009) 43–55.

[8] S. Komaba, N. Yabuuchi, T. Nakayama, A. Ogata, T. Ishikawa, I Nakai, Inorg. Chem. 51 (2012) 6211–6220.

[9] Z.H. Lu, J.R. Dahn, J. Electrochem. Soc. 148 (2001) A1225–A1229.

[10] D.H. Lee, J. Xu, Y.S. Meng, Phys. Chem. Chem. Phys. 15 (2013) 3304–3312.

[11] J. Xu, D.H. Lee, R.J. Clement, X.Q. Yu, M. Leskes, A.J. Pell, G. Pintacuda, X.Q. Yang, C.P. Grey, Y.S. Meng, Chem. Mater. 26 (2014) 1260–1269.

[12] T. Nohira, T. Ishibashi, R. Hagiwara, J. Power Sources 205 (2012) 506–509.

[13] A. Fukunaga, T. Nohira, Y. Kozawa, R. Hagiwara, S. Sakai, K. Nitta, S. Inazawa, J. Power Sources 209 (2012) 52–56.

[14] M. D'Arienzo, R. Ruffo, R. Scotti, F. Morazzoni, C.M. Maria, S. Polizzi, Phys. Chem. Chem. Phys. 14 (2012) 5945–5952.

[15] X.H. Rui, N. Ding. J. Liu, C. Li, C.H. Chen, Electrochim. Acta 55 (2010) 2384–2390.

[16] J.J. Ding, Y.N. Zhou, Q. Sun, Z.W. Fu, Electrochem. Commun. 22 (2012) 85–88.

[17] S. Seki, Y. Kobayashi, H. Miyashiro, Y. Ohno, A. Usami, Y. Mita, N. Kihira, M. Watanabe, N. Terada, J. Phys. Chem. B 21 (2006) 10229–10230.

[18] S. Komaba, C. Takei, T. Nakayama, A. Ogata, N. Yabuuchi, Electrochem. Commun. 12 (2010) 355–358.

[19] C. Vidal-Abarca, P. Lavela, J.L. Tirado, A.V. Chadwick, M. Alfredsson, E. Kelder, J. Power Sources 197 (2012) 314–318.

[20] M.D. Slater, D. Kim. E. Lee, C.S. Johnson, Adv. Funct. Mater. 23 (2013) 947–958.

[21] S. Komaba, T. Ishikawa, N. Yabuuchi, W. Murata, A. Ito, Y. Ohsawa, ACS Appl. Mater. Interfaces 3 (2011) 4165–4168.

[22] I. Saadoune, A. Maazaz, M. Menetrier, C. Delmas, J. Solid State Chem. 122 (1996) 111–117.

[23] C. Delmas, A. Maazaz, C. Fouassier, J.M. Reau, P. Hagenmuller, Mat. Res. Bull. 14 (1979) 329–335.

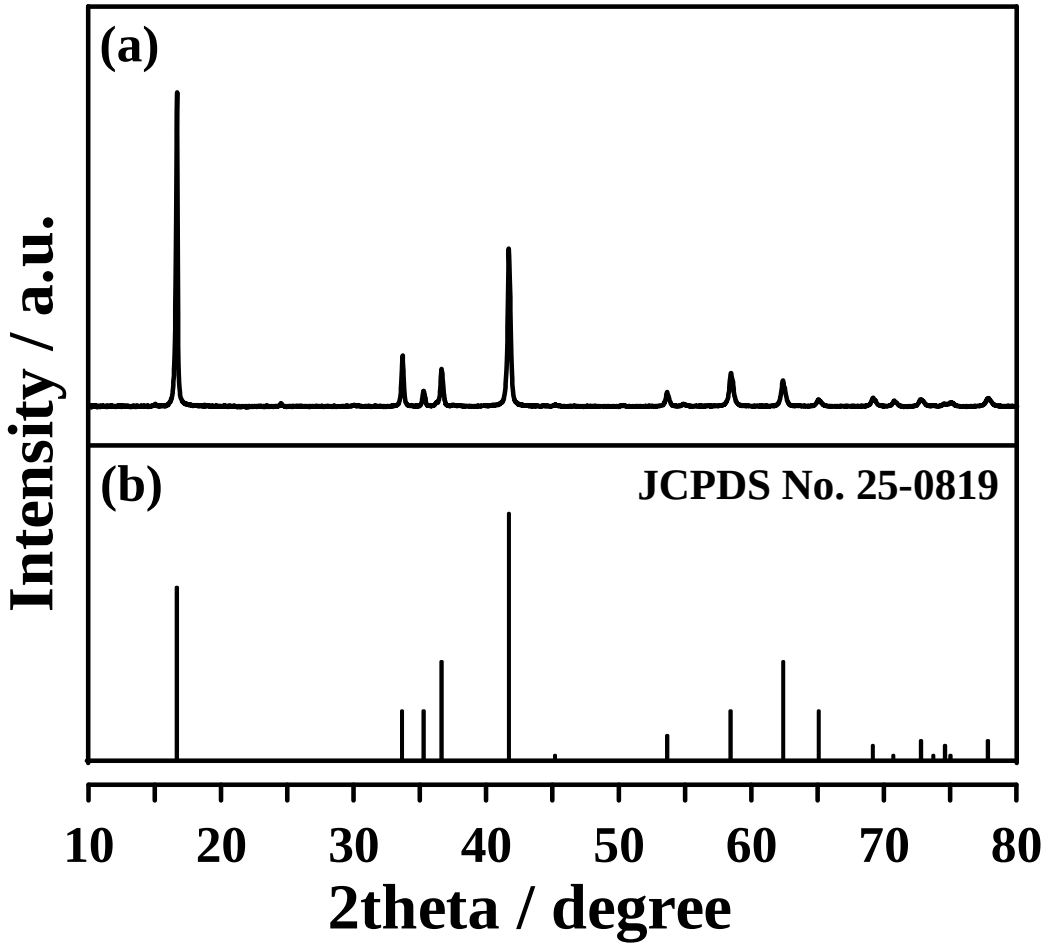

Fig. 3–1 XRD patterns of (a) as-synthesized and (b) reference $NaCrO_2$.

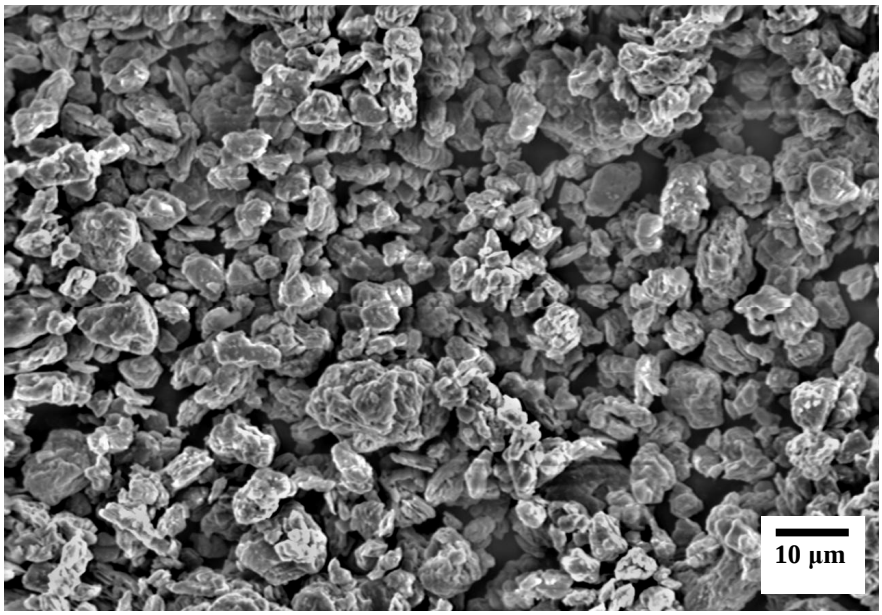

Fig. 3–2 SEM image of $NaCrO_2$.

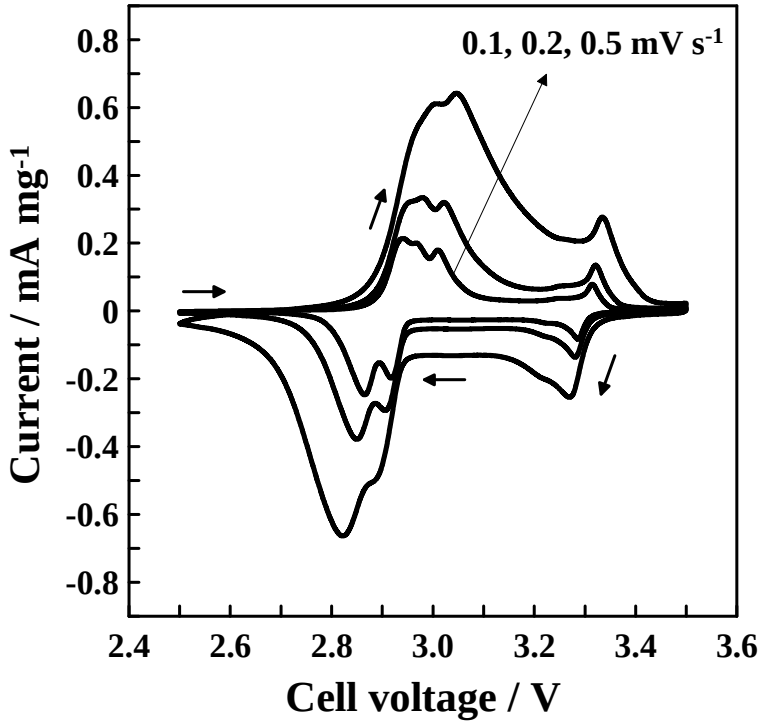

Fig. 3–3 Cyclic voltammograms of the $NaCrO_2$ electrode in the Na[FSA]–K[FSA] ionic liquid acquired between 2.5 and 3.5 V at 363 K. Scan rates: 0.1, 0.2, and 0.5 mV s^{-1}.

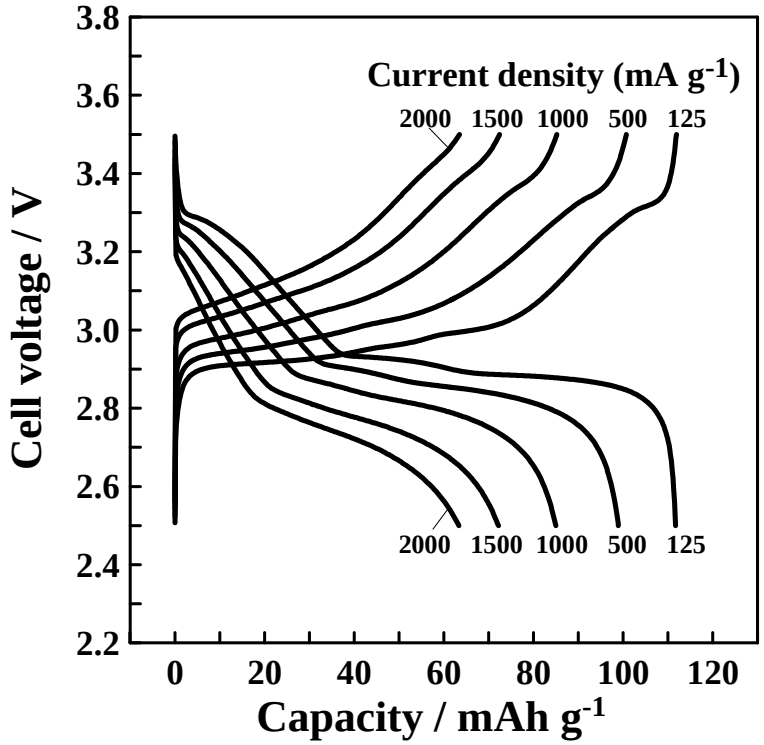

Fig. 3–4 Charge-discharge curves of the $NaCrO_2$/Na[FSA]–K[FSA]/Na cell at 363 K. Charge-discharge rates: 125, 500, 1000, 1500, and 2000 mA g^{-1}. Cut-off voltage: 2.5–3.5 V.

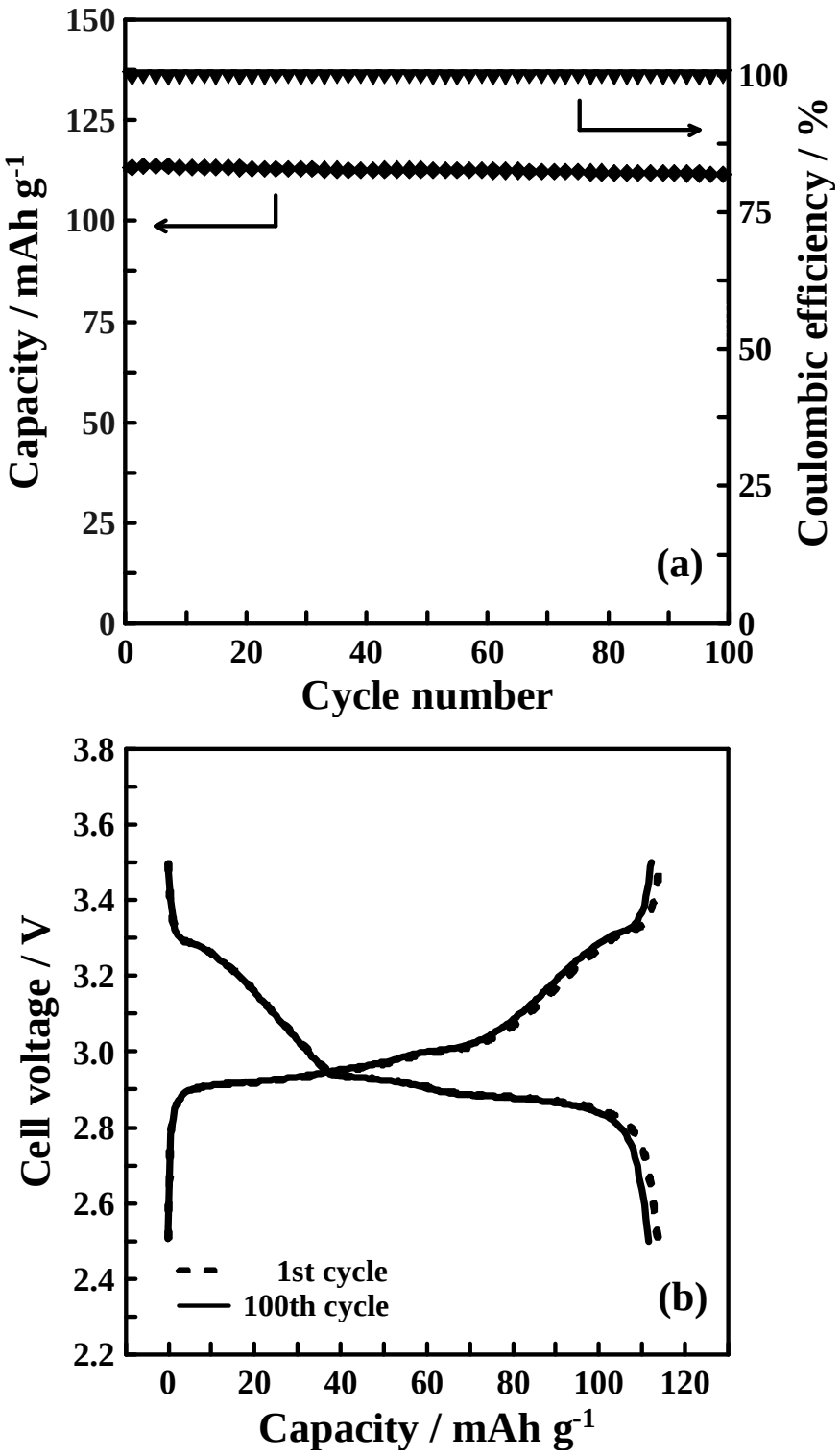

Fig. 3–5 (a) Specific discharge capacity and coulombic efficiency of $NaCrO_2$ positive electrode in Na[FSA]–K[FSA] ionic liquid as a function of cycle number at 363 K. (b) The charge–discharge curves at the 1st and 100th cycle. Current density: 125 mA g^{-1}. Cut-off voltage: 2.5–3.5 V.

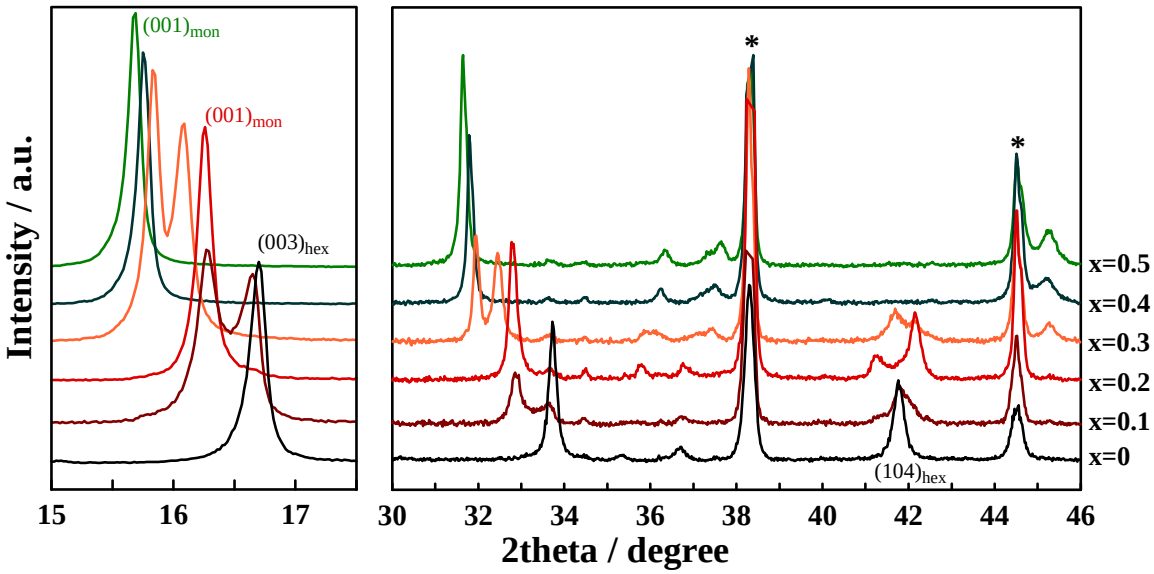

Fig. 3–6 XRD patterns of the $Na_{1-x}CrO_2$ electrodes (x = 0, 0.1, 0.2, 0.3, 0.4 and 0.5). The samples were electrochemically prepared in a $NaCrO_2$/Na[FSA]–K[FSA]/Na cell at 363 K. The XRD measurements were performed at room temperature. Peaks marked by an asterisk are assigned to the aluminium current collector. The $(003)_{hex}$ and $(104)_{hex}$ peaks are indexed in the hexagonal setting although the crystal system is rhombohedral.

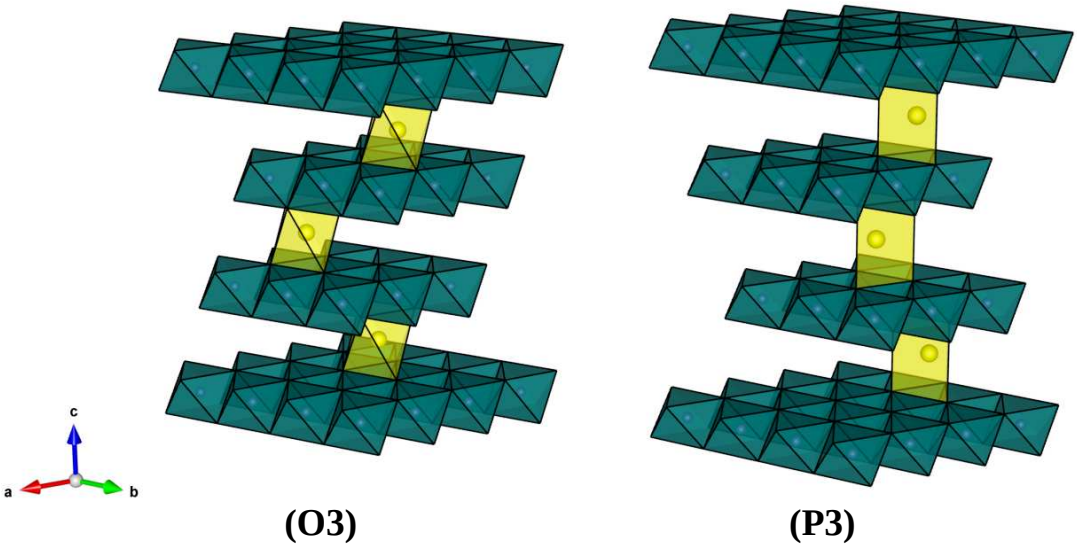

Fig. 3–7 Schematic illustrations of the crystal structure of $Na_{1-x}CrO_2$. Sodium ions are located at the octahedral and prismatic sites in the O3 and P3 types, respectively.

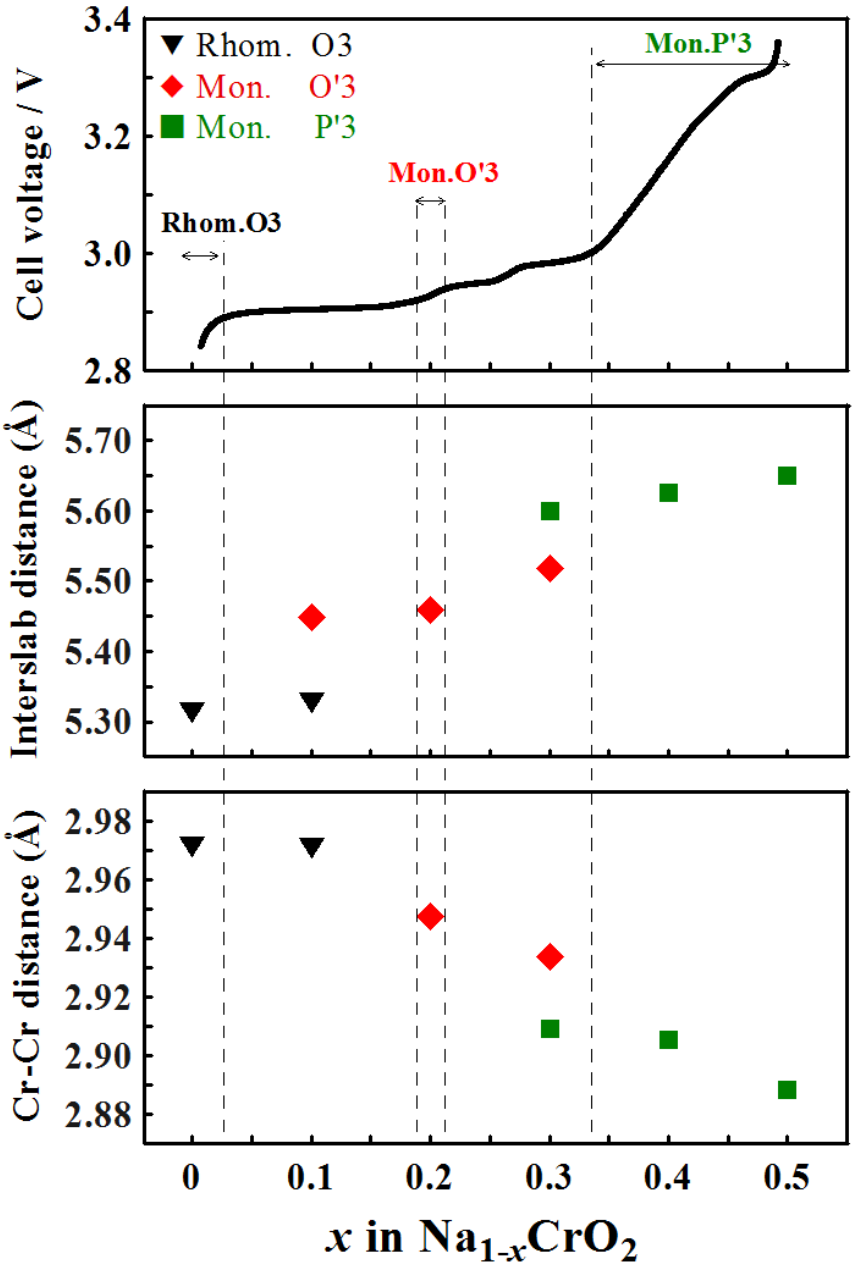

Fig. 3–8 Average Cr-Cr distances (bottom) and interslab distances (middle) of $Na_{1-x}CrO_2$ as a function of the x value, and the charge curve of the $NaCrO_2$/Na[FSA]–K[FSA]/Na cell measured at 5 mA g^{-1} at 363 K (top).

Chapter 4

Pyrophosphate $Na_2FeP_2O_7$ positive electrode in Na[FSA]–K[FSA]

4.1 Introduction

To realize forthcoming large-scale applications expected for Na secondary batteries, the search for suitable electrode and electrolyte materials is still challenging [1–3]. In particular, a battery of long cycle life, low-cost, and high-safety needs to be developed [3]. In Li-ion batteries, polyanionic compounds are receiving growing attention because of the inherent stability of the polyanion group, thus providing a safety asset [4]. Moreover, polyanionic compounds which exchange multiple electrons per transition metal are particularly interesting due to the expectation for realizing a high specific energy [5]. From the viewpoints of cost and mass production, the search for polyanionic compounds containing naturally abundant Fe as a redox center is of timely significance [6]. This has led to intensive studies of olivine $LiFePO_4$ [7], the leading contender as the positive electrode for Li-ion batteries. New compounds such as silicate (Li_2FeSiO_4) [8–10], fluorinated phosphate (Li_2FePO_4F) [11], and pyrophosphate $Li_2FeP_2O_7$ [12–14], have recently been identified to exhibit good electrochemical properties at favorable redox potentials. Compared to well-established materials for Li-ion technology, however, few iron-based polyanionic compounds have been characterized and tested for Na secondary batteries [6, 15–17]. For example, three Na ions can be extracted from the mixed-polyanion compound $Na_4Fe_3(PO_4)_2(P_2O_7)$, resulting in a capacity of 110 mAh g^{-1} with an average voltage of 3.2 V [6]. Very recently, $Na_2FeP_2O_7$ was shown to have a reversible capacity of 82 mAh g^{-1} in $NaClO_4$ dissolved in propylene carbonate (PC) at

room temperature [17].

Concerning Na secondary batteries, however, most research efforts from the scientific community have been focused on electrode materials, whereas the adoption of ionic liquid electrolytes for Na secondary batteries received less attention [18–20]. In this context, the combination of low-cost $Na_2FeP_2O_7$ electrode materials built from abundant elements with affordable Na[FSA]–K[FSA] ionic liquids is extremely interesting to study. Herein, the electrochemical performance of a $Na_2FeP_2O_7$ positive electrode was evaluated by a galvanostatic charge–discharge test in the Na[FSA]–K[FSA] ionic liquid at 363 K. The mechanisms of Na extraction from $Na_2FeP_2O_7$ was also studied by ex-situ X-ray absorption spectroscopy (XAS).

4.2 Experimental

Sodium iron pyrophosphate $Na_2FeP_2O_7$ was synthesized by a two-step solid-state method. The starting materials, Na_2CO_3 (Wako, 99.8%), $FeC_2O_4 \cdot 2H_2O$ (Wako, 99%) and $(NH_4)_2HPO_4$ (Wako, >99%), were thoroughly mixed by wet planetary ball-milling in acetone for 12 h. After evaporating the acetone, the mixture was ground and was initially heated at 573 K for 6 h using the tube furnace shown in Chapter 2. The calcined sample was reground and heated again at 873 K for 12 h. Ar flow was used to suppress the oxidation of Fe^{2+} during the heat treatments.

The working electrode was prepared by mixing as-synthesized $Na_2FeP_2O_7$, acetylene black (AB) conductive additive and polytetrafluoroethylene (PTFE) as binder in a weight ratio of 75:20:5. A metallic sodium disc (Aldrich, 99.95%) were pressed onto nickel current collector and used as the reference and counter electrodes. Na[FSA] and K[FSA] (56:44, molar ratio) was used as the electrolyte. For the galvanostatic intermittent titration technique (GITT) experiments, the cells were charged–discharged at a current density of 4.85 mA g^{-1}

(C/20 rate) for 1 h, and then the circuit was opened until the voltage shift below 10 mV h^{-1}. The theoretical capacity of $Na_2FeP_2O_7$ is defined as 97 mAh g^{-1}, corresponding to one-electron transfer. The variation of electronic structure and local geometric environment of selected materials was characterized by X-ray absorption spectroscopy (XAS), as described in Chapter 2.

4.3 Results and discussion

The XRD pattern and Rietveld refinement results of the $Na_2FeP_2O_7$ sample are shown in Fig. 4–1. This $Na_2FeP_2O_7$ sample exhibits an XRD pattern consistent with that reported in the literature [21] and crystallizes in the space group *P*-1, with a = 6.4299(4) Å, b = 9.4145(8) Å, c = 11.0110(9) Å, α = 64.403(5)°, β = 85.465(3)°, γ = 72.818(3)°, V = 573.39(8) $Å^3$, and Z = 4. No obvious diffraction peaks from impurities were detected. Unit cell parameters are presented in Table 4–1. The crystal structure consists of the corner-sharing FeO_6 octahedra and bridging pyrophosphate groups, thereby creating large tunnel structures along specific directions for facile Na ion migration (Fig. 4–2).

The morphology of the sample was observed by FE–SEM. As shown in Fig. 4–3, as-synthesized $Na_2FeP_2O_7$ particles revealed irregular morphology with diameter ranging from 0.1 to 1 μm and partial aggregation. Tailoring the particle morphology in solid-state synthesis is challenging because experiments conducted at high temperature inevitably lead to particle growth and coarsening. Unlike most of the other polyanion-type positive electrode materials, it was reported that nanosizing is not necessarily required for $Na_2FeP_2O_7$ because it has a high ionic conductivity due to spacious diffusion pathways [16, 17].

Like many pyrophosphate compounds with high thermal stability, $Na_2FeP_2O_7$ showed negligible weight loss and no indication of phase transformation up to 823 K [16]. Thus, $Na_2FeP_2O_7$ is considered to be stable at the present measurement temperature (363 K). The

initial three cycling profiles of $Na_2FeP_2O_7$ (at a current density of 10 mA g^{-1}) are displayed in Fig. 4–4. A shift of the plateau potential was observed from the first to the subsequent charging processes. The subsequent charge–discharge profiles coincided, indicating no major structural change after the first charging. The electrochemical activity centered around 3.0 V is consistent with the reported value, indicating the feasibility of the Na[FSA]–K[FSA] ionic liquid as electrolyte [16, 17]. A reversible capacity of 91 mAh g^{-1} was observed, corresponding to approximately 94% of the theoretical capacity (97 mAh g^{-1}). The observed irreversible potential profile for the first charge has also been reported for $Li_2FeP_2O_7$ and Li_2FeSiO_4 [8–10, 12]. For Li_2FeSiO_4, the observed decrease in the plateau potential by 0.2–0.7 V during the first oxidation was explained by structural ordering processes including the transition from a short-range ordered solid-solution to a more stable phase [8–10]. A similar structural rearrangement is thought to occur in the present study. The working voltage of $Na_2FeP_2O_7$ is similar to that of the Fe^{3+}/Fe^{2+} couple in Na_2FePO_4F (3.0 V) [15] and higher than that of olivine $NaFePO_4$ (2.7 V) [22].

Charge–discharge curves close to the thermodynamic equilibrium were obtained from the galvanostatic intermittent titration technique (GITT) in which each intercalation/deintercalation process is followed by a relaxation period allowing material homogenization. The GITT profiles measured at 4.85 mA g^{-1} (C/20 rate) during the first two cycles are presented in Fig. 4–5. The shape of the curves is very similar to the one obtained under continuous charge–discharge conditions, suggesting facile electrode kinetics with a small overpotential, especially for the Na intercalation process. After the structural rearrangement upon the first charging described above, two distinct regions were observed in the charging profile: a low-voltage region (2.5–3.1 V) and a high-voltage region (>3.1 V). The former region shows a sloping voltage profile with small overpotential; whereas the latter region exhibits a flat voltage plateau with large overpotential. Results of cyclic voltammetry

(CV) consistently exhibit current peaks at the relevant locations (Fig. 4–6). Na ions occupy several crystallographically different sites within $Na_2FeP_2O_7$ [17, 21], and the large overpotential observed in the high-voltage region may be ascribed to the extraction of Na ions located in small channels. These Na ions seem to be rarely re-intercalated because the reversible amount of Na is below one mole per formula. The comparison of the XRD patterns of pristine, fully desodiated, and fully sodiated $Na_2FeP_2O_7$ (Fig. 4–7) indicates that the overall framework of $Na_2FeP_2O_7$ is preserved upon electrochemical cycling.

The rate capability of the $Na_2FeP_2O_7$ electrode is shown in Fig. 4–8. The cell was charged to 4.5 V at a constant current of 5 mA g^{-1} and then discharged to 2.5 V at various current densities. Approximately 66% and 52% of the maximum capacity at 5 mA g^{-1} (90 mAh g^{-1}) were observed at 2000 and 3000 mA g^{-1}, respectively. The discharge capacity is still clearly discernible up to at current density of 4000 mA g^{-1}. The rate capability of $Na_2FeP_2O_7$ cycled in the Na[FSA]–K[FSA] electrolyte at 363 K is significantly better than those obtained in organic electrolytes at room temperature [16, 17]. Moreover, this high rate capability is comparable to that of state-of-the-art electrode materials for Li-ion batteries. For example, $LiFePO_4$, a common Li-ion positive electrode, exhibited about 80% of its theoretical capacity at a 20 C rate [23, 24]. The prominent rate capability obtained here can be attributed to improved kinetics at the elevated temperature and the large-tunnel structure of $Na_2FeP_2O_7$. The cycling performance of $Na_2FeP_2O_7$ at 100 mA g^{-1} (*ca*. 1 C) is shown in Fig. 4–9. It retains 75% of the initial capacity after 3000 cycles. The average coulombic efficiency over the whole experiment was as high as 99.9%. The cyclability of $Na_2FeP_2O_7$ electrodes have also been tested in organic electrolytes, but the results of only limited cycles (< 100 cycles) are reported [16, 17]. It should be noted that this excellent cycle performance was achieved using the $Na_2FeP_2O_7$ electrodes without optimization such as carbon coating. The present result demonstrates that the robust framework and structural integrity of pyrophosphate

allows intercalation/deintercalation of Na ions. Moreover, the high stability of $Na_2FeP_2O_7$ can be fully utilized in conjunction with a chemically stable electrolyte such as the Na[FSA]–K[FSA] ionic liquid.

Although the inductive effect generated by the polyanionic groups leads to a higher operating voltage compared to simple oxides [7], the polyanionic groups simultaneously isolating the valence electrons of transition metals often lead to the observed low electronic conductivities [25]. Consequently, specific material treatments such as carbon-coating [26] and/or resorting to nanoparticles are usually necessary to achieve a high electrochemical performance [4]. However, many manufacturing challenges still prevent achieving high-quality products with high consistency [27]. Furthermore, the volumetric energy density (Wh/L) suffers greatly from the size minimization as most of the nano-sized materials do not have the practical packing scheme yet [28]. In addition to the ease and scalability of the present solid-state synthesis, the prepared samples possess relatively large particle size, which improves the material packing density. The moderately elevated operating temperature and high stability of the Na[FSA]–K[FSA] ionic liquid also suppress the need for electrode optimization.

XAS provided a deep insight into the change of electronic and local structural properties of $Na_2FeP_2O_7$ electrodes upon sodium intercalation/deintercalation. The normalized Fe *K*-edge X-ray absorption near-edge structure (XANES) spectra of the pristine, charged, and discharged $Na_2FeP_2O_7$ are displayed in Fig. 4–10. The XANES spectra of the four investigated samples differ both in the overall shape and the energy position of the main peak. Specifically, the main edge shows a strong shift (*ca*. 4.0 eV) toward higher energy as the charging voltage increases, and vice versa (for the negative shift). This shift of the main edge is explained by screening effects of the 1*s* electrons leading to a stronger bond in the Fe^{3+} state than that in the Fe^{2+} state, suggesting that the reversible Fe^{3+}/Fe^{2+} redox activity is

involved in the electrochemical desodiation/sodiation reaction of $Na_2FeP_2O_7$ [29, 30]. The pre-edge region of the XAS spectra is shown in the inset of Fig. 4–10. The different shapes of the pre-edge resonance for the pristine and charged/discharged $Na_2FeP_2O_7$ samples indicate the irreversible changes in the local environment of Fe in $Na_2FeP_2O_7$ upon electrochemical cycling. The higher pre-edge intensity of the discharged states (sample (d)) compared to that of the charged states (samples (b) and (c)) implies that the coordination around Fe cations deviate from the normal octahedral coordination more severely in the sodiated state than in the desodiated state. Although the electrode was charged up to 4.8 V to explore the possibility of extracting the second Na in $Na_2FeP_2O_7$, no Fe oxidation above +3 was detected (Fig. 4–11). At this point, we can state if this limitation is due to the kinetics or thermodynamics of $Na_2FeP_2O_7$. A more detailed investigation is currently underway.

Fig. 4–12 shows the radial structure functions for the pristine and charged/discharged $Na_2FeP_2O_7$ samples, which have been obtained from Fourier transform (FT) of the extended X-ray absorption fine structure (EXAFS) oscillations. The simulation of the k^3-weighted Fe *K*-edge EXAFS spectra (Fig. 4–13) for the present samples was performed using a limited *k* range (2.2–10.7 $Å^{-1}$) to minimize noise. The radial structure function reveals the scattering contribution of the different atomic shells around the Fe atoms. The first strong peak represents the octahedrally coordinated Fe–O shell, followed by several weaker peaks corresponding to Fe–P and Fe–Fe (not clear in some cases) correlations, respectively. The interatomic distances and corresponding Debye-Waller factors of the samples are shown in the Table 4–2. A decrease of the average Fe–O bond from 2.106 Å (pristine) to 1.979 Å (4.0 V) upon Na extraction is observed, which can be attributed to the oxidation of Fe^{2+} to smaller Fe^{3+} ions as a result of charge compensation. Although the valence state of Fe at the end of discharge (2.7 V) is close to that in the pristine sample, the Fe–O bond length differs by 0.092 Å. Therefore, the EXAFS results verify the structural rearrangement of $Na_2FeP_2O_7$ during the

initial desodiation, which is consistent with the variation of the charge-discharge curves (Fig. 4–4).

4.4 Conclusions

$Na_2FeP_2O_7$ was synthesized via a simple solid-state reaction. The $Na_2FeP_2O_7$ positive electrode showed competent electrochemical properties in the Na[FSA]–K[FSA] ionic liquid at 363 K; a reversible capacity of 91 mAh g^{-1} at 10 mA g^{-1}, an good rate capability of 59 mAh g^{-1} at 2000 mA g^{-1}, and a high capacity retention of 75% after 3000 cycles. XAS studies confirm the reversible change in the Fe oxidation state accompanying a variation of Fe–O bond length upon electrochemical cycling. The evidently improved kinetics of the positive electrode at elevated temperature obviates the need for carbon-coating or nanosizing, which enables lowering the electrode processing cost. The combination of economic positive electrode materials built from abundant elements such as Fe, P, and Na with the safe, purely inorganic ionic liquid electrolytes will pave the way for the large-scale Na secondary batteries.

References

[1] Z.G. Yang, J.L. Zhang, M.C.W. Kintner-Meyer, X.C Lu, D.W. Choi, J.P. Lemmon, J. Liu, Chem. Rev. 111 (2011) 3577–3613.

[2] J. Liu, J.G. Zhang, Z.G. Yang, J.P. Lemmon, C. Imhoff, G.L. Graff, L.Y. Li, J.Z. Hu, C.M. Wang, J. Xiao, G. Xia, V.V. Viswanathan, S. Baskaran, V. Sprenkle, X.L. Li, Y.Y. Shao, B. Schwenzer, Adv. Funct. Mater. 23 (2013) 929–946.

[3] H.L. Pan, Y.S. Hu, L.Q. Chen, Energy Environ. Sci. 6 (2013) 2338–2360.

[4] Z.L. Gong, Y. Yang, Energy Environ. Sci. 4 (2011) 3223–3242.

[5] G. Hautier, A. Jain, H. Chen, C. Moore, S.P. Ong, G. Ceder, J. Mater. Chem. 21 (2011) 17147–17153.

[6] H. Kim, I. Park, D.H. Seo, S. Lee, S.W. Kim, W.J. Kwon, Y.U. Park, C.S. Kim, S. Jeon, K. Kang, J. Am. Chem. Soc. 134 (2012) 10369–10372.

[7] A. Padhi, K. Nanjundaswanmy, J.B. Goodenough, J. Electrochem. Soc. 144 (1997) 1188–1194.

[8] D. Rangappa, K.D. Murukanahally, T. Tomai, A. Unemoto, I. Honma, Nano Lett. 12 (2012) 1146–1151.

[9] A. Nyten, A. Abouimrane, M. Armand, T. Gustafsson, J.O. Thomas, Electrochem. Commun. 7 (2005) 156–160.

[10] Y. Zhao, J.X. Li, N. Wang, C.X. Wu, Y.H. Ding, L.H. Guan, J. Mater. Chem. 22 (2012) 18797–18800.

[11] B.L. Ellis, W.R.M. Makahnouk, Y. Makimura, K. Toghill, L.F. Nazar, Nat. Mater. 6 (2007) 749–753.

[12] S. Nishimura, M. Nakamura, R. Natsui, A. Yamada, J. Am. Chem. Soc. 132 (2010) 13596–13597.

[13] D. Shimizu, S. Nishimura, P. Barpanda, A. Yamada, Chem. Mater. 24 (2012) 2598–2603.

[14] H. Kim, S. Lee, Y.U. Park, H. Kim, J. Kim, S. Jeon, K. Kang, Chem. Mater. 23 (2011) 3930–3937.

[15] Y. Kawabe, N. Yabuuchi, M. Kajiyama, N. Fukuhara, T. Inamasu, R. Okuyama, I. Nakai, S. Komaba, Electrochem. Commun. 13 (2011) 1225–1228.

[16] H. Kim, R.A. Shakoor, C. Park, S.Y. Lim, J.S. Kim, W. Cho, K. Miyasaka, R. Kahraman, Y. Jung, J. W. Choi, Adv. Funct. Mater. 23 (2013) 1147–1155.

[17] P. Barpanda, T. Ye, S. Nishimura, S.C. Chung, Y. Yamada, M. Okubo, H.S. Zhou, A.

Yamada, Electrochem. Commun. 24 (2012) 116–119.
[18] D. Monti, E. Jonsson, M.R. Palacin, P. Johansson, J. Power Sources 245 (2014) 630–636.
[19] S.A.M. Noor, P.C. Howlett, D.R. MacFarlane, M. Forsyth, Electrochim. Acta 114 (2013) 766–771.
[20] L.G. Chagas, D. Buchholz, L.M. Wu, B. Vortmann, S. Passerini, J. Power Sources 247 (2014) 377–383.
[21] P. Barpanda, G. Liu, C.D. Ling, M. Tamaru, M. Avdeev, S.C. Chung, Y. Yamada, A. Yamada, Chem. Mater. 25 (2013) 3480–3847.
[22] S.M. Oh, S.T. Myung, J. Hassoun, B. Scrosati, Y.K. Sun, Electrochem. Commun. 22 (2012) 149–152.
[23] B. Kang, G. Ceder, Nature 458 (2009) 190–193.
[24] G. Ceder, B. Kang, J. Power Sources 194 (2009) 1024–1028.
[25] S.Y. Chung, J.T. Bloking, Y.M. Chiang, Nat. Mater. 1 (2002) 123–128.
[26] N. Ravet, Y. Chouinard, J.F. Magnan, S. Besner, M. Gauthier, M. Armand, J. Power Sources 97–98 (2001) 503–507.
[27] J.J. Wang, X.L. Sun, Energy Environ. Sci. 5 (2012) 5163–5185.
[28] B. Xu, D.N. Qian, Z.Y. Wang, Y.S. Meng, Mat. Sci. Eng. R. 73 (2012) 51–65.
[29] O. Haas, A. Deb, E.J. Cairns, A. Wokaun, J. Electrochem. Soc. 152 (2005) A191–A196.
[30] A. Deb, U. Bergmann, E.J. Cairns, S.P. Cramer, J. Synchrotron. Radiat. 11 (2004) 497–504.

Table 4–1 Atomic coordinates, site occupancies and isotropic atomic displacement parameters of $Na_2FeP_2O_7$ obtained by Rietveld refinement.

Atom	Multiplicity	*x*	*y*	*z*	Occupancy	*U* (Å^2)
Fe(1)	2	0.72829(73)	0.39876(50)	0.21699(40)	1	0.00570(120)
Fe(2)	2	0.64839(63)	–0.00503(50)	0.26342(38)	1	0.00570(120)
P(1)	2	0.57697(117)	0.20236(77)	0.45568(73)	1	0.00601(134)
P(2)	2	0.12641(107)	0.05139(89)	0.30566(69)	1	0.00601(134)
P(3)	2	0.07023(132)	0.32819(95)	0.78692(66)	1	0.00601(134)
P(4)	2	0.29169(111)	0.68887(82)	0.03422(69)	1	0.00601(134)
Na(1)	2	0.03263(142)	0.32298(112)	0.47336(106)	1	0.03071(188)
Na(2)	2	0.39601(157)	0.65625(117)	0.32377(88)	1	0.03071(188)
Na(3)	2	0.21555(148)	0.33944(105)	0.09275(94)	1	0.03071(188)
Na(4)	1	0.5	0	0	0.3333	0.03071(188)
Na(5)	2	0.17622(267)	–0.01947(210)	0.07510(192)	0.5	0.03071(188)
Na(6)	2	0.49403(866)	0.02108(576)	–0.03325(339)	0.3333	0.03071(188)
O(1)	2	0.01361(201)	0.22603(171)	0.29844(127)	1	0.00436(144)
O(2)	2	0.64689(217)	0.36706(182)	0.43310(133)	1	0.00436(144)
O(3)	2	0.32299(208)	0.00949(176)	0.21485(135)	1	0.00436(144)
O(4)	2	0.13136(199)	0.42888(145)	0.84782(128)	1	0.00436(144)
O(5)	2	0.77094(205)	0.04114(165)	0.53597(124)	1	0.00436(144)
O(6)	2	0.28485(231)	0.18505(163)	0.78971(124)	1	0.00436(144)
O(7)	2	0.02661(198)	0.06342(159)	0.68378(125)	1	0.00436(144)
O(8)	2	0.77426(207)	0.39195(158)	0.04026(136)	1	0.00436(144)
O(9)	2	0.43983(206)	0.56698(185)	0.15781(129)	1	0.00436(144)
O(10)	2	0.63251(232)	0.18082(155)	0.04420(126)	1	0.00436(144)
O(11)	2	0.38305(218)	0.18513(152)	0.53103(117)	1	0.00436(144)
O(12)	2	0.55379(236)	0.19433(168)	0.31735(120)	1	0.00436(144)
O(13)	2	0.06915(216)	0.76591(169)	0.10297(134)	1	0.00436(144)
O(14)	2	0.05739(232)	0.58456(157)	0.35364(135)	1	0.00436(144)

Table 4–2 Structural parameters for the $Na_2FeP_2O_7$ electrode determined by Fe K-edge EXAFS: coordination number CN, interatomic distance R (Fe–O), Debye-Waller factor σ^2, and residues.

	CN	R / Å	Error	σ^2 / Å^2	Error	Residue (%)
Pristine	6	2.106	0.011	0.152	0.006	11.544
3.5 V	6	1.974	0.012	0.145	0.006	7.192
4.0 V	6	1.979	0.010	0.131	0.006	2.129
2.7 V	6	2.198	0.012	0.157	0.007	2.698

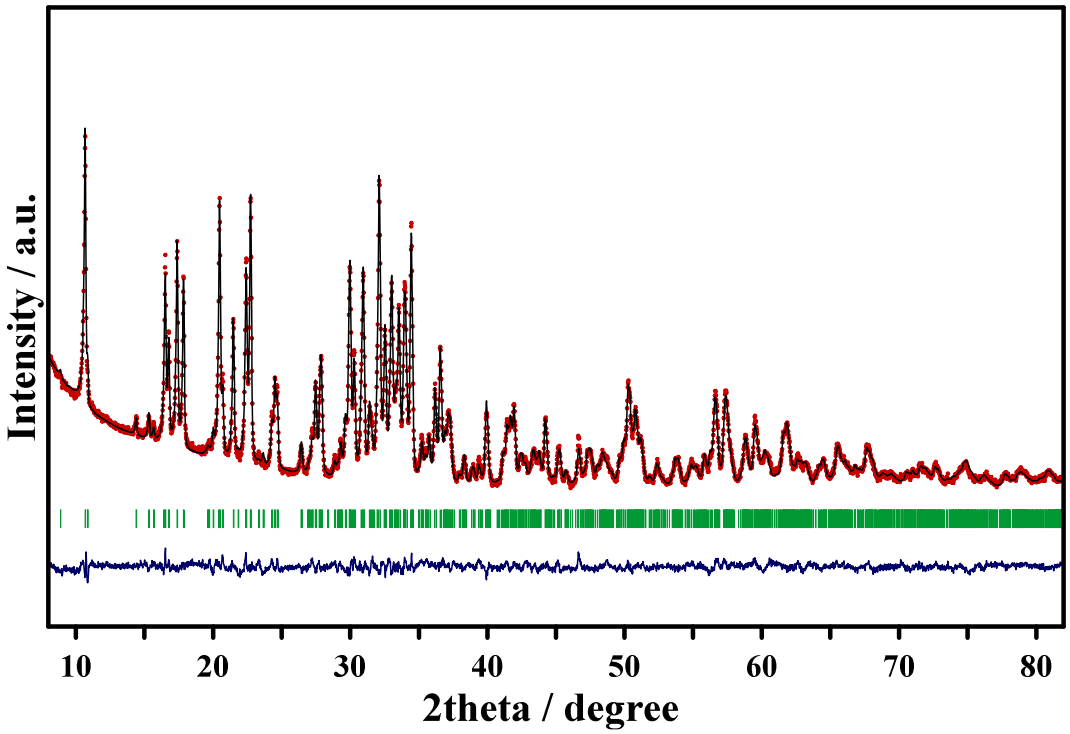

Fig. 4–1 X-ray diffraction with Rietveld refinement of $Na_2FeP_2O_7$ (R_{wp} = 0.93%, R_p = 0.73%, R_F^2 = 1.67%), with the experimental data (red dots), calculated pattern (black line), Bragg positions (green bars), and difference curve (blue line).

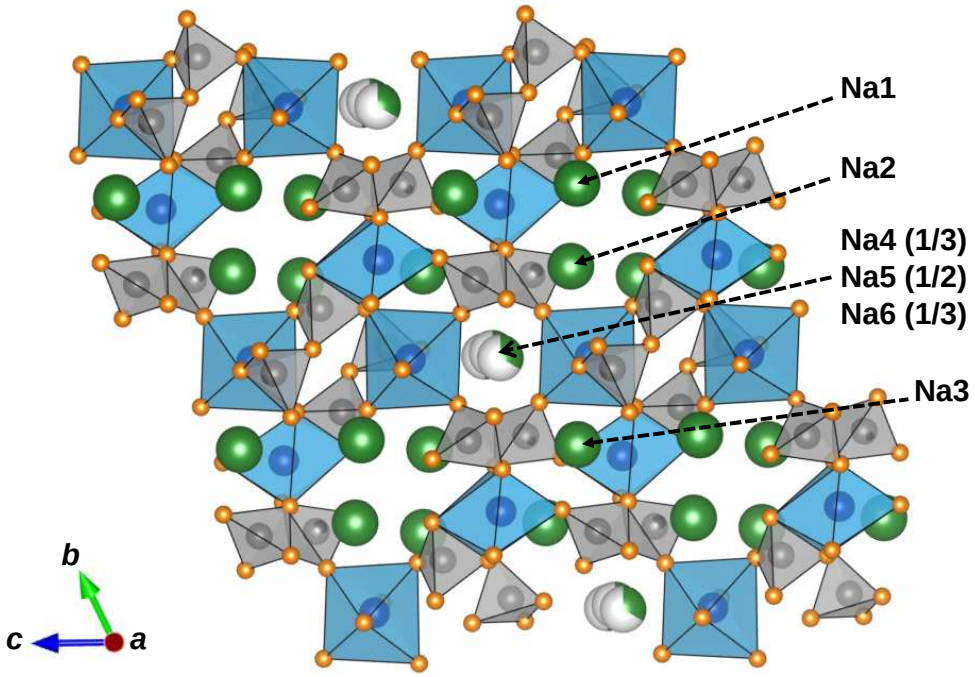

Fig. 4–2 A representative illustration of the crystal structure of $Na_2FeP_2O_7$. The FeO_6 octahedra (blue) and PO_4 tetrahedra (grey) together with Na ions (green) are shown.

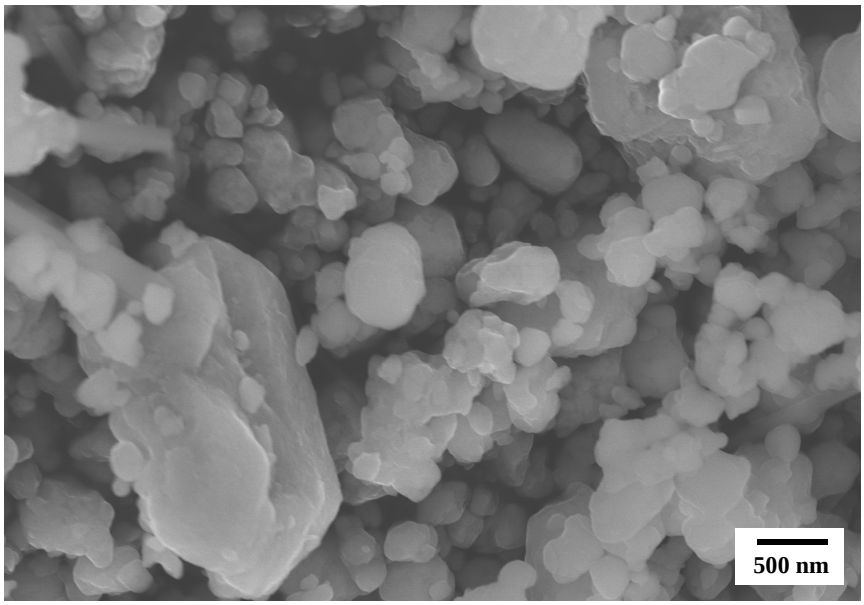

Fig. 4–3 SEM image of the as-prepared $Na_2FeP_2O_7$.

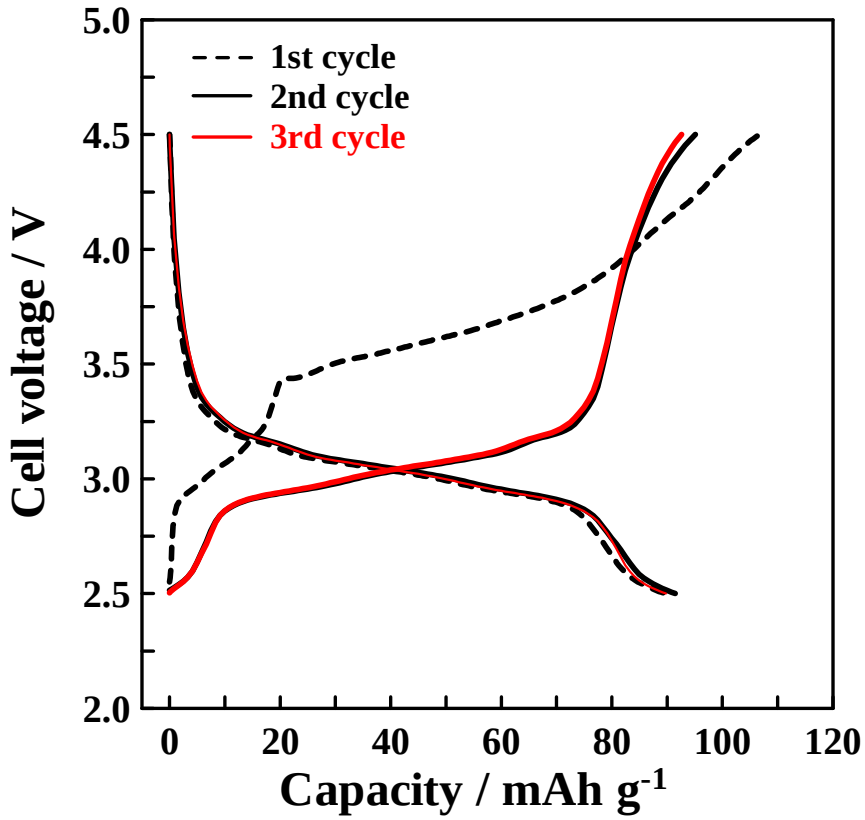

Fig. 4–4 Galvanostatic charge–discharge curves of the initial three cycles for the Na/Na[FSA]–K[FSA]/$Na_2FeP_2O_7$ cell at a current density of 10 mA g^{-1} in the voltage range of 2.5–4.5 V at 363 K.

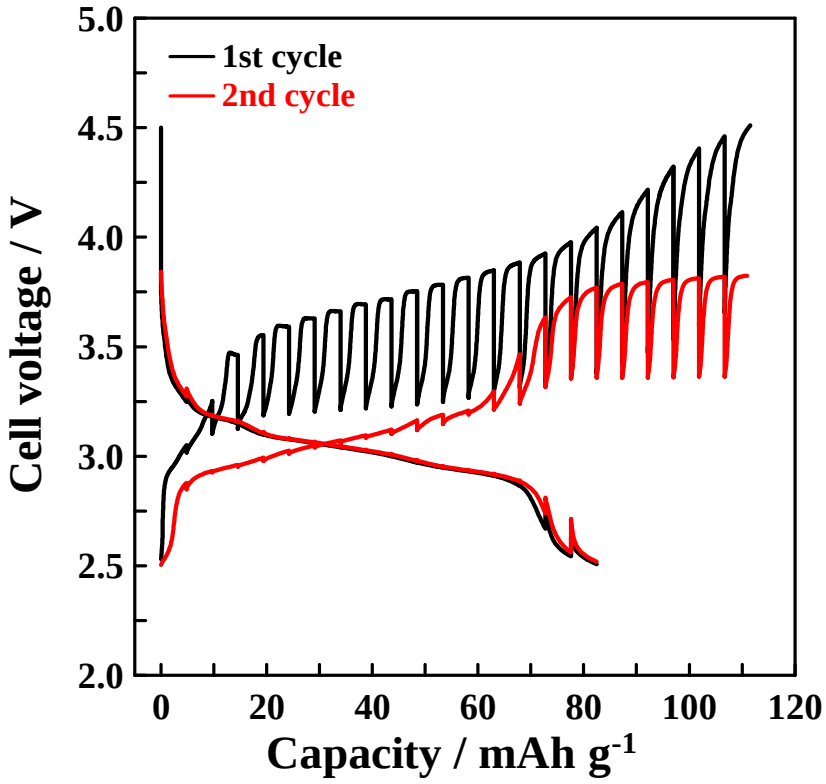

Fig. 4–5 GITT curves for the Na/Na[FSA]–K[FSA]/$Na_2FeP_2O_7$ cell measured at 4.85 mA g^{-1} (C/20 rate) at 363 K.

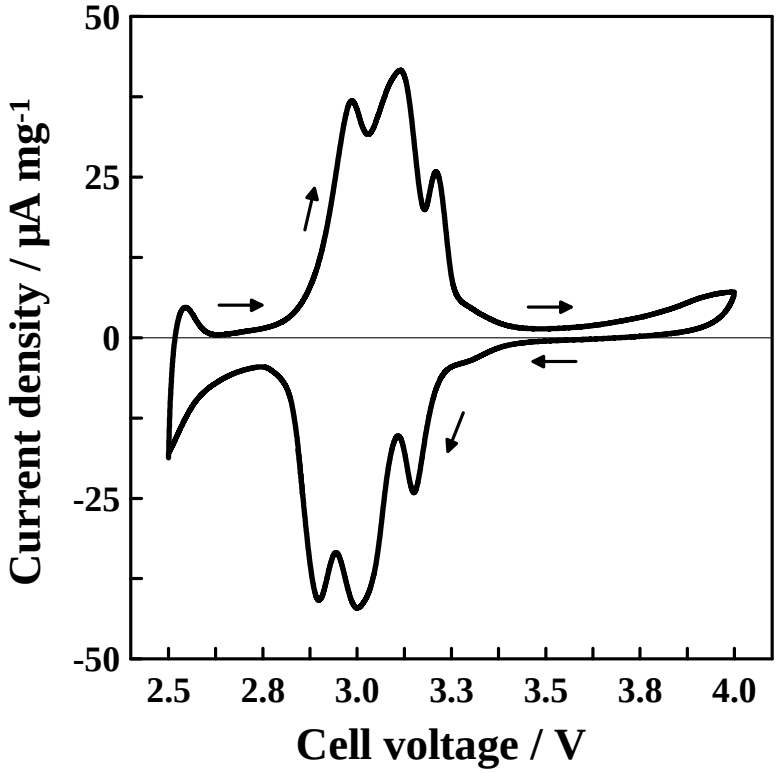

Fig. 4–6 Cyclic voltammogram of the $Na_2FeP_2O_7$ electrode in the Na[FSA]–K[FSA] ionic liquid acquired between 2.5 and 4.0 V at 363 K. Scan rate: 0.05 mV s^{-1}.

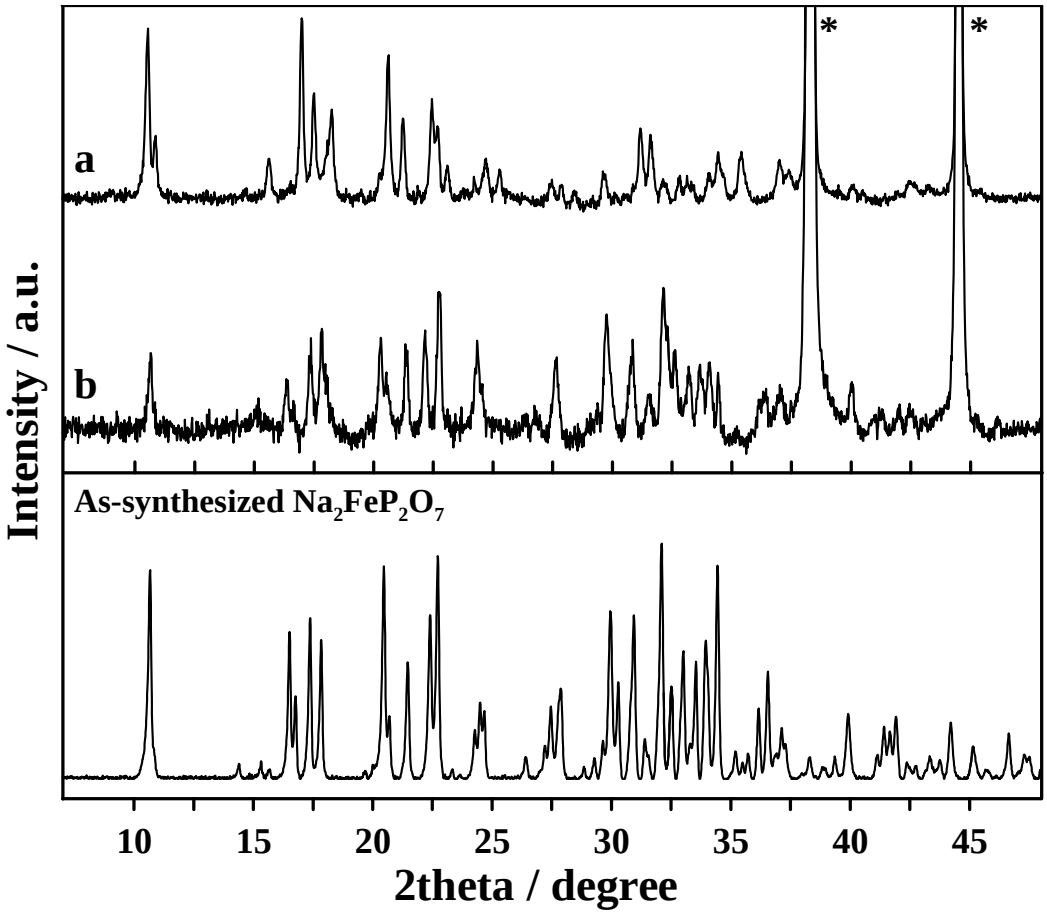

Fig. 4–7 X-ray diffraction patterns of the as-synthesized $Na_2FeP_2O_7$, (a) fully charged $NaFeP_2O_7$ and (b) fully discharged $Na_2FeP_2O_7$. Peaks marked by an asterisk are assigned to the aluminum current collector.

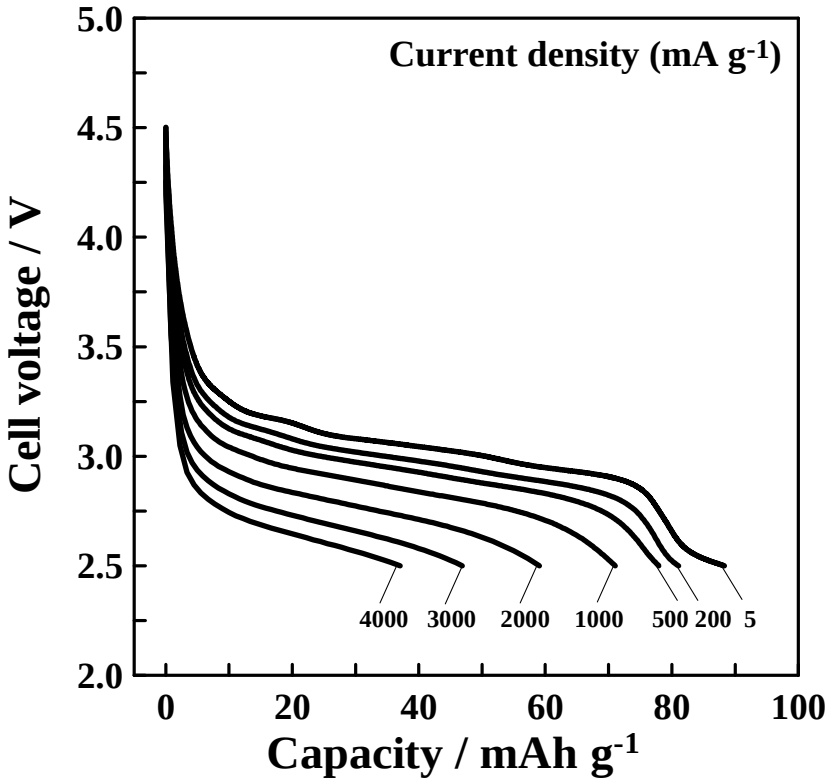

Fig. 4–8 Discharge curves of the $Na_2FeP_2O_7$ electrode at various current densities at 363 K. The charging up to 4.5 V was always conducted at 5 mA g^{-1}.

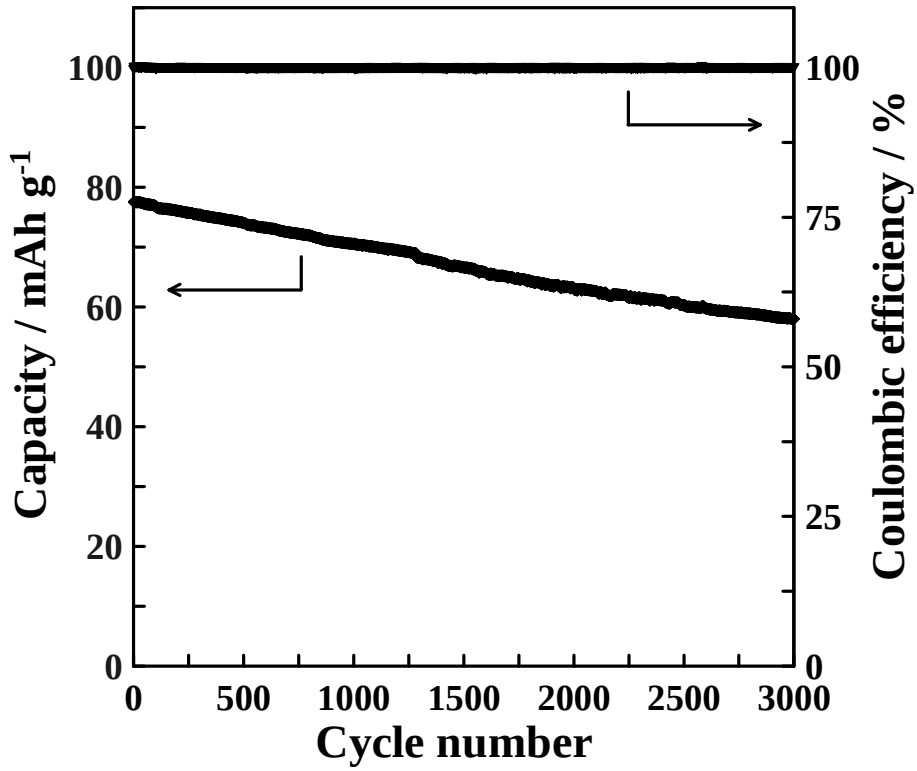

Fig. 4–9 Cycling performance and coulombic efficiency of the $Na_2FeP_2O_7$ electrode at 100 mA g^{-1} and 363 K. Cut-off voltage: 2.5–4.0 V.

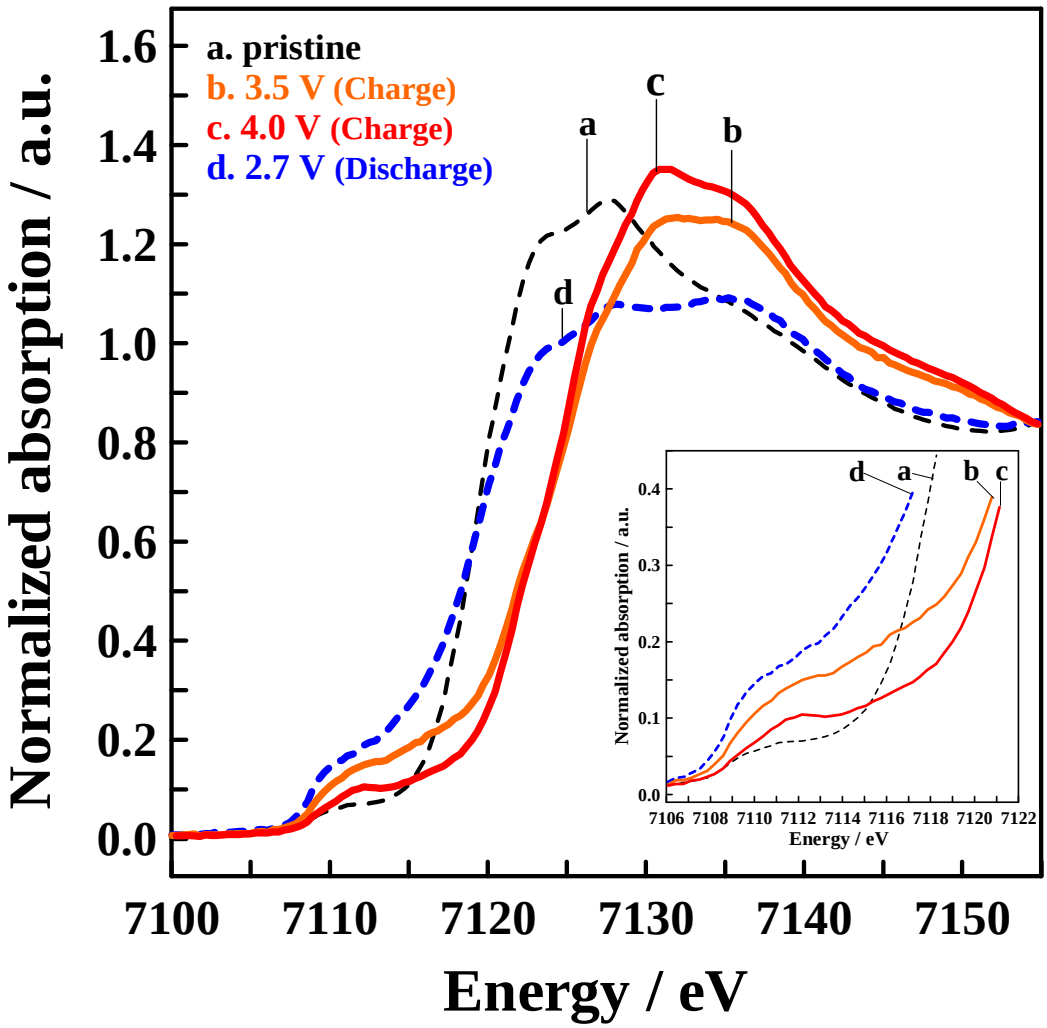

Fig. 4–10 Fe *K*-edge XANES spectra of (a) the pristine $Na_2FeP_2O_7$ and $Na_2FeP_2O_7$ electrodes (b) charged to 3.5 V, (c) charged to 4.0 V, and (d) discharged to 2.7 V. Pre-edge region of the XAS spectra (inset).

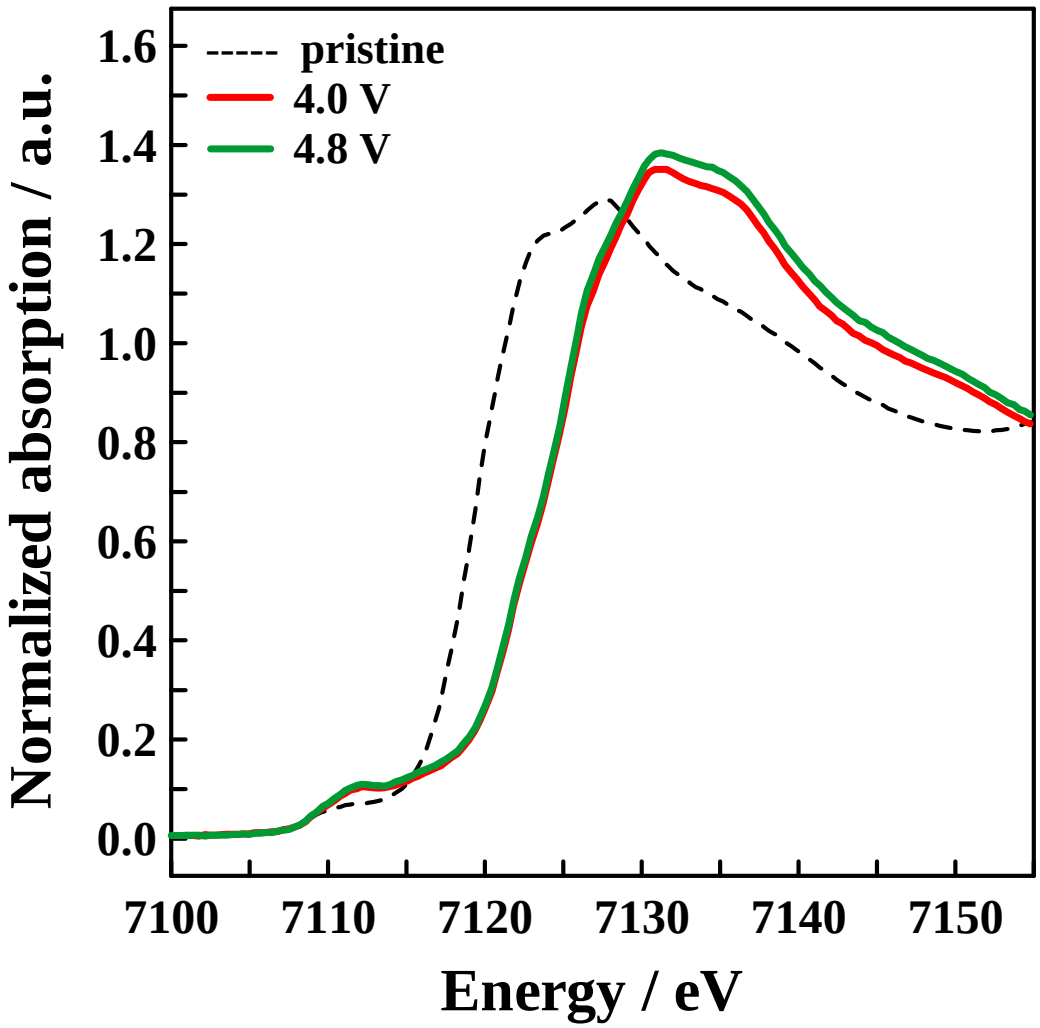

Fig. 4–11 Fe *K*-edge XANES spectra of the pristine $Na_2FeP_2O_7$ and $Na_2FeP_2O_7$ electrodes at different stages of charging.

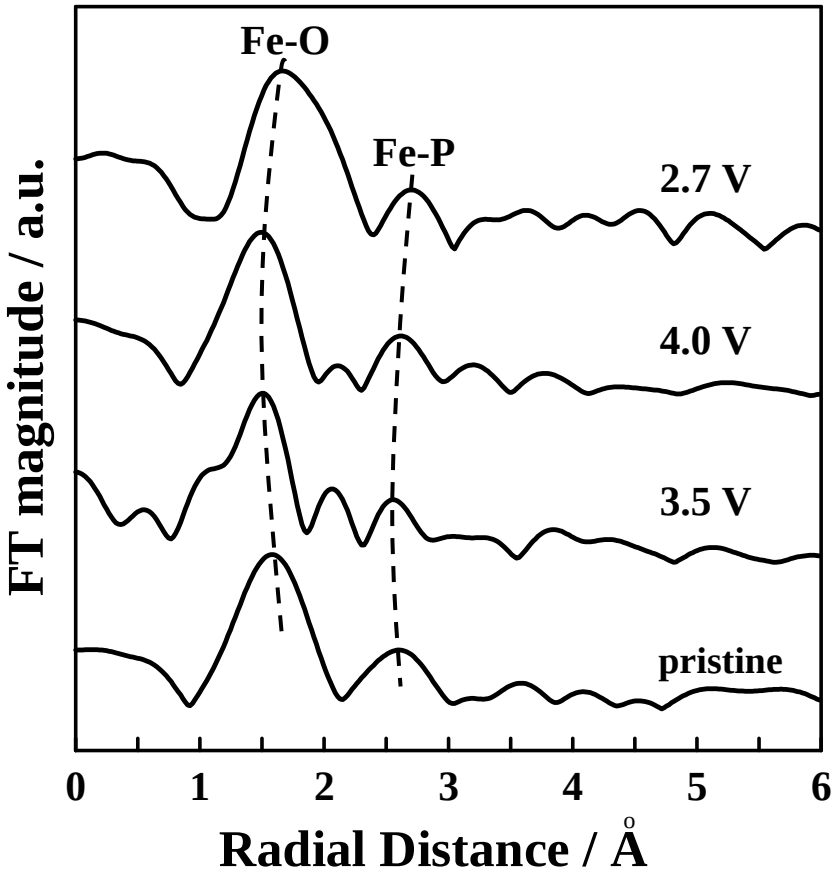

Fig. 4–12 Fourier transformation of Fe *K*-edge EXAFS of the pristine $Na_2FeP_2O_7$ and $Na_2FeP_2O_7$ electrodes at different stages of charging/discharging.

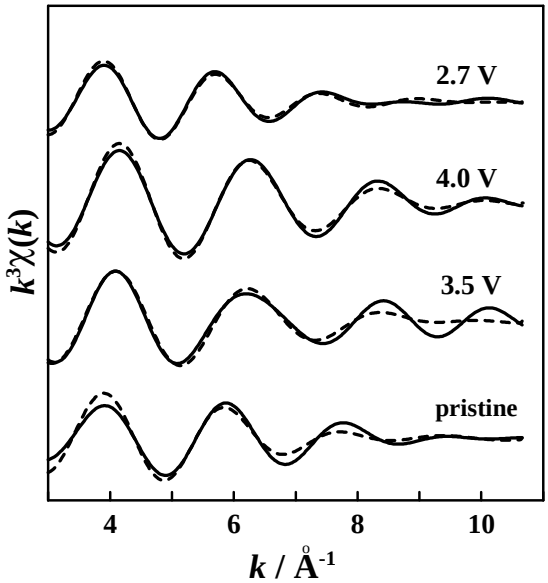

Fig. 4–13 Experimental (solid line) and calculated (dash line) Fourier filtered k^3-weighted Fe *K*-edge extended X-ray absorption fine structure spectra for pristine $Na_2FeP_2O_7$ and $Na_2FeP_2O_7$ electrodes at different stages of charging.

Chapter 5

Pyrophosphate $Na_2FeP_2O_7$ positive electrode in Na[FSA]–[C_3C_1pyrr][FSA]

5.1 Introduction

In Chapter 4, the electrochemical properties of $Na_2FeP_2O_7$ in the Na[FSA]–K[FSA] IL electrolyte has been investigated at 363 K. This positive electrode shows a good rate capability together with an impressive cycle life exceeding 3000 cycles. However, the high melting point (330 K) of the Na[FSA]–K[FSA] IL limits the operation temperature range of its batteries. In an attempt to fulfill the need for room-temperature operation, the Na[FSA]–[C_3C_1pyrr][FSA] (C_3C_1pyrr = *N*-methyl-*N*-propylpyrrolidinium) IL was proposed because of the low melting point (264 K), high conductivity, and good thermal stability of [C_3C_1pyrr][FSA] [1, 2]. It has been demonstrated that the Na[FSA]–[C_3C_1pyrr][FSA] IL (20:80 molar ratio) exhibit an electrochemical window of 5.2 V and an ionic conductivity of 15.6 mS cm^{-1} at 353 K [3]. By utilizing this IL as the electrolyte, good electrochemical properties have been obtained for $NaCrO_2$ positive electrodes over 298–353 K and hard carbon negative electrodes at 363 K [3, 4].

In this chapter, the electrochemical properties of $Na_2FeP_2O_7$ in Na[FSA]–[C_3C_1pyrr][FSA] IL over a wide temperature range of 253–363 K is investigated. The temperature dependence of the rate capability and cyclability from room temperature to 363 K is also examined. The interfacial resistance at the electrode surface is evaluated by electrochemical impedance spectroscopy (EIS).

5.2 Experimental

Sodium iron pyrophosphate $Na_2FeP_2O_7$ was synthesized by a two-step solid-state method as described in Chapter 4. The working electrode was prepared by mixing as-synthesized $Na_2FeP_2O_7$, acetylene black (AB) conductive additive and polytetrafluoroethylene (PTFE) binder in a weight ratio of 75:20:5. A metallic sodium disc (Aldrich, 99.95%) were pressed onto aluminum current collector and used as the reference and counter electrodes. Na[FSA]–[C_3C_1pyrr][FSA] (20:80 molar ratio) IL was used as the electrolyte.

Charge–discharge properties were evaluated using 2032 type coin cells with a Bio-Logic VSP potentiostat in the temperature range 253 to 363 K, as described in Chapter 2. In a typical set of experiments, measurements were first performed on the cells at 363 K at a current density of 20 mA g^{-1} for 5 cycles, after which the temperature was lowered. At each temperature step, charge–discharge tests were performed after equilibration for 2 h. Since a battery may heat up due to delays in cooling, the resulting capacity measurement may depend on the cooling conditions. In this work, the test chamber was equipped with a temperature-controlled active flow of air to avoid this problem. Electrochemical impedance spectroscopy (EIS) measurements were performed as described in Chapter 2. The EIS measurements were taken after several charge–discharge cycles for the Na/Na[FSA]–[C_3C_1pyrr][FSA]/$Na_2FeP_2O_7$ cell and several deposition–dissolution cycles for the Na/Na[FSA]–[C_3C_1pyrrFSA]/Na cell.

5.3 Results and discussion

The initial two cycling profiles of the $Na_2FeP_2O_7$ electrode at a current density of 10 mA g^{-1} at 298 and 363 K are shown in Fig. 5–1. A shift of the plateau potential from the first to the subsequent charging processes is observed for both temperatures. Thereafter,

well-overlapped charge–discharge profiles are observed, reflecting the good reversibility of the $Na_2FeP_2O_7$ electrode. Reversible capacities are 90 and 94 mAh g^{-1} at 298 and 363 K, respectively. Compared to the study using the Na[FSA]–K[FSA] electrolyte (Chapter 4), the electrochemical performance of the $Na_2FeP_2O_7$ electrode shows no apparent difference in these two ionic liquids at 363 K. The differences in the electrochemical features observed between the first cycle and those in subsequent cycles were also reported for the same material tested in organic electrolytes at 298 K, which were ascribed to the presence of Na defects in the initial structure [5].

It is understood that batteries for automotive use must function over a broad temperature range. A reasonable, practical requirement for hybrid electric vehicles (HEVs) and plug-in hybrid electric vehicles (PHEVs) ranges from 243 to 343 K [6]. As shown in Fig. 5–2, the $Na_2FeP_2O_7$ electrode in the Na[FSA]–[C_3C_1pyrr][FSA] electrolyte functions well over a temperature range that spans from 363 K to as low as 253 K. At temperatures greater than 298 K, no appreciable change in the charge–discharge profiles is observed. The reversible capacities are over 90 mAh g^{-1} at a rate of 20 mA g^{-1} (*ca*. C/5) within 298–363 K, which is close to the theoretical capacity. Although larger potential polarization is observed at 253–273 K, 43% of the theoretical capacity can still be delivered at 253 K. Furthermore, its capacity is fully recovered upon returning to 363 K, indicating that cell components remain intact upon cycling in this temperature range. To the best of my knowledge, no other studies have been dedicated to Na battery performance at such extreme temperatures. In this context, the Na[FSA]–[C_3C_1pyrr][FSA] IL represents a promising electrolyte for wide-temperature Na battery applications. Importantly, the upper temperature measureable in this study is limited by the Na metal electrode (m.p.: 371 K). An even higher operating temperature might thereby be expected by utilizing an alternative negative electrode material such as hard carbon [4].

The rate capability of the $Na_2FeP_2O_7$ electrode was evaluated over 298–363 K. The cells

were charged to 4.0 V at a constant current of 10 mA g^{-1} and then discharged to 2.0 V at various current densities. The results are shown in Fig. 5–3. The capacities at 20 mA g^{-1} are 90, 94, 94, and 94 mAh g^{-1} at 298, 323, 348, and 363 K, respectively. Defining these values as the reference capacities (C_0) for each temperature, the ratios between the practical capacity (C) and the reference value are plotted as a function of rate, as shown in Fig. 5–4. No capacity decline is observed when the rate increases from 20 to 200 mA g^{-1} for the cell tested at 363 K, and the value of C/C_0 remains at 87% at 1000 mA g^{-1} (*ca*. 10 C). Even at a very high current rate of 4000 mA g^{-1} (*ca*. 41 C), 53% is still retained. For the cells tested at 348 and 323 K, similarly, almost no capacity decline is observed at 200 mA g^{-1}. At a rate of 1000 mA g^{-1}, the C/C_0 values remain at 82% and 68% at 348 and 323 K, respectively. For the cell measured at 298 K, full capacity is retained at 100 mA g^{-1} but rapidly drops when the current increases to 200 mA g^{-1}. For reference, the charge–discharge curves and the cycle dependence of discharge capacity at high rates of 200, 500 and 1000 mA g^{-1} at 363 K are shown Fig. 5–5. The greatly enhanced rate performance at temperatures higher than 323 K is realized by the use of thermal stable Na[FSA]–[C_3C_1pyrr][FSA] IL, enabling the full utilization of thermal benefits. Although the ionic conductivities of conventional electrolytes also increase as temperatures rise, the evaporation and degradation problems of organic solvents can offset the thermal effects, or even result in deteriorated electrochemical performance [6].

It should be noted that the temperature performance of a battery system is complicated and may not depend on the behavior of a single component. For example, the kinetic limitation at low temperatures may result from solution conductivity, interfacial impedance, or activation-controlled solid-state diffusion [7]. To clarify the rate-limiting factor in the present case, electrochemical impedance measurements were performed on the Na/$Na_2FeP_2O_7$ half cell and the Na/Na symmetric cell using the same electrolyte over 298–363 K. Typical Nyquist plots of the former cell are given in Fig. 5–6a. Each plot consists of a semicircle and

an inclined line on a complex plane. The high frequency limits refer to the bulk electrolyte resistance (R_b). The semicircle at the middle frequency region is derived from the charge-transfer process (R_{ct}) at the electrode/electrolyte interface. The straight line in the low frequency region is attributed to Warburg diffusion associated with finite sodium motion [8]. As shown in Fig. 5–6a, the charge-transfer resistance exhibits a significant sensitivity to temperature. As might have been expected, both R_b and R_{ct} drastically decrease as the temperature is raised, confirming that the transfer of ions in the electrolyte and electrons at the electrode surface is facilitated at elevated temperatures. These findings are consistent with previous studies on Li-ion cells [9, 10]. Nyquist plots of the Na/Na symmetric cell are shown in Fig. 5–6b. The most significant difference from the Na/$Na_2FeP_2O_7$ half cell occurs in the mid-frequency range, namely, the interfacial resistance. A significantly larger interfacial impedance is acquired at 298 and 323 K. Thus, it is concluded that the major component of the R_{ct} observed for the Na/$Na_2FeP_2O_7$ cell originates from the Na counter electrode, especially at lower temperatures. For Li-ion batteries, the formation of an SEI on the lithium metal surface is well accepted in organic electrolytes as well as ionic liquids [11]. It is unclear whether the highly resistive component observed in the present case is associated with the SEI or not.

After the initial electrochemical characterizations, the long-term cycling performance of the $Na_2FeP_2O_7$ electrode was examined at 100 mA g^{-1} (*ca*. 1 C) at 298, 323, and 363 K. As shown in Fig. 5–7, a remarkably stable charge–discharge behavior extending 300 cycles with negligible capacity decay is observed for all temperatures. The average coulombic efficiencies over the whole test are 99.3, 99.9, and 99.6% at 298, 323, and 363 K, respectively. These values further approach 100% at the end of the test, indicating no undesirable side reactions occur, even at elevated temperatures. In a recent report, pristine $Na_2FeP_2O_7$ and its charged states ($NaFeP_2O_7$) were characterized by in situ thermal XRD and thermogravimetric (TG)

analyses [5, 12]. Both studies showed no indication of decomposition, phase transformation, or oxygen evolution up to about 833 K. The excellent thermal stability far exceeds those of layered oxides, which can be attributed to the robust pyrophosphate $(P_2O_7)^{4-}$ building blocks. Furthermore, the full extraction of Na from $Na_2FeP_2O_7$ is accompanied by 2.6% volume shrinkage [12]. This volume change is smaller than that of several positive electrodes such as $LiFePO_4$ (6.8%) [13], Na_2FePO_4F (4%) [14], and $Na_4Fe_3(PO_4)_2(P_2O_7)$ (4%) [15]; thus, an intercalation/deintercalation process with lower strain is expected. These appealing properties can be fully utilized in conjunction with a chemically stable IL electrolyte. The good thermal stability and low melting point of Na[FSA]–[C_3C_1pyrr[FSA] ionic liquid enable the cell to operate at extreme temperatures. The satisfactory electrochemical properties over a wide temperature range demonstrated here are thus originated from both the excellent electrode active material of $Na_2FeP_2O_7$ and the compatible electrolyte of Na[FSA]–[C_3C_1pyrr]FSA. To my knowledge, the $Na_2FeP_2O_7$ electrode tested in the Na[FSA]–[C_3C_1pyrr][FSA] (and Na[FSA]–K[FSA]) IL electrolyte shows the best cycling performance in terms of capacity retention among the reported phosphate-based positive electrode materials for Na secondary batteries, as shown in Chapter 4 and this chapter.

5.4 Conclusions

To enhance safety and extend their operating temperature range, Na batteries utilizing the $Na_2FeP_2O_7$ positive electrode and the Na[FSA]–[C_3C_1pyrr][FSA] ionic liquid electrolyte were proposed. Fairly stable capacity was observed over 253–363 K: a nearly one-electron capacity was delivered for temperatures greater than 298 K, and 43% of their capacity was retained at 253 K. Furthermore, such a cell exhibited satisfactory cyclability and flexibility when operating conditions were switched from low to high rates at 298–363 K. The results obtained

in this work demonstrate that combining the economically viable positive electrode $Na_2FeP_2O_7$ with the nonflammable Na[FSA]–[C_3C_1pyrr][FSA] electrolyte could be a promising platform for the broad spectrum of applications expected for Na secondary batteries.

References

[1] Q. Zhou, W.A. Henderson, G.B. Appetecchi, M. Montanino, S. Passerini, J. Phys. Chem. B 112 (2008) 13577–13580.

[2] M. Kunze, S. Jeong, G.B. Appetecchi, M. Schonhoff, M. Winter, S. Passerini, Electrochim. Acta 82 (2012) 69–74.

[3] C.S. Ding, T. Nohira, K. Kuroda, R. Hagiwara, A. Fukunaga, S. Sakai, K. Nitta, S. Inazawa, J. Power Sources 238 (2013) 296–300.

[4] A. Fukunaga, T. Nohira, R. Hagiwara, K. Numata, E. Itani, S. Sakai, K. Nitta, S. Inazawa, J. Power Sources 246 (2014) 387–391.

[5] H. Kim, R.A. Shakoor, C. Park, S.Y. Lim, J.S. Kim, W. Cho, K. Miyasaka, R. Kahraman, Y. Jung, J. W. Choi, Adv. Funct. Mater. 23 (2013) 1147–1155.

[6] L.S. Plashnitsa, E. Kobayashi, Y. Noguchi, S. Okada, J. Yamaki, J. Electrochem. Soc. 157 (2010) A536–A543.

[7] D. Yaakov, Y. Gofer, D. Aurbach, I.C. Halalay, J. Electrochem. Soc. 157 (2010) A1383–A1391.

[8] A.K. Hjelm, G. Lindbergh, Electrochim. Acta 47 (2002) 1747–1759.

[9] M.C. Smart, B.V. Ratnakumar, K.B. Chin, L.D. Whitcanack, J. Electrochem. Soc. 157 (2010) A1361–A1374.

[10] F. Castiglione, E. Ragg, A. Mele, G.B. Appetecchi, M. Montanino, S. Passerini, J. Phys. Chem. Lett. 2 (2011) 153–157.

[11] N. Byrne, P.C. Howlett, D.R. MacFarlane, M. Forsyth, Adv. Mater. 17 (2005) 2497–2501.

[12] P. Barpanda, G. Liu, C.D. Ling, M. Tamaru, M. Avdeev, S.C. Chung, Y. Yamada, A. Yamada, Chem. Mater. 25 (2013) 3480–3487.

[13] Z.L. Gong, Y. Yang, Energy Environ. Sci. 4 (2011) 3223–3242.

[14] B.L. Ellis, W.R.M. Makahnouk, W.N. Rowan-Weetaluktuk, D.H. Ryan, L.F. Nazar, Chem. Mater. 22 (2010) 1059–1070.

[15] H. Kim, I. Park, D.H. Seo, S. Lee, S.W. Kim, W.J. Kwon, Y.U. Park, C.S. Kim, S. Jeon, K. Kang, J. Am. Chem. Soc. 134 (2012) 10369–10372.

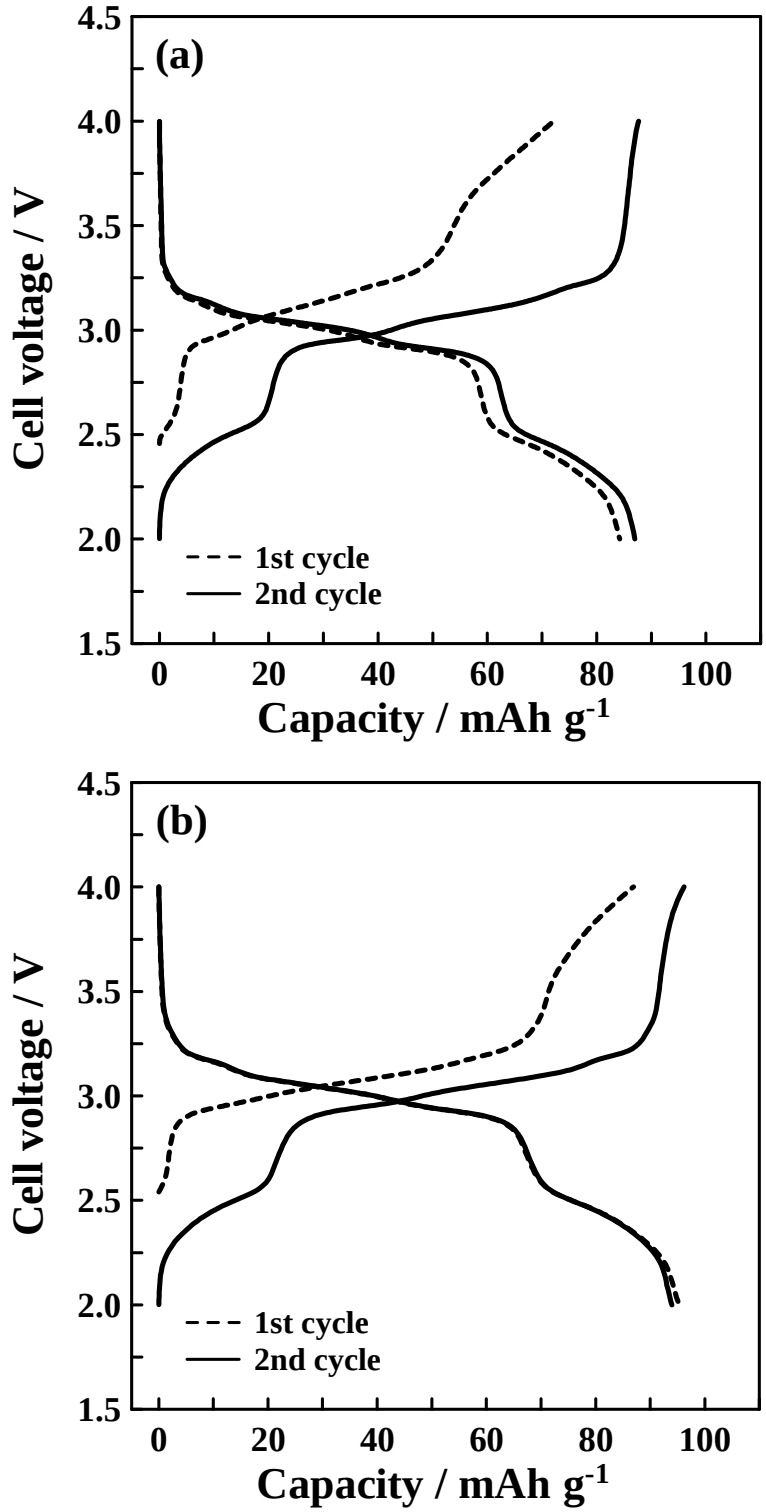

Fig. 5–1 Galvanostatic charge–discharge curves of the initial two cycles for the Na/Na[FSA]–[C_3C_1pyrr][FSA]/$Na_2FeP_2O_7$ cell at a current density of 10 mA g^{-1} in the voltage range of 2.0–4.0 V at (a) 298 K and (b) 363 K.

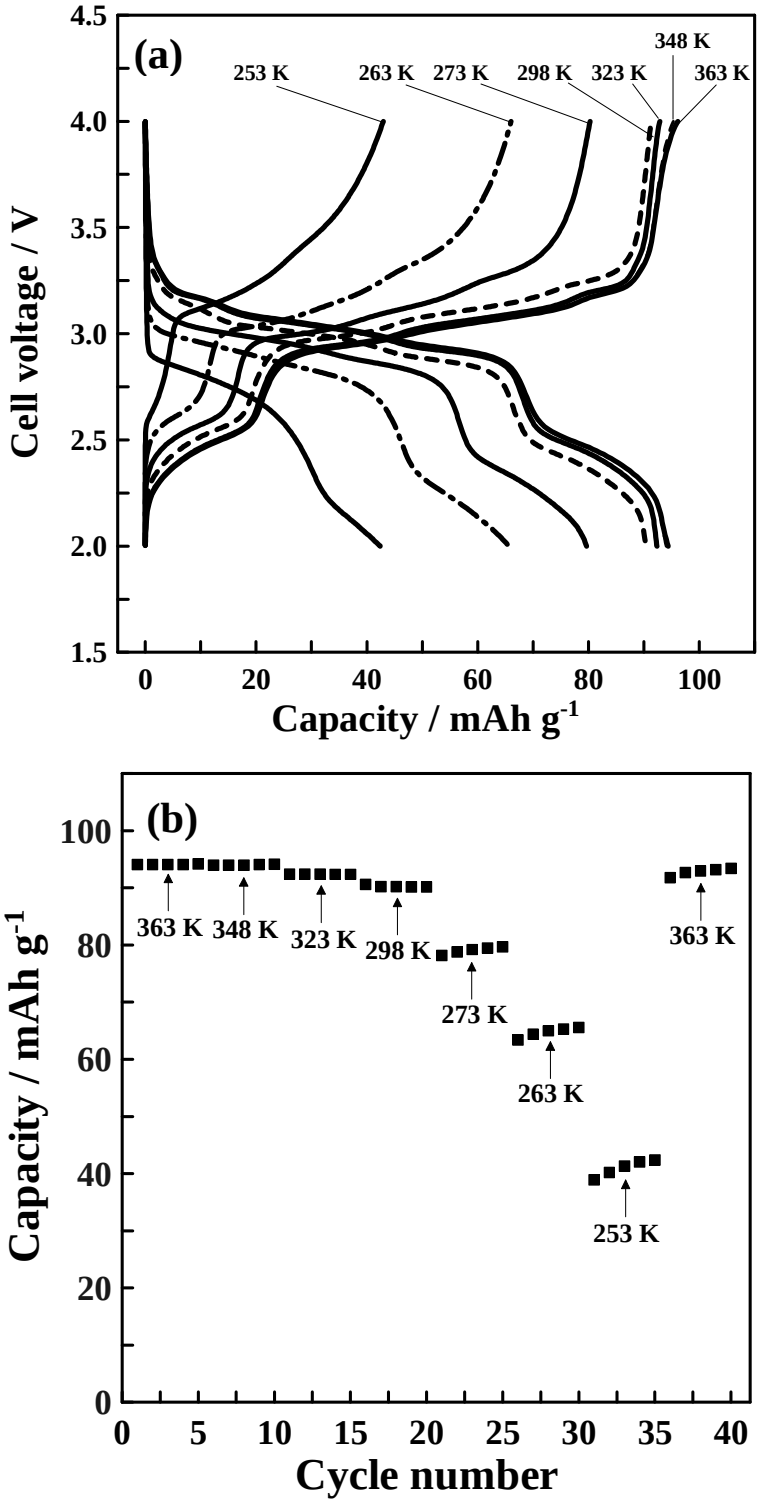

Fig. 5–2 (a) Galvanostatic charge–discharge curves for the Na/Na[FSA]–[C_3C_1pyrr][FSA]/$Na_2FeP_2O_7$ cell at 20 mA g^{-1} over 253–363 K. (b) Discharge capacities of the $Na_2FeP_2O_7$ positive electrode as a function of operating temperature and cycle number. Cut-off voltage: 2.0–4.0 V.

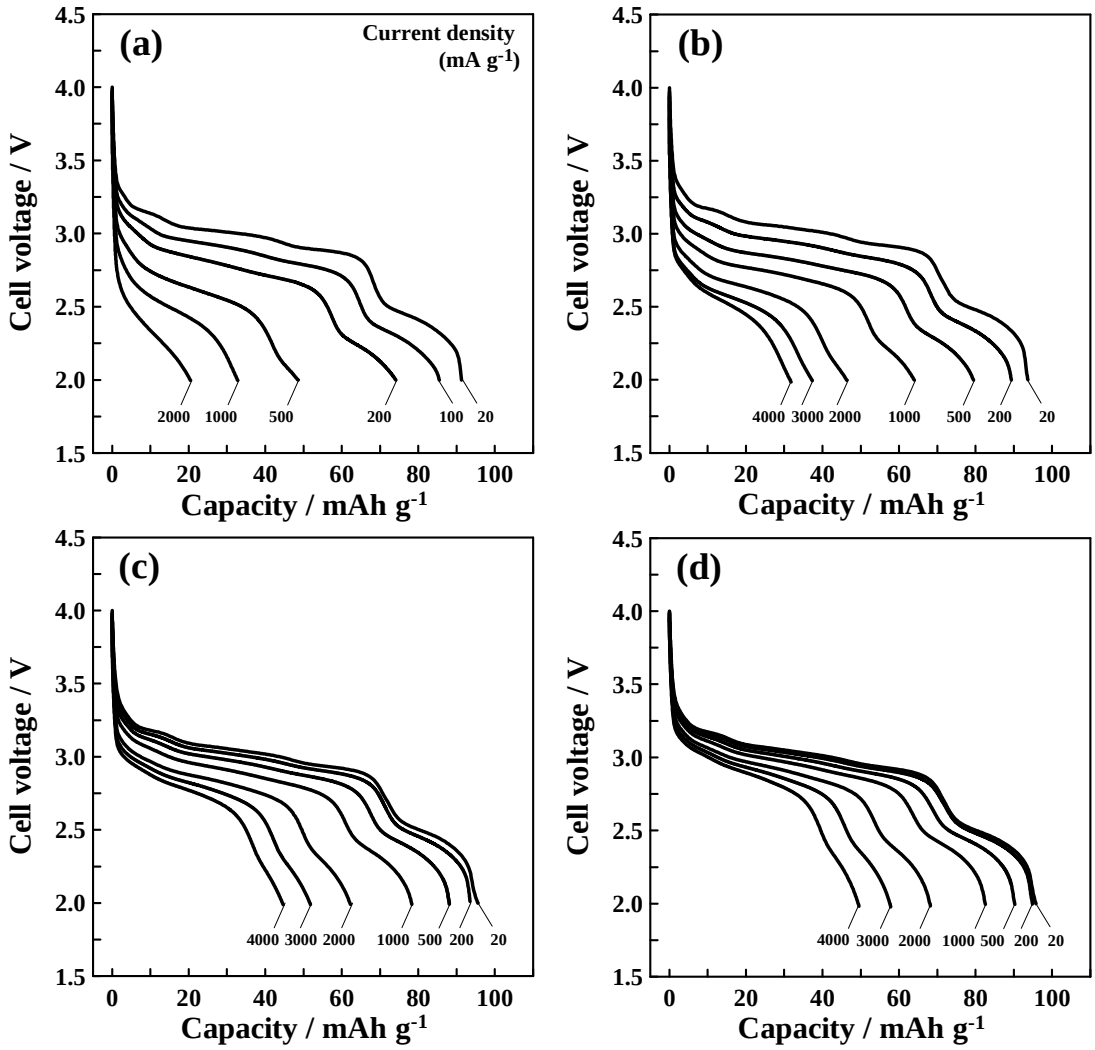

Fig. 5–3 Discharge curves for the Na/Na[FSA]–[C_3C_1pyrr][FSA]/$Na_2FeP_2O_7$ cell at various current densities at (a) 298, (b) 323, (c) 348, and (d) 363 K. The charging was conducted at 10 mA g^{-1}. Cut-off voltage: 2.0–4.0 V.

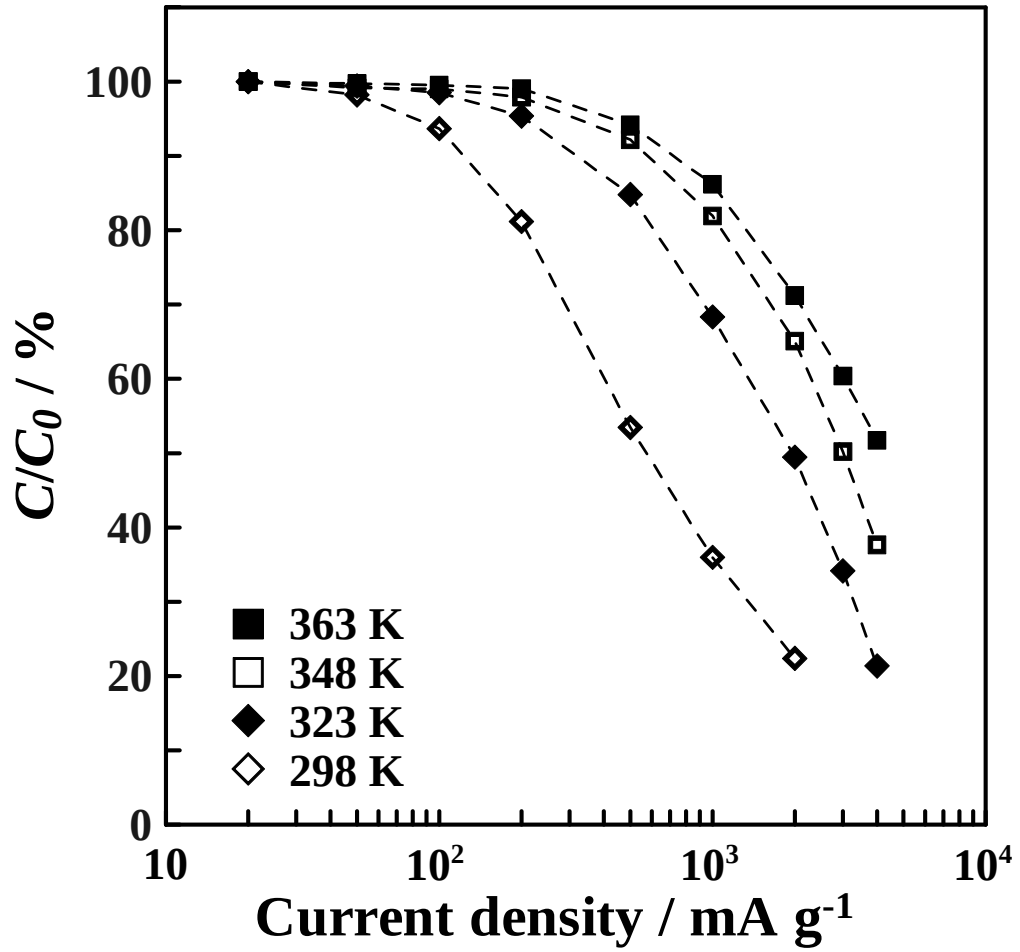

Fig. 5–4 The ratios between the discharge capacity (C) and the reference capacity (C_0) as a function of rate at 298–363 K. The charging was conducted at 10 mA g^{-1}. The reference capacities were 90, 94, 94, and 94 mAh g^{-1} at 298, 323, 348, and 363 K, respectively. Cut-off voltage: 2.0–4.0 V. The dotted lines connecting the capacity data are only guides to the eye.

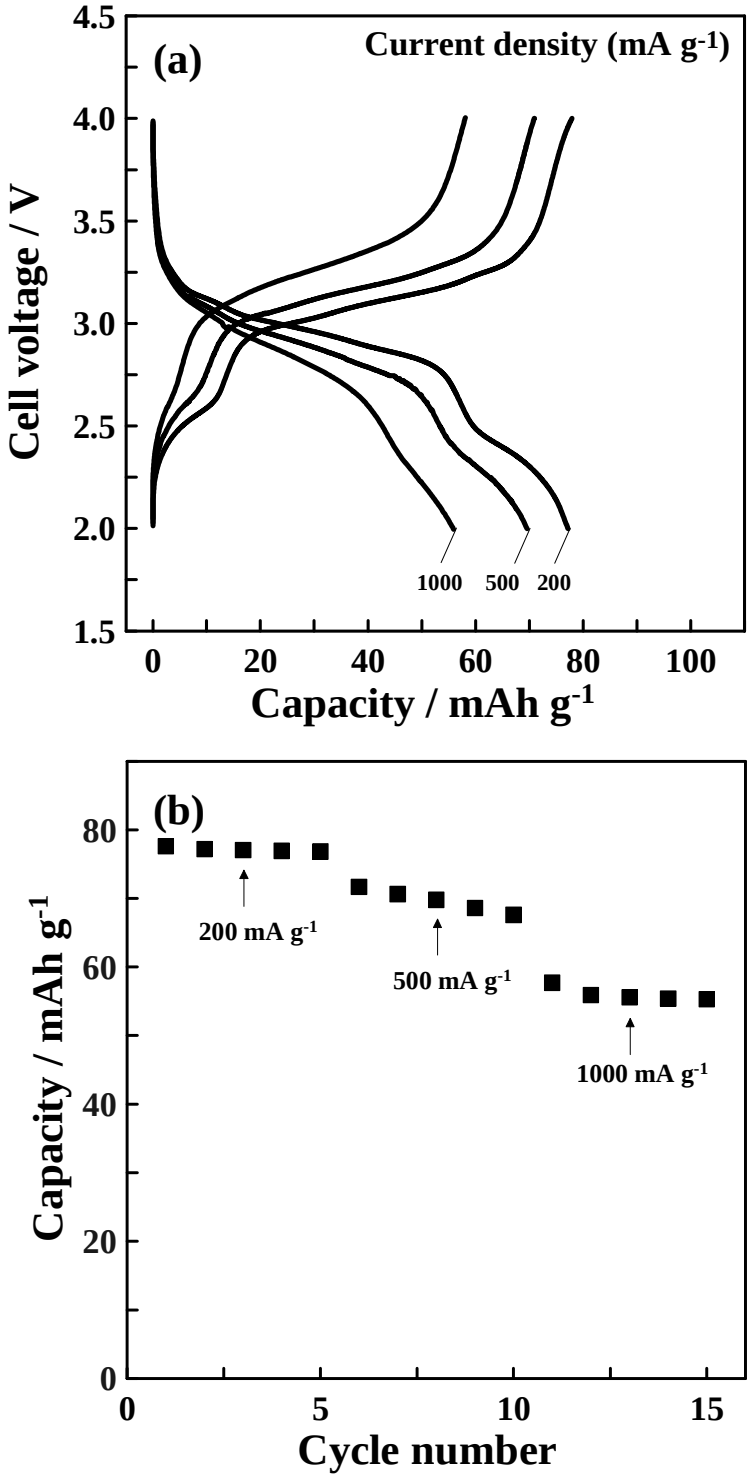

Fig. 5–5 (a) Galvanostatic charge–discharge curves for the Na/Na[FSA]–[C_3C_1pyrr][FSA]/$Na_2FeP_2O_7$ cell at 200, 500, and 1000 mA g^{-1} at 363 K. (b) Discharge capacities of the $Na_2FeP_2O_7$ positive electrode as a function of rate and cycle number.

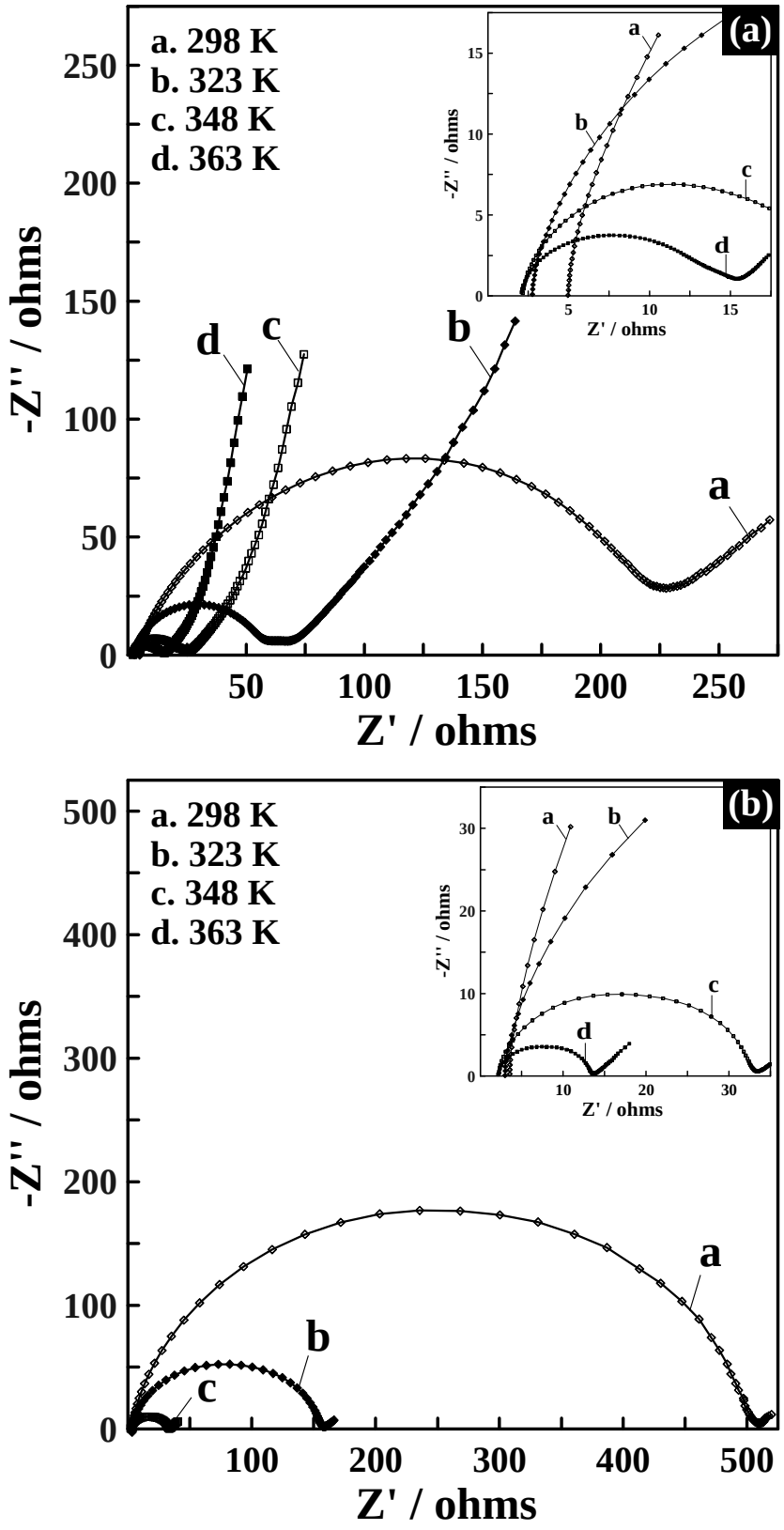

Fig. 5–6 Nyquist plots for (a) the Na/Na[FSA]–[C_3C_1pyrr][FSA]/$Na_2FeP_2O_7$ cell and (b) the Na/Na[FSA]–[C_3C_1pyrr][FSA]/Na symmetric cell at 298–363 K. The AC perturbation was 10 mV, and the frequency range was from 200 kHz to 5 mHz.

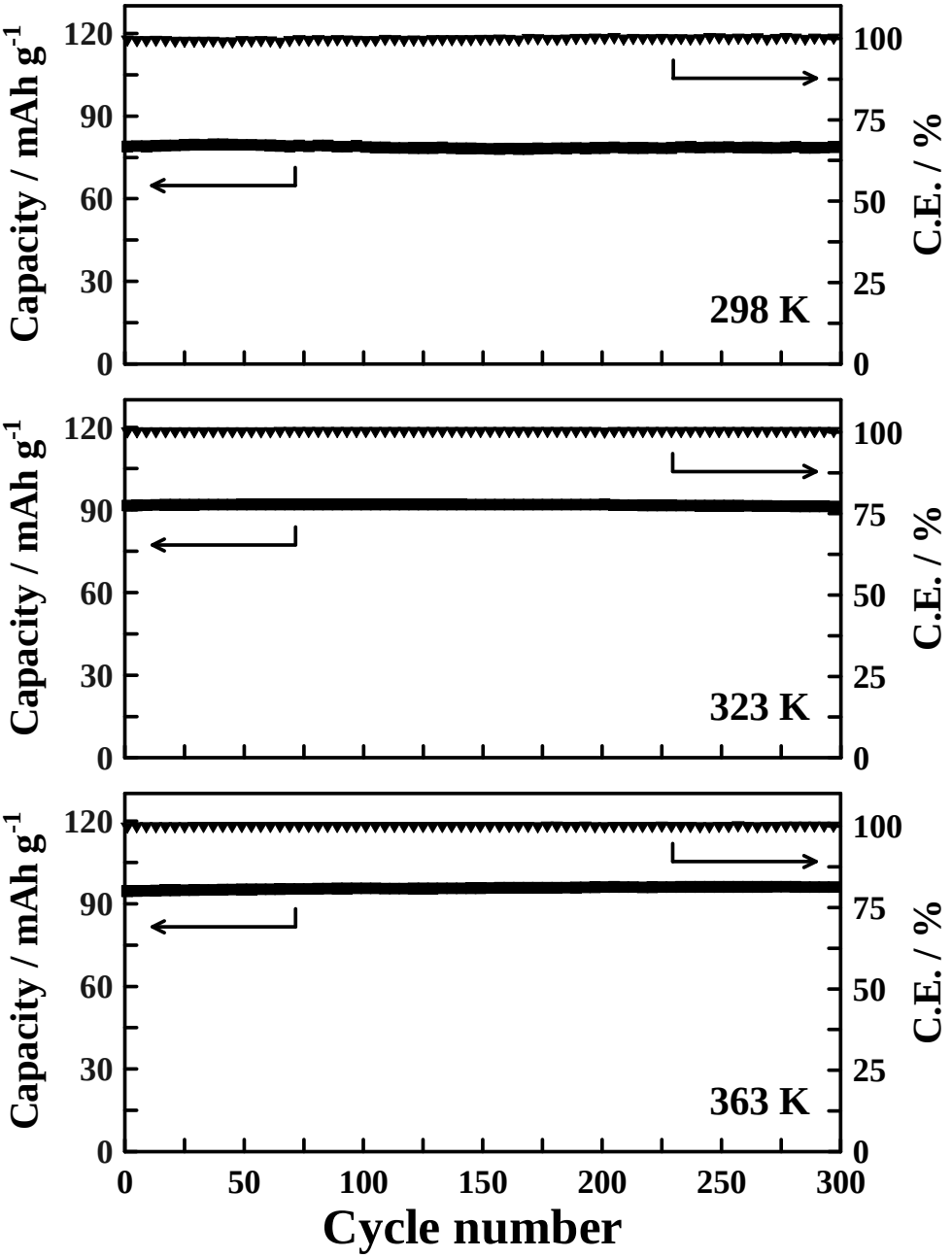

Fig. 5–7 Cycling performance and coulombic efficiency (C.E.) of the $Na_2FeP_2O_7$ positive electrode at 298, 323, and 363 K. Cut-off voltage: 2.0–4.0 V. Current density: 100 mA g^{-1}.

Chapter 6

Pyrophosphate $Na_{2-x}Fe_{1+x/2}P_2O_7$ positive electrode in Na[FSA]–[C_3C_1pyrr][FSA]

6.1 Introduction

As mentioned in Chapter 1, layered oxides Na_xMO_2 (M = transition metal) are generally recognized as one of the most plausible positive electrode candidates for Na secondary batteries [1–6]. However, most of these materials undergo complicated phase transitions and have been shown to possess irreversible structure transition upon cycling [2, 4]. Besides, their long term cyclability and rate capability are insufficient to meet necessary requirements for practical applications [3–5].

In order to overcome such limitations in electrode performance, phosphate-based framework materials have been proposed as positive electrode materials for Na secondary batteries [7–12]. As demonstrated in Chapters 4 and 5, the author has focused on pyrophosphate $Na_2FeP_2O_7$ and studied its electrochemical properties in Na[FSA]–K[FSA] and Na[FSA]–[C_3C_1pyrr][FSA] ionic liquids at 363 K and 253–363 K, respectively. The robust framework undergoes a topotactic Na insertion/extraction reaction with small volume change upon electrochemical cycling, in which the large tunnel provides facile pathways for Na. However, they are less appealing in terms of theoretical capacity (97 mAh g^{-1}) as compared to layered oxides (110–120 mAh g^{-1}) owing to the presence of the P_2O_7 units that induces a weight penalty [13]. Recently, $Na_{2-x}Fe_{1+x/2}P_2O_7$ compounds ($0 < x < 0.44$) were synthesized and evaluated as a positive electrode materials for Na secondary batteries using organic electrolytes at room temperature [14, 15]. The substitution of Na with Fe would

directly influence the active Na sites and the coordination environment of the redox center, resulting in distinct electrochemical characteristics. The electrochemical reaction of $Na_{2-x}Fe_{1+x/2}P_2O_7$ is expressed as following [14]:

$$Na_{2-x}Fe_{1+x/2}(II)P_2O_7 \rightarrow Na_{1-3x/2}Fe_{1+x/2}(III)P_2O_7 + (1 + x/2)(Na^+ + e^-)$$

Notably, the theoretical capacity for the extreme stoichiometric composition, $Na_{1.56}Fe_{1.22}P_2O_7$ (x = 0.44), is estimated to be increased to the highest value of 118 mAh g^{-1}, assuming that 1.22 Na is reversibly intercalated/deintercalated via the redox reaction of 1.22 Fe^{2+}/Fe^{3+}. A comparison between end members of $Na_{2-x}Fe_{1+x/2}P_2O_7$ (i.e., x = 0 and 0.44) is therefore of importance, as it would provide an avenue for the electrochemical properties of the pyrophosphates to be maximized through composition design. However, the full theoretical capacity of $Na_{1.56}Fe_{1.22}P_2O_7$ has not realized so far. The reversible capacity values typically reported in the literature are *ca*. 85 mAh g^{-1} and generally include only reports of limited cycles [14, 15].

In this Chapter, the electrochemical properties of $Na_{1.56}Fe_{1.22}P_2O_7$ in the Na[FSA]–[C_3C_1pyrr][FSA] IL at 298–363 K are investigated and compared to those of $Na_2FeP_2O_7$ under the same experimental conditions, in order to understand the effect of altering the stoichiometric ratio of Na to Fe, in a polyanion-type positive electrode. The dependence of the rate capability and the cyclability of these electrodes on temperature are also examined.

6.2 Experimental

Sodium iron pyrophosphates $Na_{2-x}Fe_{1+x/2}P_2O_7$ (x = 0 and 0.44) were synthesized through a two-step solid-state method as described in Chapter 4, but with different Na/Fe stoichiometric ratios. The working electrode was prepared by mixing as-synthesized

$Na_{1.56}Fe_{1.22}P_2O_7$, acetylene black (AB) conductive additive and polytetrafluoroethylene (PTFE) as binder in a weight ratio of 75:20:5. A metallic sodium disc (Aldrich, 99.95%) were pressed onto aluminum current collector and used as the reference and counter electrodes. Na[FSA]–[C_3C_1pyrr][FSA] (20:80 molar ratio) IL was used as the electrolyte. Charge–discharge properties were evaluated using 2032 type coin cells with a Bio-Logic VSP potentiostat, as described in Chapter 2.

6.3 Results and discussion

Although $Na_{1.56}Fe_{1.22}P_2O_7$ was first synthesized and characterized using single crystal X-ray diffraction by Angenault *et al*. in 1995 [16], no electrochemical data was reported in that work. The XRD pattern and Rietveld refinement results of as-synthesized $Na_{1.56}Fe_{1.22}P_2O_7$ are shown in Fig. 6–1. The $Na_{1.56}Fe_{1.22}P_2O_7$ sample crystallizes in the space group *P*-1, with a = 6.4215(3) Å, b = 9.390(4) Å, c = 10.978(4) Å, α = 64.546(10)°, β = 86.091(12)°, γ = 73.013(13)°, V = 569.8(4) Å^3, and Z = 4. Unit cell parameters are presented in Table 6–1. The lattice parameters of $Na_{1.56}Fe_{1.22}P_2O_7$ are in good agreement with previously reported microcrystalline and single crystal data [15, 16]. No obvious diffraction peaks from impurities are detected.

A compositional analysis of the as-synthesized $Na_{2-x}Fe_{1+x/2}P_2O_7$ (x = 0 and 0.44) were conducted using ICP-AES and AAS. The results are presented in Table 6–2. The atomic ratios are Na:Fe:P = 1.97:0.998:2 for $Na_2FeP_2O_7$ (x = 0) and Na:Fe:P = 1.47:1.22:2 for $Na_{1.56}Fe_{1.22}P_2O_7$ (x = 0.44). The consistency between analytical result and the expected compound verifies the feasibility of the solid-state method adopted. The morphology of $Na_{1.56}Fe_{1.22}P_2O_7$ was observed by FE-SEM. As shown in Fig. 6–2, $Na_{1.56}Fe_{1.22}P_2O_7$ possesses broad size distribution ranging from hundreds of nanometers to a few micrometers. No distinct difference in the morphology is found when compared to that of $Na_2FeP_2O_7$.

A comparative study of the crystal structures of $Na_{1.56}Fe_{1.22}P_2O_7$ and $Na_2FeP_2O_7$ reveals the similarities and the differences between them. According to the structural models proposed for $Na_{1.56}Fe_{1.22}P_2O_7$ and $Na_2FeP_2O_7$[10, 16], both the compounds possess a similar framework in which the FeO_6 octahedra interconnect with the P_2O_7 units resulting in three-dimensional and large interstitial spaces through which Na ions can diffuse (Fig. 6–3). On the other hand, compared to $Na_2FeP_2O_7$, the occupancy of Na6 sites is reduced to 0 and the occupancy of Na4 sites is increased from 0.333 to 0.882 in the case of $Na_{1.56}Fe_{1.22}P_2O_7$. The Na5 sites are partially occupied by Fe with an occupancy of 0.118 in addition to one Na site in the large tunnel along the *a* axis (Na1) being partly replaced by Fe in $Na_{1.56}Fe_{1.22}P_2O_7$, whereas no site mixing is found in $Na_2FeP_2O_7$. The presence of co-occupied sites results in a much larger mean value for the cation–oxygen bond length compared to that of the other FeO_6 units (r_{Na}^{+} = 1.02 Å > r_{Fe}^{2+} = 0.78 Å) [16]. Therefore, polyhedral units are considered to be more distorted in $Na_{1.56}Fe_{1.22}P_2O_7$ than in $Na_2FeP_2O_7$.

The initial two cycling profiles of the $Na_{1.56}Fe_{1.22}P_2O_7$ electrode at a current density of 10 mA g^{-1} at 298, 323, 348, and 363 K are shown in Fig. 6–4. The shift of the plateau potential from the first charging curve to the subsequent charging curves becomes small as temperature rises. The absence of the plateau at 2.5 V for the cell tested at 298 K may be due to the slow kinetics of desodiation at lower temperature. Besides, well-overlapped charge–discharge profiles are observed for all temperatures investigated, reflecting the good reversibility of the $Na_{1.56}Fe_{1.22}P_2O_7$ electrode. Reversible capacities are 90, 99, 107, and 108 mAh g^{-1} at 298, 323, 348, and 363 K, respectively. The capacity (90 mAh g^{-1}) is slightly higher than that tested in organic electrolytes (85 mAh g^{-1}) under the same 298 K, which could be explained by the successful synthesis as well as the use of chemically stable IL electrolyte [14]. More importantly, the highest capacity of 108 mAh g^{-1} has been obtained for the first time by the elevation of temperature to 363 K. This result confirms that a moderately elevated operating

temperature can effectively enhance the utilization ratio of active materials, resulting in a higher capacity.

In comparison with $Na_2FeP_2O_7$, $Na_{1.56}Fe_{1.22}P_2O_7$ clearly shows better electrochemical characteristics (Fig. 6–5). At 298 K, the $Na_{1.56}Fe_{1.22}P_2O_7$ electrode exhibits a smooth charge–discharge profile, a smaller voltage shift during the first charging cycle, and a reversible capacity of 90 mAh g^{-1}. At 363 K, the voltage shift for the $Na_{1.56}Fe_{1.22}P_2O_7$ electrode becomes almost negligible and the reversible capacity is evidently improved by 15% (108 mAh g^{-1}), which corresponds to approximately 92% of the theoretical capacity based on the one-electron reaction. The well-overlapped feature of the first and the second charging curves implies that $Na_{1.56}Fe_{1.22}P_2O_7$ may be more resistant to atmospheric poisoning, resulting in better preservation of the initial stoichiometry. Notably, the voltage profiles of $Na_{1.56}Fe_{1.22}P_2O_7$ and $Na_2FeP_2O_7$ also exhibit a pronounced difference. While two distinguishable voltage plateaus are observed at 2.5 V and 3.0 V in the case of $Na_2FeP_2O_7$, for $Na_{1.56}Fe_{1.22}P_2O_7$ the plateau at 2.5 V becomes narrower while a new plateau appears at 3.8 V (Fig. 3b). The distinct voltage profiles imply that the active Na intercalation/deintercalation sites of the two compounds are altered as the ratio of Na to Fe is varied. The results also indicate that the operating voltage is influenced by the local environment of the polyanions [17]. An upward shift in the discharge curves is observed for $Na_{1.56}Fe_{1.22}P_2O_7$, leading to a higher average operating voltage.

The mechanisms by which Na is extracted from $Na_{1.56}Fe_{1.22}P_2O_7$ were studied by ex-situ XRD. Fig. 6–6 indicates that the XRD patterns of three samples (a) as-synthesized, (b) fully charged, and (c) fully discharged $Na_{1.56}Fe_{1.22}P_2O_7$ show no significant differences, confirming that the overall framework of $Na_{1.56}Fe_{1.22}P_2O_7$ is preserved during electrochemical cycling. There are no apparent evidences for the formation of a new phase in the fully charged state, indicating that the $Na_{1.56}Fe_{1.22}P_2O_7$ electrode undergoes reactions in a single-phase. This

finding is in agreement with previous report in which a series form of $Na_{1.56-x}Fe_{1.22}P_2O_7$ was prepared via chemical sodiation and desodiation [15].

The rate capability of the $Na_{1.56}Fe_{1.22}P_2O_7$ electrode was evaluated over 298–363 K. The cells were charged up to 4.0 V at a constant current density of C/10 (11.8 mA g^{-1}) and then discharged down to 2.0 V at various rates. The obtained discharge curves are shown in Fig. 6–7. The discharge capacities are plotted as a function of discharge rate at various temperatures in Fig. 6–8. The capacities decrease with increasing current densities for all the cells because the reactions are kinetically constrained at high rates. Nevertheless, the capacity remains its 77%, 89% and 90% when the rate increased from C/5 to 10 C for the cells tested at 323, 348 and 363 K. The reversible capacities at 363 K are 106, 97, 88, 78, and 64 mAh g^{-1} at current rates of 2 C, 10 C, 20 C, 30 C and 40 C, respectively. By contrast, the capacity rapidly dropped when the current density increased up to 2 C for the one measured at 298 K. In previous chapters, it has been demonstrated that the transfers of ions in the electrolyte and electrons at the electrode surface are facilitated at elevated temperatures. Moreover, it has been indicated that the rate-limiting factor for the half cell at intermediate temperature (298 and 323 K) originates from the Na counter electrode, rather than the positive electrode side.

The long term cycling performance of the $Na_{1.56}Fe_{1.22}P_2O_7$ electrode at 1 C (118 mA g^{-1}) at 298, 323, and 363 K is shown in Fig. 6–9. A considerably stable cycle behavior with negligible capacity decay (< 1.5%) over 300 cycles is observed. The average coulombic efficiencies over the whole test are 99.9, 99.8, and 99.7% at 298, 323, and 363 K, respectively, indicating no undesirable side reaction occurs. Moreover, at a rate as high as 20 C (2360 mA g^{-1}) at 363 K, 71% of the initial capacity is retained after 3000 cycles, as shown in Fig 6–10. The average coulombic efficiency is as high as 99.95%. It was reported that the volume change between the fully desodiated and sodiated $Na_{1.56}Fe_{1.22}P_2O_7$ was 1.9% [15], which is extremely small compared with other phosphate-based materials including $NaFePO_4$ (17.6%)

[18], $Na_3V_2(PO_4)_3$ (8.3%) [19], $Na_4Fe_3(PO_4)_2P_2O_7$ (4%) [20], and $Na_2FeP_2O_7$ (2.6%) [10]. The outstanding cyclability is likely attributed to the negligible volume variation of the rigid pyrophosphate framework that is less sensitive to Na insertion/extraction. Furthermore, a chemically stable IL electrolyte Na[FSA]–[C_3C_1pyrr][FSA] would also contribute to the long cycle life. This result is reminiscent of the well-known zero-strain $Li_4Ti_5O_{12}$ electrode for Li secondary batteries, confirming the importance of the small volume change in achieving high cycle stability [21]. Although the theoretical capacity of $Na_{1.56}Fe_{1.22}P_2O_7$ is less than recently reported layered oxides positive electrodes [3–5], the rate capability and cyclability achieved here obviously surpasses them.

6.4 Conclusions

By altering the Na/Fe stoichiometric ratio, $Na_{2-x}Fe_{1+x/2}P_2O_7$ (x = 0 and 0.44) have been successfully synthesized and their electrochemical properties have been investigated in the Na[FSA]–[C_3C_1pyrr][FSA] IL at 298–363 K. $Na_{1.56}Fe_{1.22}P_2O_7$ exhibits a reversible capacity of 108 mAh g^{-1} at 363 K, which is 15% improved compared with that of $Na_2FeP_2O_7$ under the same condition. Moreover, good rate capability and cyclability over 3000 cycles are achieved for $Na_{1.56}Fe_{1.22}P_2O_7$. The high performance positive electrode materials consisting of earth abundant Fe, P, and Na is promising for the future widespread use of Na secondary batteries. It is also expected that more superior polyanionic compounds will be developed through composition design.

References

[1] D. Hamani, M. Ati, J.M. Tarascon, P. Rozier, Electrochem. Commun. 13 (2011) 938–941.

[2] R. Berthelot, D. Carlier, C. Delmas, Nat. Mater. 10 (2011) 74–80.

[3] S. Komaba, C. Takei, T. Nakayama, A. Ogata, N. Yabuuchi, Electrochem. Commun. 12 (2012) 355–358.

[4] S. Komaba, N. Yabuuchi, T. Nakayama, A. Ogata, T. Ishikawa, I. Nakai, Inorg. Chem. 51 (2012) 6211–6220.

[5] N. Yabuuchi, M. Kajiyama, J. Iwatate, H. Nishikawa, S. Hitomi, R. Okuyama, R. Usui, Y. Yamada, S. Komaba, Nat. Mater. 11 (2012) 512–517.

[6] J. Billaud, G. Singh, A.R. Armstrong, E. Gonzalo, V. Roddatis, M. Armand, T. Rojob, P.G. Bruce, Energy Environ. Sci. 7 (2014) 1387–1391.

[7] P. Serras, V. Palomares, J. Alonso, N. Sharma, J.M.L. del Amo, P. Kubiak, M.L. Fdez-Gubieda, T. Rojo, Chem. Mater. 25 (2013) 4917–4925.

[8] K. Saravanan, C.W. Mason, A. Rudola, K.H. Wong, P. Balaya, Adv. Energy Mater. 3 (2013) 444–450.

[9] P. Barpanda, T. Ye, S. Nishimura, S.C. Chung, Y. Yamada, M. Okubo, H.S. Zhou, A. Yamada, Electrochem. Commun. 24 (2012) 116–119.

[10] P. Barpanda, G. Liu, C.D. Ling, M. Tamaru, M. Avdeev, S.C. Chung, Y. Yamada, A. Yamada, Chem. Mater. 25 (2013) 3480–3487.

[11] H. Kim, R.A. Shakoor, C. Park, S.Y. Lim, J.S. Kim, W. Cho, K. Miyasaka, R. Kahraman, Y. Jung, J. W. Choi, Adv. Funct. Mater. 23 (2013) 1147–1155.

[12] P. Barpanda, T. Ye, M. Avdeev, S.C. Chung, A. Yamada, J. Mater. Chem. A 1 (2013) 4194–4197.

[13] C. Wurm, M. Morcrette, G. Rousse, L. Dupont, C. Masquelier, Chem. Mater. 14 (2002) 2701–2710.

[14] T. Honma, N. Ito, T. Togashi, A. Sato, T. Komatsu, J. Power Sources 227 (2013) 31–34.

[15] K.H. Ha, S.H. Woo, D. Mok, N.S. Choi, Y. Park, S.M. Oh, Y. Kim, J. Kim, J. Lee, L.F. Nazar, K.T. Lee, Adv. Energy Mater. 3 (2013) 770–776.

[16] J. Angenault, J.C. Couturier, M. Quarton, F. Robert, Eur. J. Solid State Inorg. Chem. 32 (1995) 335–343.

[17] S.W. Kim, D.H. Seo, X.H. Ma, G. Ceder, K. Kang, Adv. Energy Mater. 2 (2012)

710–721.

[18] M. Casas-Cabansa, V.V. Roddatis, D. Saurel, P. Kubiak, J. Carretero-Gonzalez, V. Palomares, P. Serras, T. Rojo, J. Mater. Chem. 22 (2012) 17421–17423.

[19] Z.L. Jian, W.Z. Han, X. Lu, H.X. Yang, Y.S. Hu, J. Zhou, Z.B. Zhou, J.Q. Li, W. Chen, D.F. Chen, L.Q. Chen, Adv. Energy Mater. 3 (2013) 156–160.

[20] H. Kim, I. Park, D.H. Seo, S. Lee, S.W. Kim, W.J. Kwon, Y.U. Park, C.S. Kim, S. Jeon, K. Kang, J. Am. Chem. Soc. 134 (2012) 10369–10372.

[21] T. Ohzuku, A. Ueda, N. Yamamoto, J. Electrochem. Soc. 142 (1995) 1431–1435.

Table 6–1 Atomic coordinates, site occupancies and isotropic atomic displacement parameters of $Na_{1.56}Fe_{1.22}P_2O_7$ obtained by Rietveld refinement.

Atom	Multiplicity	*x*	*y*	*z*	Occupancy	*U* (Å^2)
Na(1)	2	0.2048(18)	–0.1326(14)	0.5980(12)	1	0.042(2)
Na(2)	2	0.4125(19)	0.1560(12)	–0.1656(10)	1	0.042(2)
Na(3)	1	0.5	0.5	0.5	0.882	0.042(2)
Na(4)	2	–0.0297(11)	0.1744(8)	0.0215(7)	0.677	0.013(2)
Fe(1)	2	0.3477(8)	0.5104(7)	0.2324(6)	1	0.0192(15)
Fe(2)	2	0.2739(8)	0.0995(5)	0.2803(5)	1	0.0192(15)
Fe(3)	2	0.856(6)	0.400(5)	0.403(3)	0.118	0.0192(15)
Fe(4)	2	–0.0297(11)	0.1744(8)	0.0215(7)	0.323	0.013(2)
P(1)	2	–0.0777(14)	0.1619(12)	0.7304(8)	1	0.0258(18)
P(2)	2	0.2863(13)	0.1942(10)	0.5381(9)	1	0.0258(18)
P(3)	2	0.5814(14)	0.7048(10)	–0.0363(8)	1	0.0258(18)
P(4)	2	0.8532(15)	0.4594(12)	0.2028(10)	1	0.0258(18)
O(1)	2	0.081(2)	0.2722(17)	0.6149(14)	1	0.0046(2)
O(2)	2	0.748(3)	0.529(2)	0.0517(165)	1	0.0046(2)
O(3)	2	–0.077(3)	0.0365(18)	0.6659(13)	1	0.0046(2)
O(4)	2	-0.291(3)	0.324(2)	0.6862(13)	1	0.0046(2)
O(5)	2	0.069(2)	0.1067(17)	0.8617(16)	1	0.0046(2)
O(6)	2	0.422(3)	0.0949(17)	0.6383(16)	1	0.0046(2)
O(7)	2	0.173(3)	0.1087(18)	0.4653(16)	1	0.0046(2)
O(8)	2	0.346(3)	0.3291(18)	0.4341(16)	1	0.0046(2)
O(9)	2	0.669(2)	0.8783(18)	–0.0571(13)	1	0.0046(2)
O(10)	2	0.563(2)	0.7234(19)	–0.2159(14)	1	0.0046(2)
O(11)	2	0.362(2)	0.6897(16)	0.0289(12)	1	0.0046(2)
O(12)	2	1.048(3)	0.5315(18)	0.1843(16)	1	0.0046(2)
O(13)	2	0.983(3)	0.3546(19)	0.1532(16)	1	0.0046(2)
O(14)	2	0.699(3)	0.4399(19)	0.2929(14)	1	0.0046(2)

Table 6–2 ICP-AES compositional analysis for the as-synthesized $Na_{2-x}Fe_{1+x/2}P_2O_7$ (x = 0 and 0.44).

	Weight (%)			Atomic ratio[a]		
	Na	Fe	P	Na	Fe	P
x = 0	15.5	19.1	21.2	1.97	0.998	2
x = 0.44	11.7	23.7	21.4	1.47	1.22	2

[a] Calculated as P was normalized to 2.

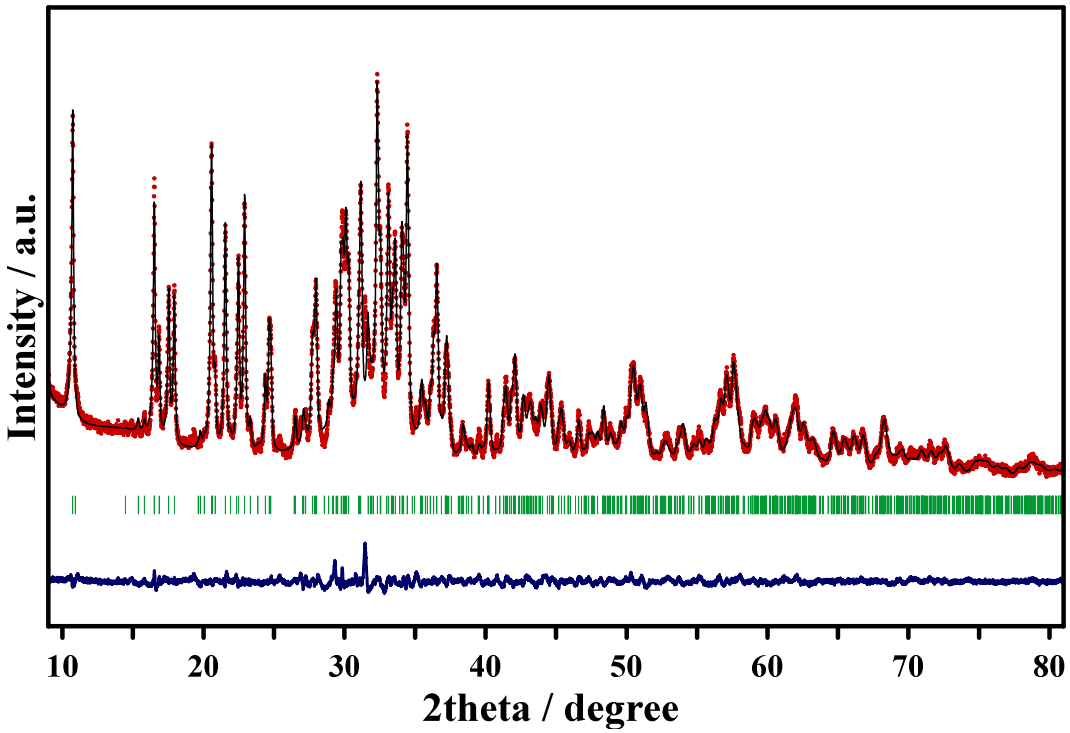

Fig. 6–1 X-ray diffraction with Rietveld refinement of $Na_{1.56}Fe_{1.22}P_2O_7$ (R_{wp} = 0.88%, R_p = 0.60%) with the experimental data (red dots), calculated pattern (black line), Bragg positions (green bars) and the difference curve (blue line).

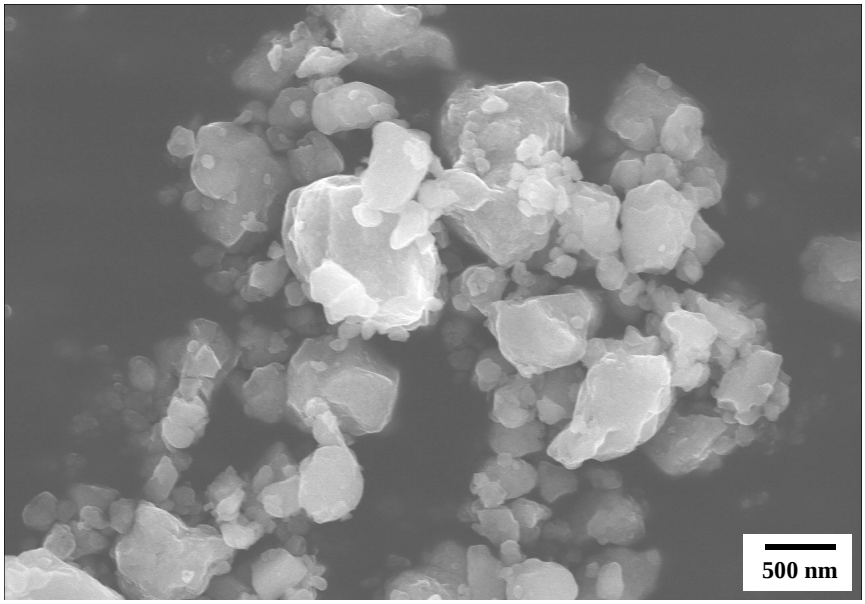

Fig. 6–2 SEM image of the as-prepared $Na_{1.56}Fe_{1.22}P_2O_7$.

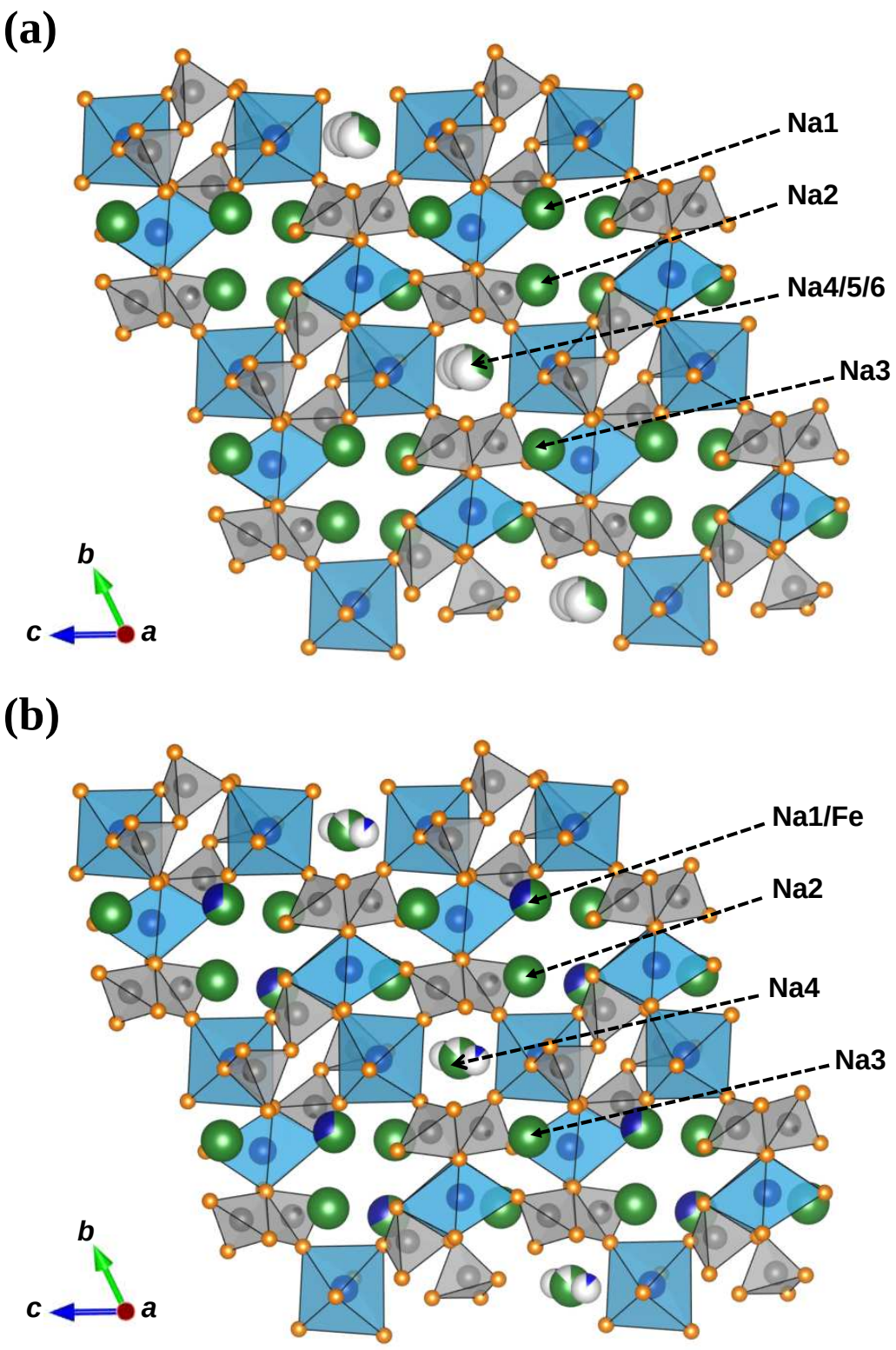

Fig. 6–3 Crystal structures of (a) $Na_2FeP_2O_7$ and (b) $Na_{1.56}Fe_{1.22}P_2O_7$, with FeO_6 and PO_4 polyhedra shown in blue and gray, respectively. Na, Fe, P and O are green, blue, grey and orange, with the shading indicating occupancy.

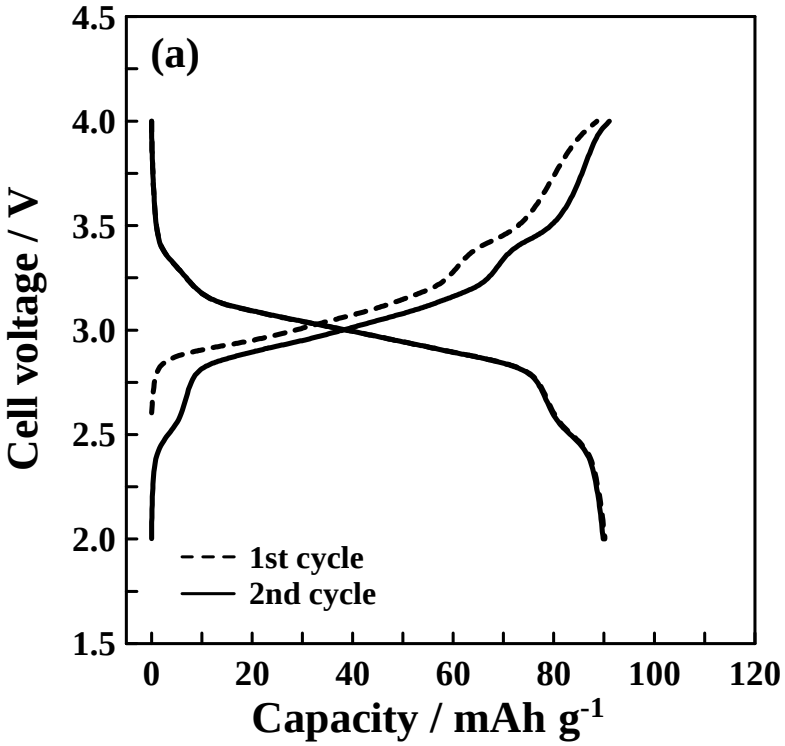
(a)
Cell voltage / V
4.5
4.0
3.5
3.0
2.5
2.0
1.5
0
20
40
60
80
100
120
Capacity / mAh g-1
1st cycle
2nd cycle

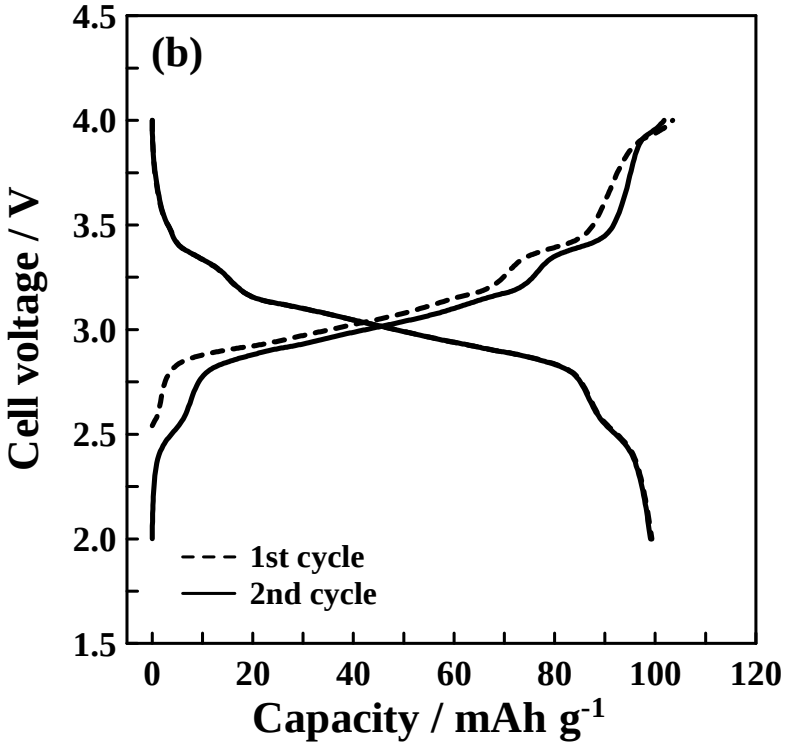
(b)
Cell voltage / V
4.5
4.0
3.5
3.0
2.5
2.0
1.5
0
20
40
60
80
100
120
Capacity / mAh g-1
1st cycle
2nd cycle

(Continued)

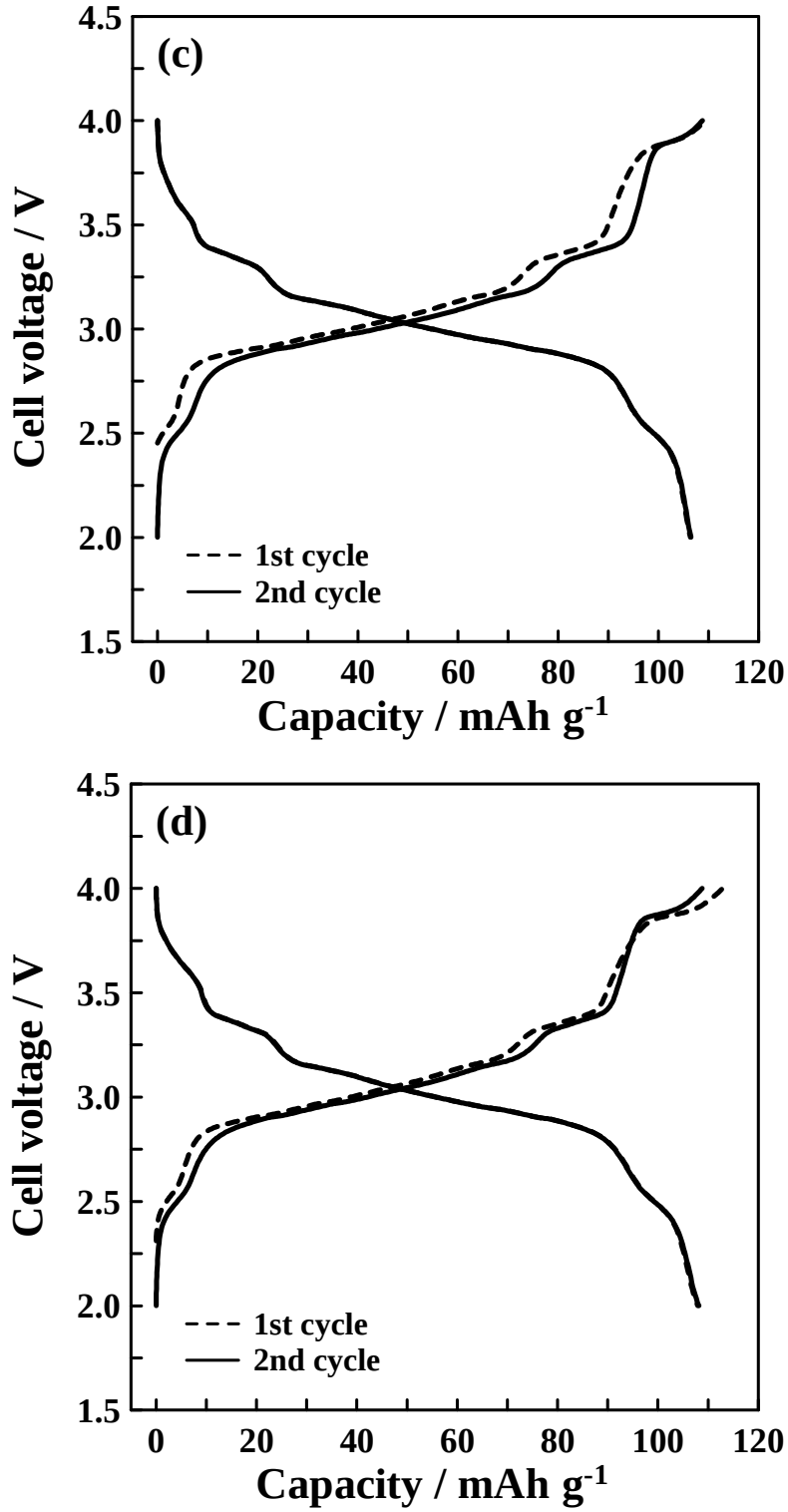

Fig. 6–4 Galvanostatic charge–discharge curves of the initial two cycles for the Na/Na[FSA]–[C_3C_1pyrr][FSA]/$Na_{1.56}Fe_{1.22}P_2O_7$ cell at a current density of 10 mA g^{-1} in the voltage range 2.0–4.0 V at (a) 298 K, (b) 323 K, (c) 348 K and (d) 363 K.

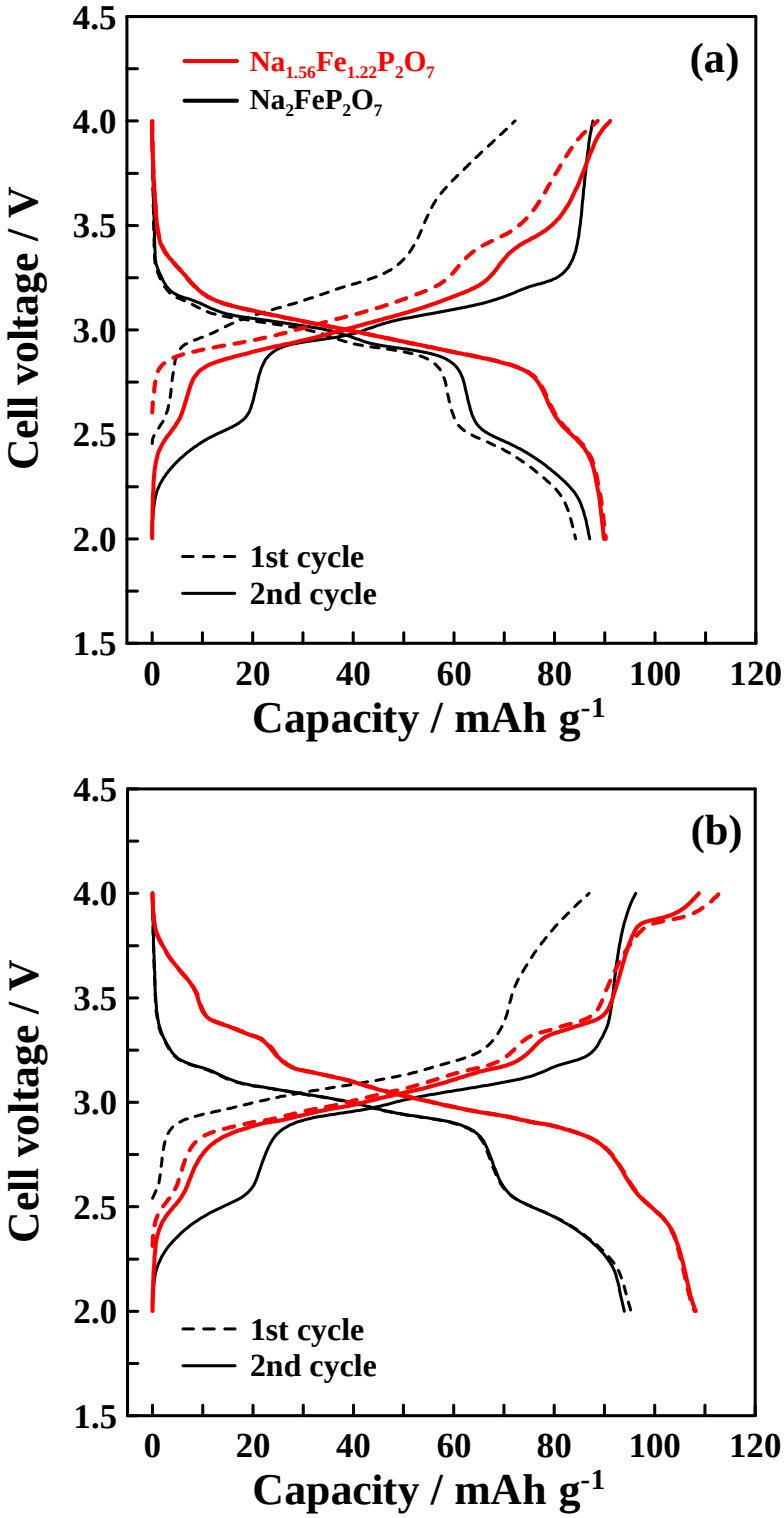

Fig. 6–5 Galvanostatic charge–discharge curves for the Na/Na[FSA]–[C_3C_1pyrr][FSA]/$Na_{2-x}Fe_{1+x/2}P_2O_7$ (x = 0 and 0.44) cell at a current density of 10 mA g^{-1} in the voltage range 2.0–4.0 V at (a) 298 K and (b) 363 K. $Na_{1.56}Fe_{1.22}P_2O_7$: Red line. $Na_2FeP_2O_7$: black line.

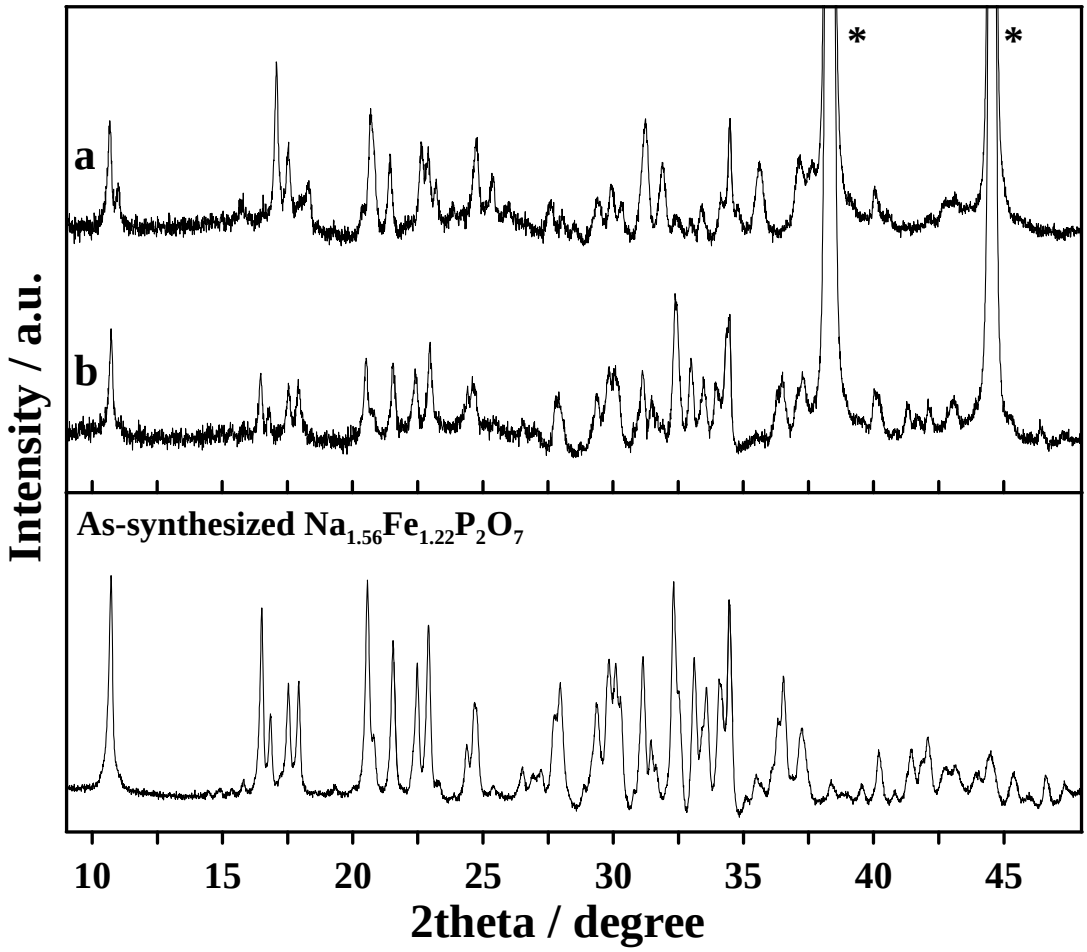

Fig. 6–6 X-ray diffraction patterns of the as-synthesized $Na_{1.56}Fe_{1.22}P_2O_7$, (a) fully charged $Na_xFeP_2O_7$ and (b) fully discharged $Na_{1.56}Fe_{1.22}P_2O_7$. Peaks marked by an asterisk are assigned to the aluminum current collector.

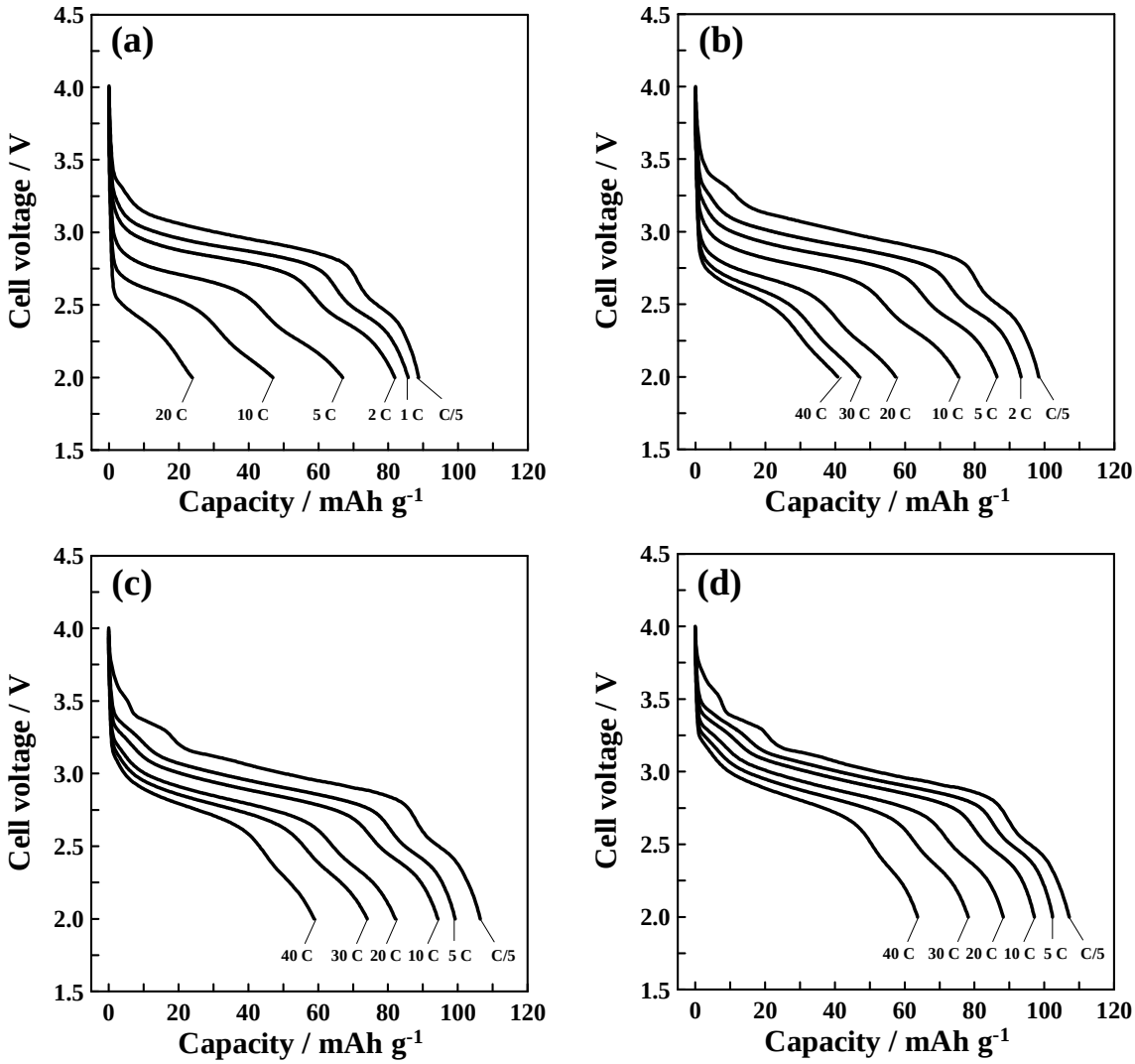

Fig. 6–7 Discharge curves for the Na/Na[FSA]–[C_3C_1pyrr][FSA]/$Na_{1.56}Fe_{1.22}P_2O_7$ cell at various current densities at (a) 298, (b) 323, (c) 348, and (d) 363 K. The cell was charged at C/10 (11.8 mA g^{-1}). Cut-off voltage: 2.0–4.0 V.

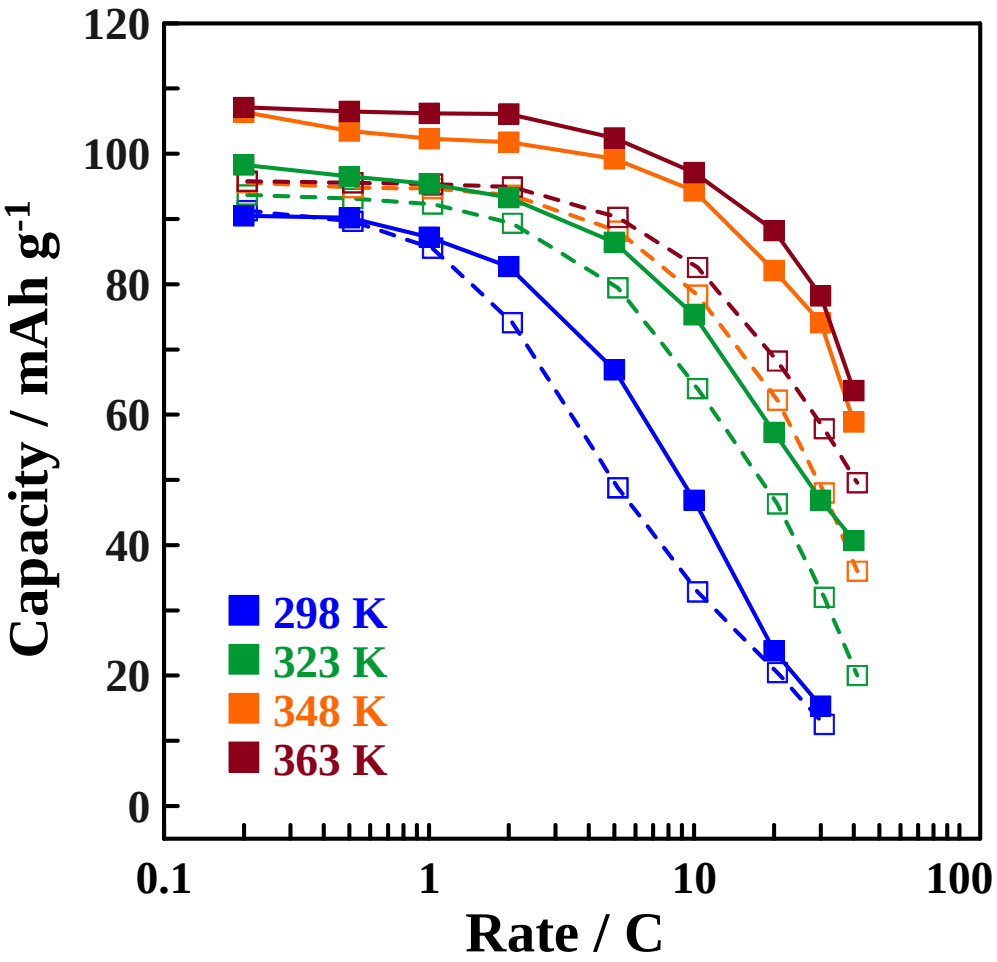

Fig. 6–8 The rate capability of the $Na_{2-x}Fe_{1+x/2}P_2O_7$ (x = 0 and 0.44) positive electrode at 298–363 K. The cell was charged at C/10 (11.8 mA g^{-1}). Cut-off voltage: 2.0–4.0 V. $Na_{1.56}Fe_{1.22}P_2O_7$: solid line and solid mark. $Na_2FeP_2O_7$: dotted line and open mark. The lines connecting the capacity data are only guides to the eye.

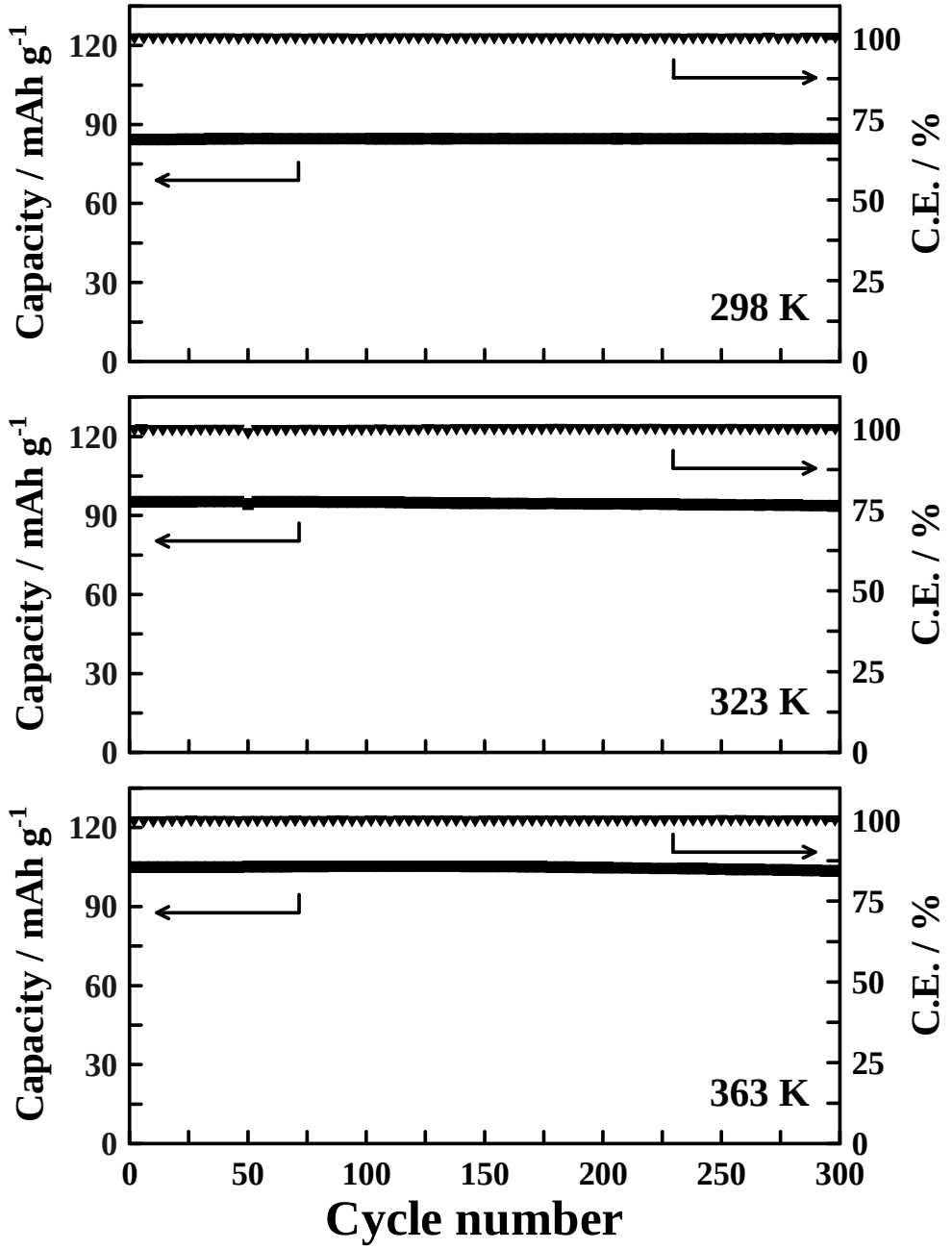

Fig. 6–9 Cycling performance and coulombic efficiency (C.E.) of the $Na_{1.56}Fe_{1.22}P_2O_7$ positive electrode at 298, 323, and 363 K. Cut-off voltage: 2.0–4.0 V. Current density: 1 C (118 mA g^{-1}).

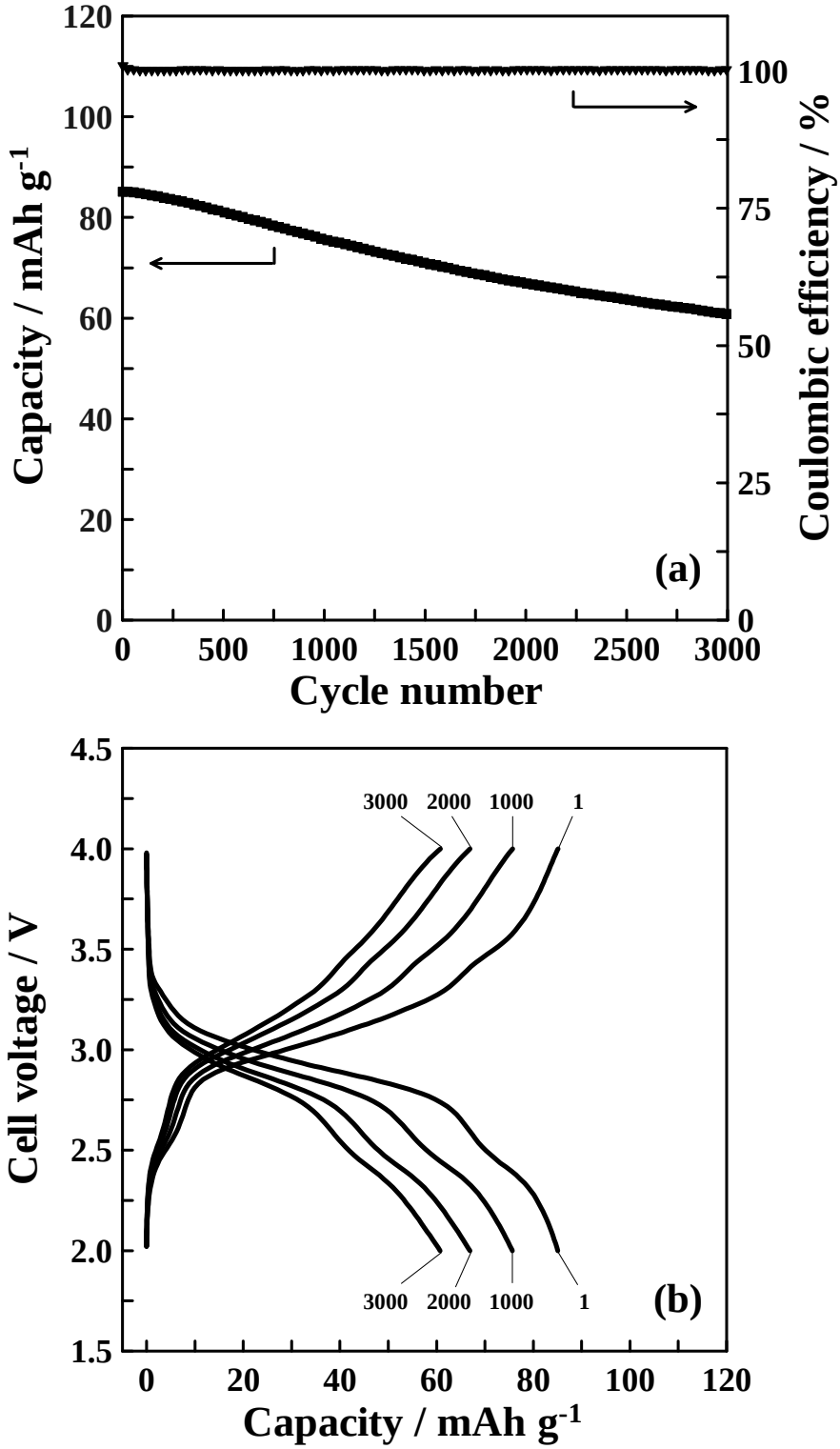

Fig. 6–10 (a) Cycling performance and coulombic efficiency of the $Na_{1.56}Fe_{1.22}P_2O_7$ positive electrode at 363 K. (b) The charge–discharge curves at the 1st, 1000th, 2000th, and 3000th cycle. Cut-off voltage: 2.0–4.0 V. Current density: 20 C (2360 mA g^{-1}).

Chapter 7

Orthosilicate Na_2MnSiO_4 positive electrode in Na[FSA]–[C_3C_1pyrr][FSA]

7.1 Introduction

While interest in Na secondary batteries has grown, many advances need to be done in terms of energy and power density if Na batteries are to be present in future versatile applications [1–3]. Especially, the reversible capacities of positive electrode materials are extremely important in the capacities of full cells [4].

The chemical similarities between Na and Li imply that the heavily studied electrode materials for Li batteries provide the superior library for research on Na batteries [5, 6]. This concept has been explored both experimentally and theoretically [5–12]. As the ionic radius of Na ion (1.02 Å) is 34% larger than that of Li ion (0.76 Å), electrode materials suitable for Li batteries are not always feasible for Na batteries. Due to the open structure and large interstitial space, layered oxides (AMO_2; A = Li, Na; M = transition metal) [7, 8], NASCION (Na-superionic conductors, $A_3M_2(PO_4)_3$) [9, 10] compounds, pyrophosphates ($A_2MP_2O_7$) [11, 12], and phosphate fluorides (A_2MPO_4F) [13, 14] are generally able to accommodate both alkali ions. However, most of these require an improved reversible capacity and/or rate capability. Recently, orthosilicates (A_2MSiO_4) have been proposed as promising Li storage materials due to the low-cost, environmental benignity and excellent safety characteristics [15–19]. Most importantly, they offer the possibility of realizing two-electron exchange per formula leading to a high theoretical capacity of ca. 330 mAh g^{-1}. To my knowledge, however, orthosilicates remains as unexplored Na host matrix.

For Li-ion batteries, orthosilicates of satisfactory electrochemical performance generally necessitate nanosizing and carbon coating to improve their ionic and electronic transport properties [17, 18]. Intermediate-temperature operation (ca. 333 K) is also being pursed to enhance the electrode kinetics [15, 17]. However, safety issues and poor cyclability, owing to volatility and flammability of electrolytes, have been inevitable obstacles [20]. Ionic liquids (ILs) are characterized as task-specific media owing to their nonflammability, good thermal and electrochemical stability [21]. Recent advances have suggested that ILs represents a viable solution to disappointing compromises between energy density and safety features in Li batteries [22]. The unique features make ILs an ideal electrolyte to investigate the electrode performance at moderate and elevated temperatures. For Na battery applications, we have developed a series of ILs based on bis(fluorosulfonyl)amide (FSA) anion [23–25]. Among these, the Na[FSA]–[C_3C_1pyrr][FSA] IL (20:80 molar ratio; C_3C_1pyrr = *N*-methyl-*N*-propylpyrrolidinium) possesses an electrochemical window of 5.2 V and an ionic conductivity of 15.6 mS cm^{-1} at 353 K [25]. Moreover, this IL has been successfully applied to Na batteries in a wide temperature range of 253–363 K [26, 27].

In this chapter, orthosilicate Na_2MnSiO_4 (theoretical capacity of 278 mAh g^{-1} based on a two-electron reaction) was evaluated for its use as a Na storage material for the first time. The Na[FSA]–[C_3C_1pyrr][FSA] IL electrolyte was utilized to exploit its electrochemical behavior from ambient (298 K) to elevated temperatures (363 K). The structural variation upon electrochemical cycling and thermal stability were also investigated.

7.2 Experimental

Sodium manganese orthosilicate Na_2MnSiO_4 was synthesized by a sol-gel method as reported [28]. Sodium acetate (Aldrich, 99.0%) and manganese acetate tetrahydrate (Wako, >99.9%) were dissolved in deionized water and added to a solution of tetraethylorthosilicate

(TEOS) (Aldrich, >99.0%) in ethanol. A proper amount of acetic acid was added to accelerate the hydrolysis of TEOS. The resultant solution was mixed thoroughly for 20 h. After full evaporation of the solvent, the dry powder was ground at room temperature and calcined at 973 K in Ar for 12 h using the tube furnace shown in Chapter 2. Carbon coated Na_2MnSiO_4 (Na_2MnSiO_4/C) was prepared by adding sucrose to the solution before drying. The desodiated form, $Na_{0.8}MnSiO_4$, was prepared by chemical oxidation with nitronium tetrafluoroborate NO_2BF_4 oxidizer (Aldrich, >95%) in acetonitrile (Wako, water content < 50 ppm) at 333 K for 24 h. Since NO_2BF_4 is a strong oxidizing agent with a high redox potential of NO_2^+ / NO_2 at 5.1 V versus Li^+/Li [29], the reaction was carried out in a PFA reactor. The resultant compound was washed several times with fresh acetonitrile in a dry chamber, followed by vacuum-dried at 333 K for 24 h. The content of Na in the desodiated compound was determined by X-ray fluorescence analysis (XRF, Rigaku EDXL 300).

The electrochemical properties of the orthosilicates were assessed using 2032 type coin cells with a Bio-Logic VSP potentiostat as described in Chapter 2. The working electrode was prepared by mixing Na_2MnSiO_4 or Na_2MnSiO_4/C, acetylene black (AB) and polytetrafluoroethylene (PTFE) in a weight ratio of 75:20:5. A metallic sodium disc (Aldrich, purity 99.95%) pressed onto an aluminum current collector was used as the negative electrode. Na[FSA]–[C_3C_1pyrr][FSA] (20:80 molar ratio) IL was used as the electrolyte. The working electrode was impregnated under vacuum with the electrolyte at 333 K for 1 day prior to the test.

7.3 Results and discussion

In a previous study by Duncan *et al*. [28], Na_2MnSiO_4 was prepared and used as the start material to obtain a metastable polymorph of Li_2MnSiO_4 via ion exchanging, because the

latter compound cannot be directly synthesized. I have adopted the same synthetic method of Na_2MnSiO_4. Fig. 7–1 shows the XRD pattern of the obtained sample; the as-prepared material matches the previously known monoclinic phase with the space group *Pn* (PDF No. 00-055-0638), which is consistent to that obtained by Duncan *et al*.. Some impurities, namely MnO and trace amount of Na_2SiO_3, were unavoidably present. The unidentified diffraction peaks may be assigned to another Na_2MnSiO_4 phase that crystallized into a different crystal structure because lithium orthosilicates are known to provide rich polymorphs [30]. Similar kinds of impurity phases were also noticed by other researchers during synthesis of A_2MnSiO_4 (A = Li, Na) by a variety approaches [16, 28, 31–33]. Synthesis of high purity and single phase orthosilicates has been a long-standing goal. It has been speculated that an overlap exists between the stability domains of the main and impurity phases, so isolating an impurity-free Li_2MnSiO_4 is very difficult [33]. Recently, the relative stability of various Li_2FeSiO_4 polymorphs was investigated from first-principles calculations [34]. All of them were shown to have very similar energies, accompanying with many subtle variations between the connectivity of tetrahedral sites occupied by Li^+, Si^{4+}, Fe^{2+}, which explains the difficulties to control the synthesis of single phase Li_2FeSiO_4. For practical utilization of orthosilicates for Na batteries, further optimization of synthesis protocols is required.

A_2MSiO_4 compounds belong to the material genre known as the tetrahedral structures [30, 35]. These structures are based on a distorted hexagonal close-packed array of oxide ions with all cations in distorted corner sharing tetrahedra. The crystal structure of *Pn*-Na_2MnSiO_4 illustrated in Fig. 7–2 have the MnO_4 and SiO_4 tetrahedra, all nearly pointing to the same direction along to the *c* axis, belonging to a non-centrosymmetric space group.

Morphological features of Na_2MnSiO_4 and Na_2MnSiO_4/C are shown in Fig. 7–3. It can be observed that the pristine Na_2MnSiO_4 consists of irregular congregated particles with the particle size of 100–400 nm (Fig. 7–3a), while Na_2MnSiO_4/C exhibits smaller particle size

below 100 nm (Fig. 7–3b). The TEM image shown in Fig. 7–3c illustrates the porous feature of Na_2MnSiO_4/C composite. The HRTEM image indicates that Na_2MnSiO_4 nanoparticles are quite crystalline and coated by a thin layer of amorphous carbon (Fig. 7–3d). Energy dispersive X-ray spectroscopic (EDS) analysis acquired in TEM also confirms the uniform distribution of carbon coating around the Na_2MnSiO_4 particles (Fig. 7–3e). The Brunauer–Emmett–Teller (BET) specific surface area is 4.3 and 29.3 $m^2\ g^{-1}$ for the uncoated Na_2MnSiO_4 and Na_2MnSiO_4/C composite, respectively (Fig. 7–4). The carbon content in the composite is 13.5 wt% according to elemental analysis. During the high temperature calcination, the decomposition of sucrose is accompanied with an evolution of gases that leave sufficient porosity to the final composite, while the carbon coating formed simultaneously with the heat treatment on the surface of Na_2MnSiO_4 inhibits further particle growth. In such architecture, the carbon coating ensures fast paths for electrons while the pores enable good ionic wiring (electrolyte distribution). The latter is particularly important for ILs because they possess a higher viscosity than organic electrolytes [36].

It is generally recognized that a conductive carbon layer is essential to study the electrochemical activity of Li_2MnSiO_4 [28]. It is also true for Na_2MnSiO_4; as can be seen in Fig. 7–5, almost no Na can be extracted from uncoated Na_2MnSiO_4 due to its low electronic conductivity. Typical Nyquist plots of the uncoated and carbon-coated Na_2MnSiO_4 electrodes are shown in Fig. 7–6. Both of them exhibit a semicircle in the high frequency region and a straight line in the low-frequency region. The numerical value of the semicircle diameter on the Z' axis is approximately equal to the charge-transfer resistance (R_{ct}). Results show that the carbon-coated Na_2MnSiO_4 displays apparently lower charge-transfer resistance; a higher electroactivity is thus expectable.

The initial two charge–discharge profiles of the Na_2MnSiO_4/C electrode at a rate of C/10 (13.9 mA g^{-1}) at 298, 323, and 363 K are shown in Fig. 7–7a, b, and c. The first charge curve

with a short voltage plateau region around 3.0 V is distinct from those of the succeeding cycles, wherein only monotonically sloping curves are observed. Reversible capacities of 70, 94 and 125 mAh g^{-1} are obtained for the cell tested at 298, 323 and 363 K, respectively. Approximately 0.9 Na ions per unit formula can be reversibly extracted/inserted from the Na_2MnSiO_4 crystal at 363 K (Fig. 7–7c). Obviously, the alleviation of polarization and increase in capacity are observed with temperature elevation, which can be attributed to enhanced kinetics at elevated temperatures [18]. As shown in Fig. 7–7d, the reversible capacity of the Na_2MnSiO_4/C electrode fades gradually upon cycling. The capacity retention is about 80% at the 10th cycle for all temperatures investigated and further improvement on the cyclability is required for practical application. Nevertheless, considering that lithium orthosilicates generally suffer from a very low rate capability [19, 30], an acceptably high rate capability is observed for the Na_2MnSiO_4/C electrode at 363 K. As shown in Fig. 7–8, the electrode is capable of delivering a capacity of 115, 76 and 34 mAh g^{-1} at 1 C (139 mA g^{-1}), 3 C and 10 C, respectively.

Structural evolution of Na_2MnSiO_4 upon electrochemical cycling was investigated by an ex-situ XRD analysis. As shown in Fig. 7–9, crystalline Na_2MnSiO_4 collapses upon the first charging (Na removal), leaving behind an amorphous phase; furthermore, the diffraction peaks are not recovered during the consecutive discharge (Na insertion). This irreversible structural transformation accounts for the change in the charge–discharge profiles. Although the structural change is significant, the transformed phase can still reversibly accommodate Na ions, as can be seen in Figs. 7–7 and 7–8. For Li_2MnSiO_4, different electrochemical features in the first cycle have also been observed [16, 18, 19, 28] and a strong tendency to become amorphous upon delithiation was confirmed by in-situ XRD analysis and DFT calculations [19, 37]. Furthermore, it was also reported that the electrochemical behavior of two Li_2MnSiO_4 polymorphs differed only during the first cycle [28]. From the viewpoint of

practical application, having a mixture of polymorphs or a single phase orthosilicate for electrode materials appears to be only a minor issue in the present case. Besides, severe capacity fade issues are generally observed for Li_2MnSiO_4 [16–19, 28, 32, 37]. It was speculated that the amorphization of the lattice consequently inhibits re-insertion of Li ions, resulting in the unsatisfactory cyclability [19, 37].

Safety is an essential concern for large-scale battery applications; in particular, good thermal stability of the positive electrode material in the charged (desodiated) state is crucial to realize an intrinsically safe battery. Fig. 7–10 shows the thermogravimetric/differential thermal analytic (TG–DTA) profiles for Na_2MnSiO_4 and its desodiated state ($Na_{0.8}MnSiO_4$) at a heating rate of 5 K min^{-1} under the flow of Ar. During heating up to 773 K, pristine Na_2MnSiO_4 shows negligible weight variation, while the desodiated phase shows a weight loss of 7%. The DTA profiles for both states do not show any noticeable endothermic/exothermic peaks in the same temperature range. Such excellent thermal stability of Na_2MnSiO_4 is comparable to those of other safe positive electrode materials for lithium batteries, including the olivine family that is known to be thermally stable due to the strong P–O bonding. For the pristine state, $LiMnPO_4$ and $LiFePO_4$ were reported to be thermally stable up to 673 K [38, 39]. When comparing in the charged state, the thermal stability of $Na_{0.8}MnSiO_4$ is substantially better than that of $MnPO_4$ (423–473 K) [40] and is comparable to that of $FePO_4$ (773 K) [41]. The superior thermal properties of the orthosilicate will render a safe battery with high tolerance to extreme temperatures.

The present study also demonstrates that ionic liquids can be advantageous electrolytes for intermediate-temperature evaluation of the electrochemical properties of new electrode materials that may otherwise be overlooked. Learning from the strategies proposed for the Li_2MSiO_4 positive electrodes, further reducing of the particle size and improving of the dispersibility [42, 43], tailoring of the electrode architecture or utilizing advanced carbon

substrates [44, 45], can positively improve the electrochemical performance of this material.

7.4 Conclusions

Carbon coated Na_2MnSiO_4 was synthesized by a so-gel method and evaluated for use as a positive electrode material for Na secondary batteries using Na[FSA]–[C_3C_1pyrr][FSA] IL in the temperature range 298–363 K. A reversible capacity of 125 mAh g^{-1} with an acceptably high rate capability was achieved at 363 K. Although issues that include increasing the sample purity or improving the cyclability should be addressed prior to practical applications, this is the first practical demonstration of an orthosilicate electrode material for Na batteries. The low cost, high theoretical capacity, and remarkable thermal stability allow Na_2MnSiO_4 to potentially serve as a positive electrode material. Further exploration of Na_2MSiO_4 (M = Fe, Co, Ni, and Ti) materials may offer new opportunities to make substantial improvements in capacity, voltage, and cyclability of positive electrodes for Na secondary batteries.

References

[1] S.W. Kim, D.H. Seo, X.H. Ma, G. Ceder, K. Kang, Adv. Energy Mater. 2 (2012) 710–721.

[2] V. Palomares, M. Casas-Cabanas, E. Castillo-Martinez, M.H. Han, T. Rojo, Energy Environ. Sci. 6 (2013) 2312–2337.

[3] H.L. Pan, Y.S. Hu, L.Q. Chen, Energy Environ. Sci. 6 (2013) 2338–2360.

[4] Z.L. Jian, H.J. Yu, H.S. Zhou, Electrochem. Commun. 34 (2013) 215–218.

[5] S.Y. Hong, Y. Kim, Y. Park, A. Choi, N.S. Choi, K.T. Lee, Energy Environ. Sci. 6 (2013) 2067–2081.

[6] S.P. Ong, V.L. Chevrier, G. Hautier, A. Jain, C. Moore, S. Kim, X.H. Ma, G. Ceder, Energy Environ. Sci. 4 (2011) 3680–3688.

[7] K. Mizushima, P.C. Jones, P.J. Wiseman, J.B. Goodenough, Mater. Res. Bull. 15 (1980) 783–789.

[8] R. Berthelot, D. Carlier, C. Delmas, Nat. Mater. 10 (2011) 74–80.

[9] J. Gaubicher, C. Wurm, G. Goward, C. Masquelier, L. Nazar, Chem. Mater. 12 (2000) 3240–3242.

[10] Z.L. Jian, L. Zhao, H.L. Pan, Y.S. Hu, H. Li, W. Chen, L.Q. Chen, Electrochem. Commun. 14 (2012) 86–89.

[11] S. Nishimura, M. Nakamura, R. Natsui, A. Yamada, J. Am. Chem. Soc. 132 (2010) 13596–13597.

[12] P. Barpanda, T. Ye, S. Nishimura, S.C. Chung, Y. Yamada, M. Okubo, H.S. Zhou, A. Yamada, Electrochem. Commun. 24 (2012) 116–119.

[13] J. Barker, R.K.B. Gover, P. Burns, A. Bryan, Electrochem. Solid-State Lett. 8 (2005) A285–A287.

[14] B.L. Ellis, W.R.M. Makahnouk, Y. Makimura, K. Toghill, L.F. Nazar, Nat. Mater. 6 (2007) 749–753.

[15] A. Nyten, A. Abouimrane, M. Armand, T. Gustafsson, J.O. Thomas, Electrochem. Commun. 7 (2005) 156–160.

[16] R. Dominko, M. Bele, M. Gaberscek, A. Meden, M. Remskar, J. Jamnik, Electrochem. Commun. 8 (2006) 217–222.

[17] Z.L. Gong, Y.X. Li, Y. Yang, Electrochem. Solid State Lett. 9 (2006) A542–A544.

[18] T. Muraliganth, K.R. Stroukoff, A. Manthiram, Chem. Mater. 22 (2010) 5754–5761.

[19] R. Dominko, J. Power Sources 184 (2008) 462–468.

[20] D. Aurbach, Y. Talyosef, B. Markovsky, E. Markevich, E. Zinigrad, L. Asraf, J.S. Gnanaraj, H.J. Kim, Electrochim. Acta 50 (2004) 247–254.

[21] M. Armand, F. Endres, D.R. MacFarlane, H. Ohno, B. Scrosati, Nat. Mater. 8 (2009) 621–629.

[22] M.A. Navarra, MRS Bull. 38 (2013) 548–553.

[23] K. Kubota, T. Nohira, T. Goto, R. Hagiwara, Electrochem. Commun. 10 (2008) 1886–1888.

[24] A. Fukunaga, T. Nohira, Y. Kozawa, R. Hagiwara, S. Sakai, K. Nitta, S. Inazawa, J. Power Sources 209 (2012) 52–56.

[25] C.S. Ding, T. Nohira, K. Kuroda, R. Hagiwara, A. Fukunaga, S. Sakai, K. Nitta, S. Inazawa, J. Power Sources 238 (2013) 296–300.

[26] C.Y. Chen, K. Matsumoto, T. Nohira, C.S. Ding, T. Yamamoto, R. Hagiwara, Electrochim. Acta 133 (2014) 583–588.

[27] C.S. Ding, T. Nohira, R. Hagiwara, K. Matsumoto, Y. Okamoto, A. Fukunaga, S. Sakai, K. Nitta, S. Inazawa, J. Power Sources 269 (2014) 124–128.

[28] H. Duncan, A. Kondamreddy, P.H.J. Mercier, Y. Le Page, Y. Abu-Lebdeh, M. Couillard, P.S. Whitfield, I.J. Davidson, Chem. Mater. 23 (2011) 5446–5456.

[29] A.R. Wizansky, P.E. Rauch, F.J. Disalvo, J. Solid State Chem. 174 (1989) 203–207.

[30] M.S. Islam, R. Dominko, C. Masquelier, C. Sirisopanaporn, A.R. Armstrong, P.G. Bruce, J. Mater. Chem. 21 (2011) 9811–9818.

[31] M.E. Arroyo-DeDompablo, R. Dominko, J.M. Gallardo-Amores, L. Dupont, G. Mali, H. Ehrenberg, J. Jamnik, E. Moran, Chem. Mater. 20 (2008) 5574–5584.

[32] V. Aravindan, K. Karthikeyan, K.S. Kang, W.S. Yoon, W.S. Kim, Y.S. Lee, J. Mater. Chem. 21 (2011) 2470–2475.

[33] I. Belharouak, A. Abouimrane, K. Amine, J. Phys. Chem. C 113 (2009) 20733–20737.

[34] A. Saracibar, A. Van der Ven, M.E. Arroyo-de Dompablo, Chem. Mater. 24 (2012) 495–503.

[35] C.A.J. Fisher, N. Kuganathan, M.S. Islam, J. Mater. Chem. A 1 (2013) 4207–4214.

[36] M. Nadherna, R. Dominko, D. Hanzel, J. Reiter, M. Gaberscek, J. Electrochem. Soc., 156 (2009) A619–A626.

[37] A. Kokalj, R. Dominko, G. Mali, A. Meden, M. Gaberscek, J. Jamnik, Chem. Mater. 19 (2007) 3633–3640.

[38] S.W. Kim, J. Kim, H. Gwon, K. Kang, J. Electrochem. Soc. 156 (2009) A635–A638.

[39] J.L. Dodd, R. Yazami, B. Fultz, Electrochem. Solid State Lett. 9 (2006) A151–A155.

[40] S.P. Ong, A. Jain, G. Hautier, B. Kang, G. Ceder, Electrochem. Commun. 12 (2010) 427–430.

[41] C. Delacourt, P. Poizot, J.M. Tarascon, C. Masquelier, Nat. Mater. 4 (2005) 254–260.

[42] D. Rangappa, K.D. Murukanahally, T. Tomai, A. Unemoto, I. Honma, Nano Lett. 12 (20012) 1146–1151.

[43] Z. Hu, K. Zhang, H.Y. Gao, W.C. Duan, F.Y. Cheng, J. Liang, J. Chen, J. Mater. Chem. A 1 (2013) 12650–12656.

[44] Y. Zhao, J.X. Li, N. Wang, C.X. Wu, Y.H. Ding, L.H. Guan, J. Mater. Chem. 22 (2012) 18797–18800.

[45] Y. Zhao, C.X. Wu, J.X. Li, L.H. Guan, J. Mater. Chem. A 1 (2013) 3856–3859.

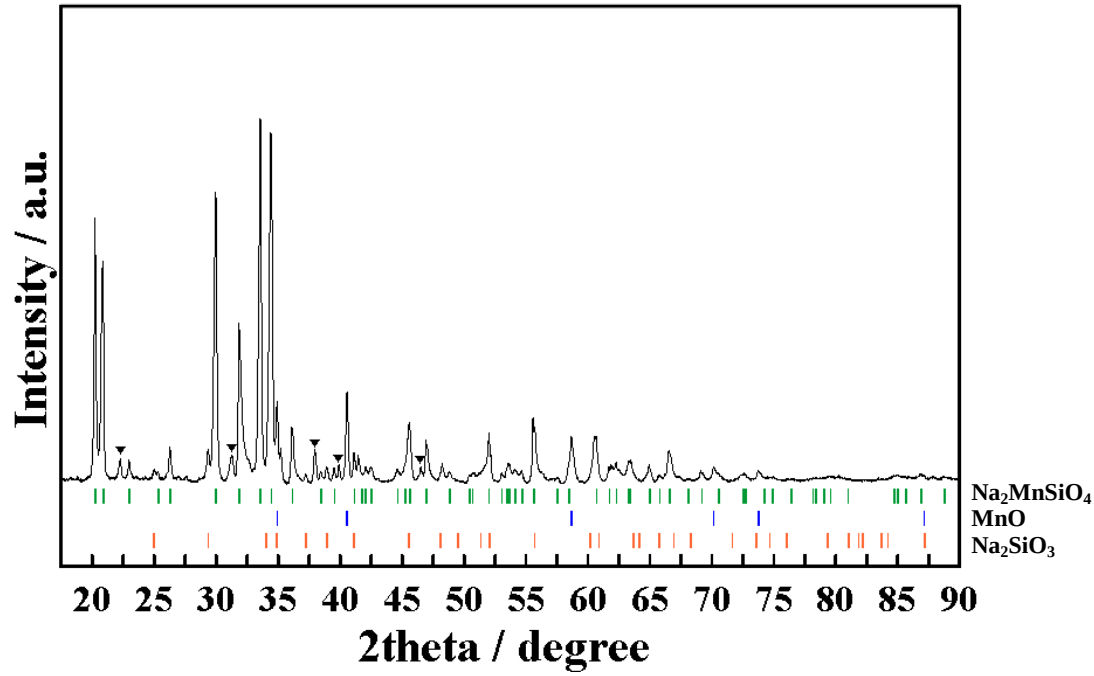

Fig. 7–1 XRD patterns of pristine Na_2MnSiO_4. Bragg diffraction positions for the parent phase (green ticks for Na_2MnSiO_4) and impurities (blue ticks for MnO and orange ticks for Na_2SiO_3) are shown. Triangles represent unidentified peaks.

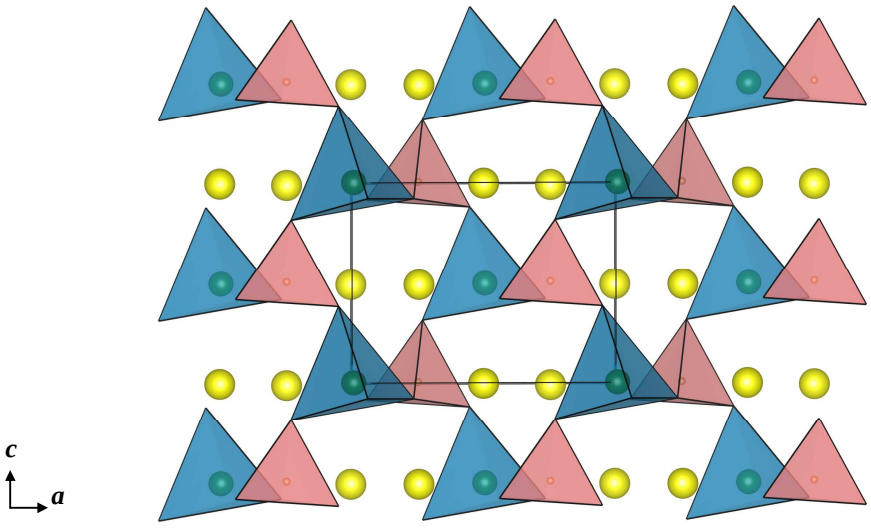

Fig. 7–2 A representative illustration of the crystal structure showing an arrangement of MnO_4 (blue) and SiO_4 (pink) tetrahedra together with Na ions (yellow).

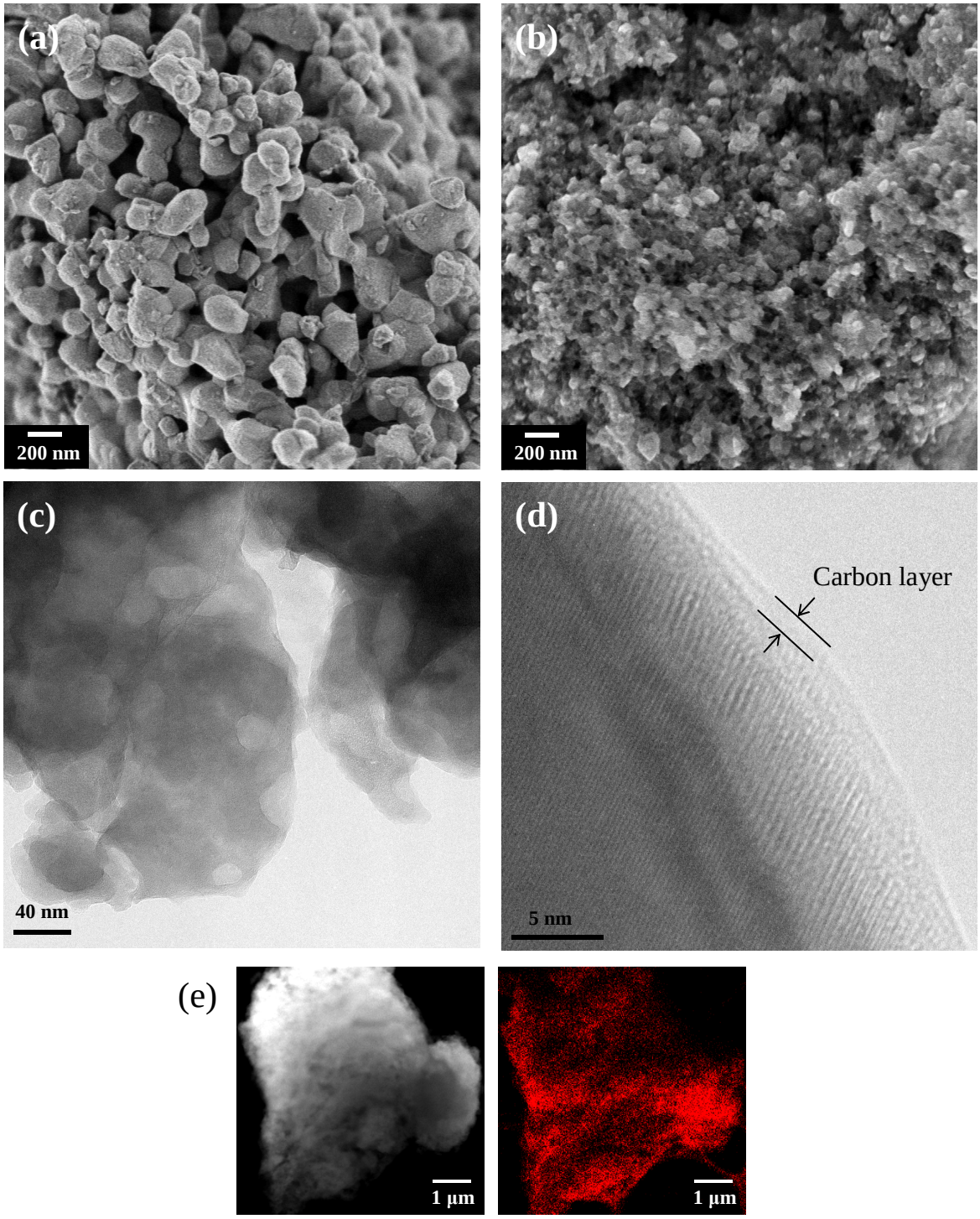

Fig. 7–3 SEM images of (a) Na_2MnSiO_4 and (b) Na_2MnSiO_4/C. TEM images of Na_2MnSiO_4/C are shown in (c) and (d). (e) Carbon mapping of Na_2MnSiO_4/C by energy dispersive X-ray spectroscopy.

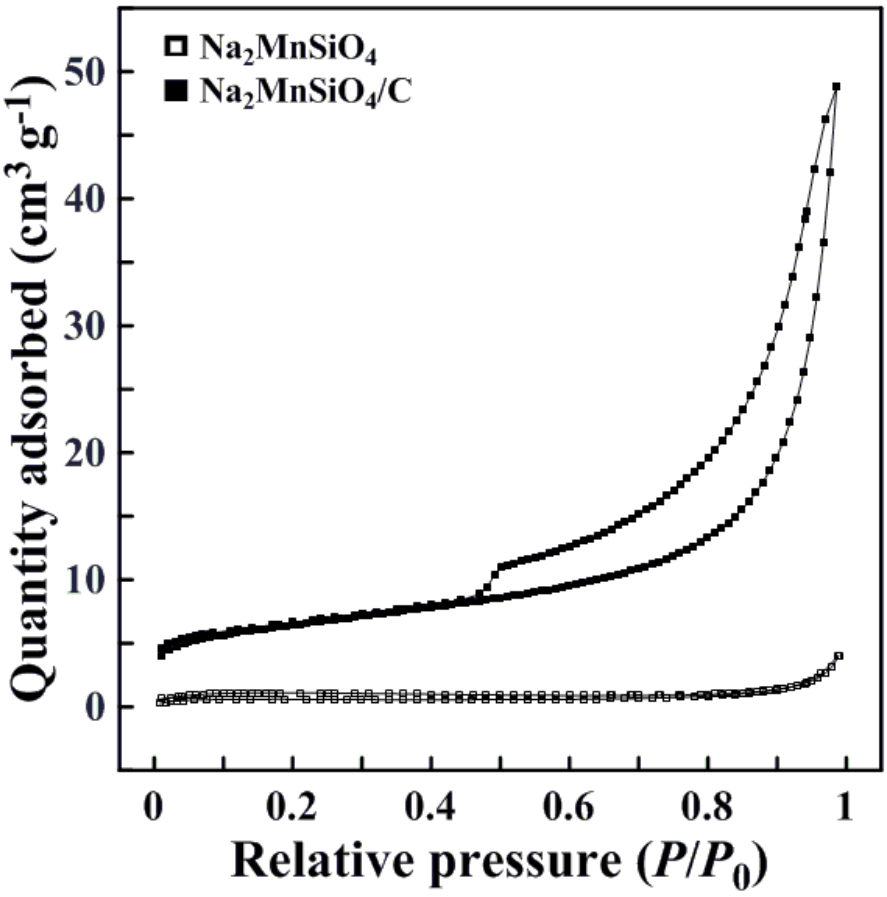

Fig. 7–4 Nitrogen adsorption and desorption isotherms at 77 K for the pristine and carbon-coated Na_2MnSiO_4.

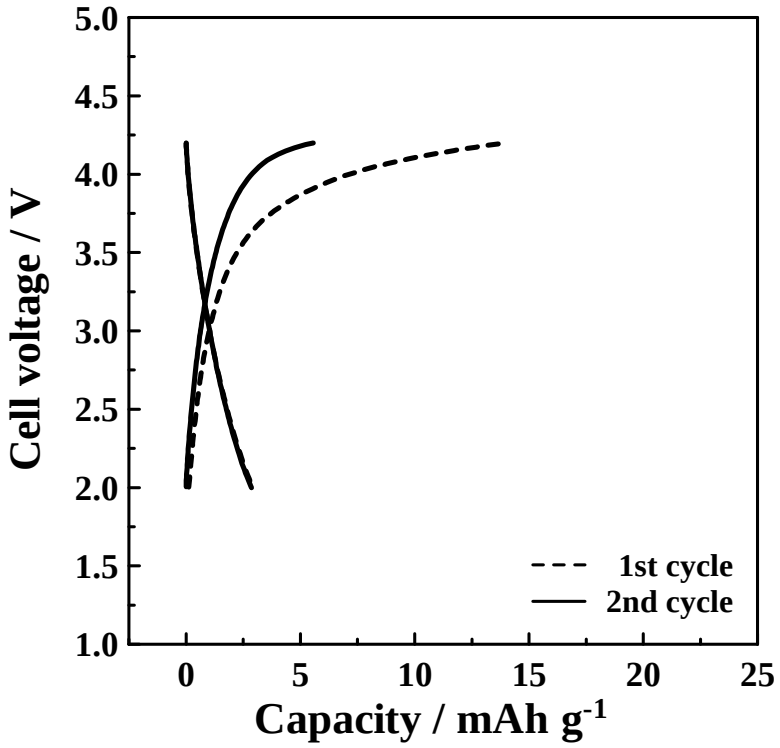

Fig. 7–5 Galvanostatic charge–discharge curves of the initial two cycles for the Na/Na[FSA]–[C_3C_1pyrr][FSA]/Na_2MnSiO_4 cell at 10 mA g^{-1} in the voltage range of 2.0–4.2 V at 298 K.

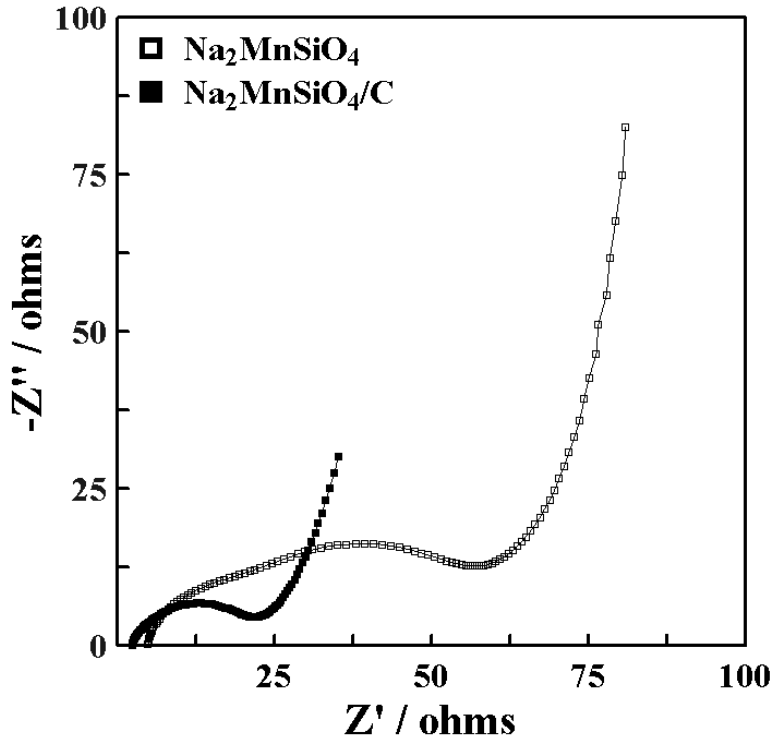

Fig. 7–6 Nyquist plots for the uncoated and carbon-coated Na_2MnSiO_4 electrodes measured at 363 K. The AC perturbation was 10 mV, and the frequency range was from 200 kHz to 2 Hz.

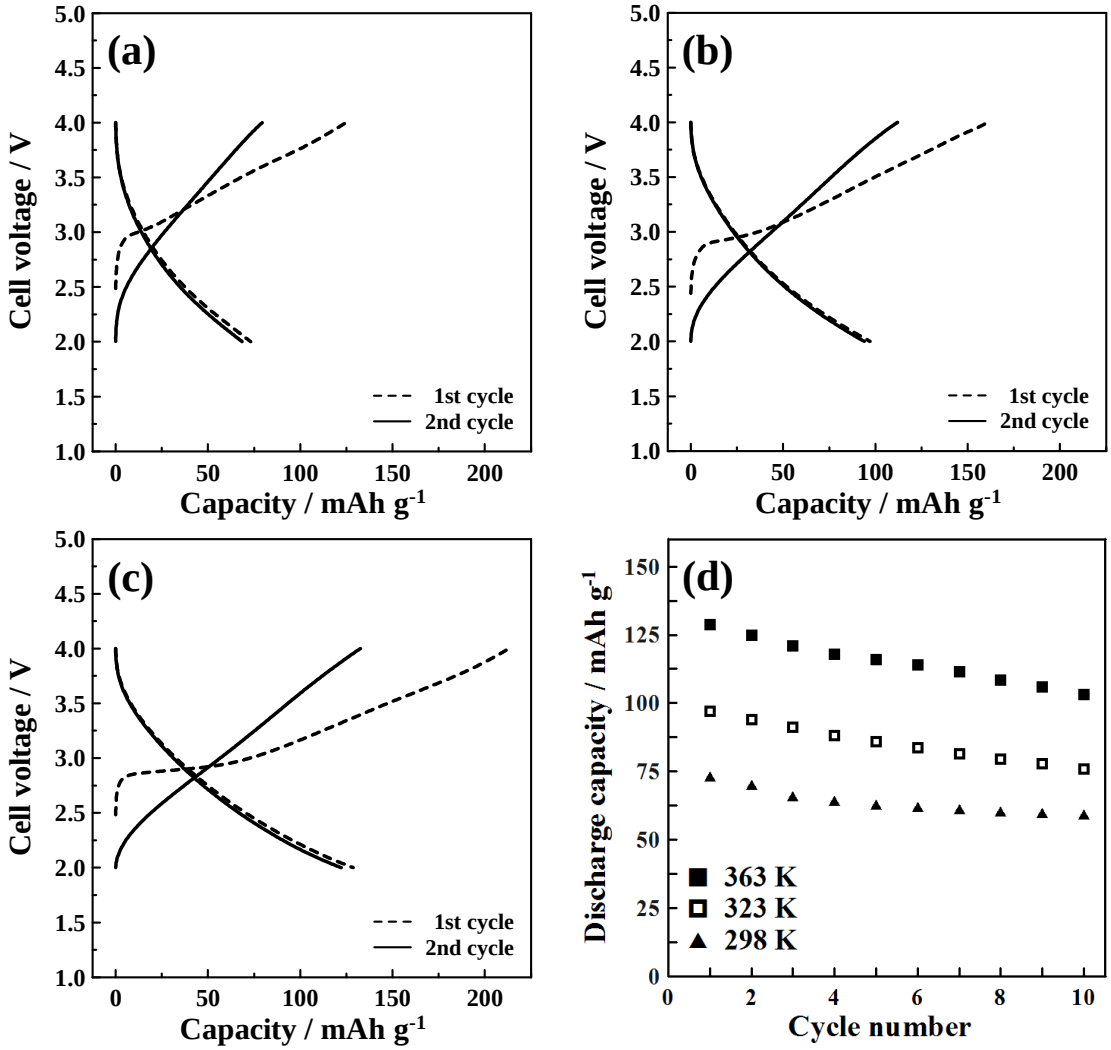

Fig. 7–7 Galvanostatic charge–discharge curves of the initial two cycles for the Na/Na[FSA]–[C_3C_1pyrr][FSA]/Na_2MnSiO_4/C cell at C/10 (13.9 mA g^{-1}) in the voltage range of 2.0–4.0 V at (a) 298 K, (b) 323 K and (c) 363 K. (d) Cycling performance of the Na_2MnSiO_4/C electrode at 298, 323 and 363 K.

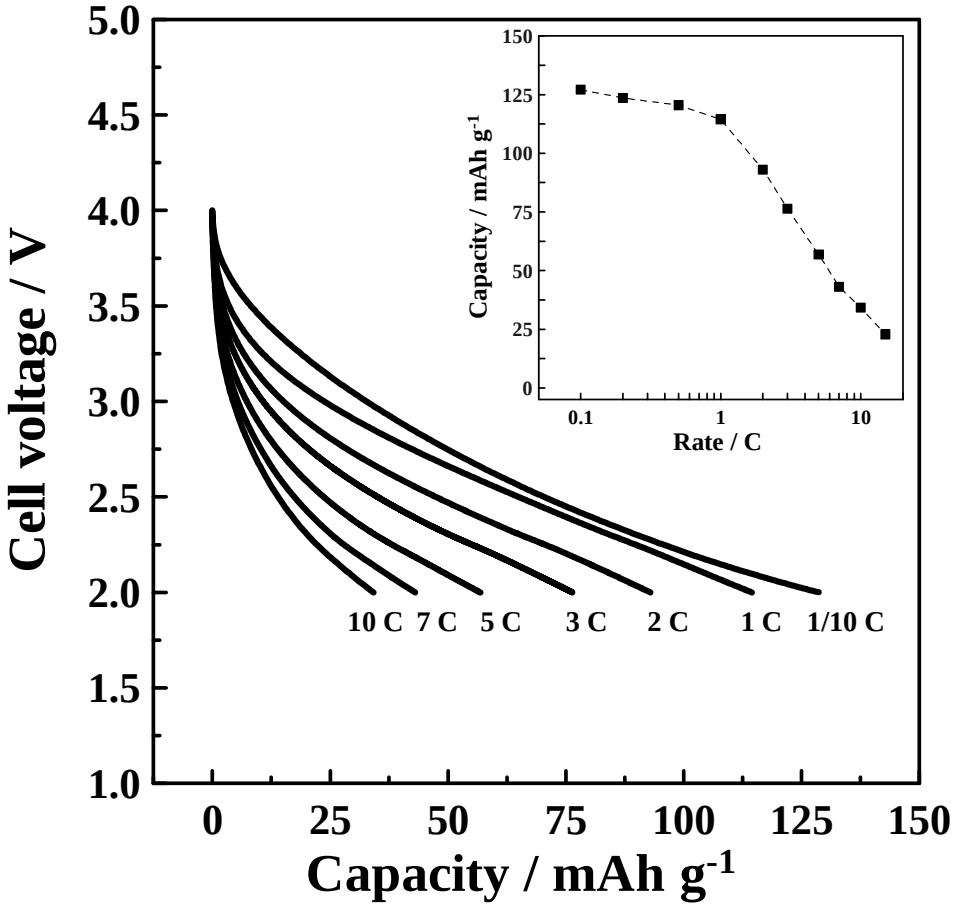

Fig. 7–8 Discharge curves of the Na_2MnSiO_4/C positive electrode at various current densities at 363 K. The cells were charged to 4.0 V at constant rate of C/10 and were kept for 2 h before discharging at different rates to 2.0 V. (Inset) The capacity as a function of rate.

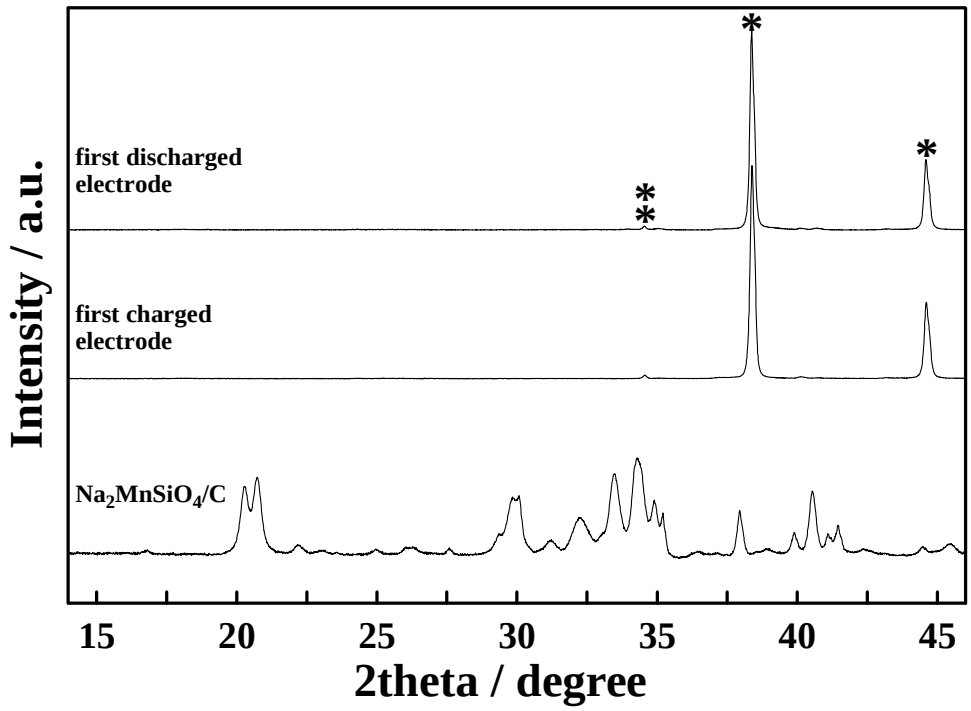

Fig. 7–9 XRD patterns of Na_2MnSiO_4/C, first charged, and first discharged electrodes. Peaks marked by asterisks (*) are assigned to the aluminum current collector including Kβ peaks (**).

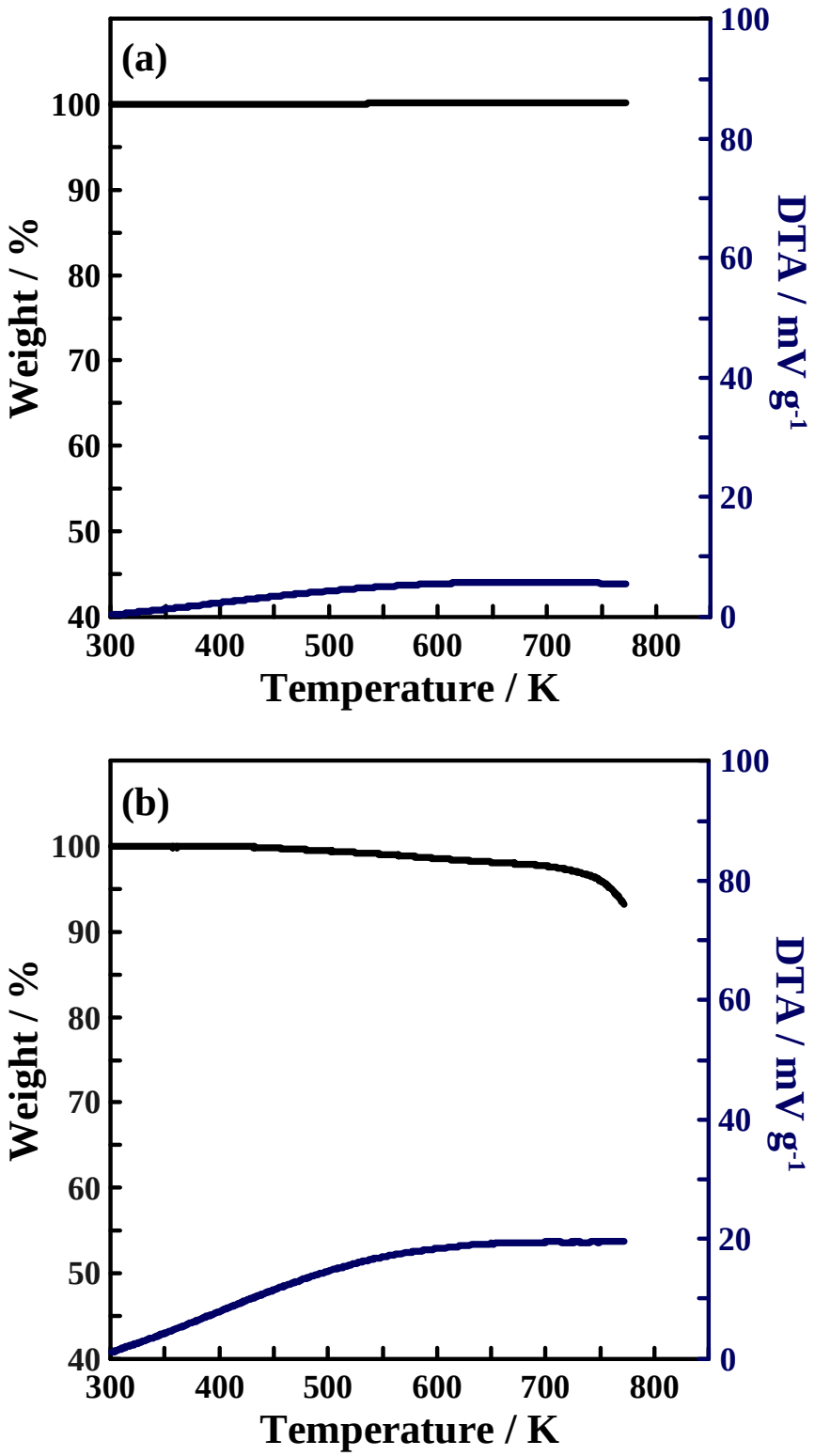

Fig. 7–10 Thermal analysis (TG-DTA) curves for (a) the pristine Na_2MnSiO_4 and (b) the desodiated state $Na_{0.8}MnSiO_4$ at a heating rate of 5 K min^{-1} under Ar flow. $Na_{0.8}MnSiO_4$ was prepared by chemical oxidation of Na_2MnSiO_4.

Chapter 8

General conclusions

Reports on the processing, properties, and applications associated with Na secondary batteries are appearing rapidly on a daily basis. However, Na secondary batteries are still in their germination stage now and major efforts have focused on studies at ambient temperature. Many forthcoming energy storage devices are expected to be used under extreme operating environments including elevated temperature. In such circumstances, ionic liquid (IL) electrolytes of thermal and chemical stability are attractive for developing high-power and safe batteries. Besides, to make Na secondary batteries more economically accessible, polyanion systems that focus on Fe and Mn are the most desirable from raw material cost perspective. Bearing these considerations in mind, the author have synthesized layered oxide and polyanionic-type positive electrode materials and investigated their properties in IL electrolytes for Na secondary battery applications.

In Chapter 3, the charge–discharge behavior and phase transition of layered oxide $NaCrO_2$ have been investigated in the Na[FSA]–K[FSA] IL at 363 K. When compared with the previous reports for the same material tested in an organic electrolyte at room temperature (RT), the results reveal that both kinetics and cyclability of the Na intercalation/deintercalation processes are largely improved. The desodiation of $NaCrO_2$ proceeds with the phase transition in the following sequence: hexagonal O3 → monoclinic O’3 → monoclinic P’3, which is in agreement with those observed at RT. Nevertheless, phase transitions takes place more easily at high temperature than RT. In this chapter, the advantages of intermediate temperature operation have been demonstrated. It is also confirmed that the Na[FSA]–K[FSA] IL is a promising electrolyte of choice for this purpose.

In Chapter 4, the charge–discharge behavior of a polyanionic compound $Na_2FeP_2O_7$ has been evaluated in the Na[FSA]–K[FSA] IL at 363 K. The mechanism of Na extraction from $Na_2FeP_2O_7$ has been also studied by ex-situ X-ray absorption spectroscopy (XAS). Good rate capability (59 mAh g^{-1} at 2000 mA g^{-1}) and capacity retention of 75% over 3000 cycles are observed. XAS studies confirm that the Fe oxidation state reversibly changes upon electrochemical cycling accompanying a variation of Fe–O bond length. This chapter confirms the feasibility of combining economic positive electrode materials built from abundant elements with a safe IL electrolyte.

In Chapter 5, the charge–discharge behavior of polyanionic compound $Na_2FeP_2O_7$ has been evaluated in the Na[FSA]–[C_3C_1pyrr][FSA] IL in a wide temperature range of 253–363 K. The temperature dependence of the rate capability and cyclability has been also studied. A stable charge–discharge behavior is obtained over 253–363 K. The rate capability is considerably improved with increasing temperature, delivering 50 mAh g^{-1} even at a high rate of 4000 mA g^{-1} at 363 K. Furthermore, the $Na_2FeP_2O_7$ positive electrode demonstrates an satisfactory cyclability exceeding 300 cycles in terms of both capacity retention and coulombic efficiency at 298–363 K. The results obtained in this chapter demonstrate that the operating temperature range of Na secondary batteries can be effectively extended by utilizing a suitable electrolyte such as the Na[FSA]–[C_3C_1pyrr][FSA] IL.

In Chapter 6, the charge–discharge behavior of $Na_{1.56}Fe_{1.22}P_2O_7$ has been investigated in the Na[FSA]–[C_3C_1pyrr][FSA] IL at 298–363 K and compared with that of $Na_2FeP_2O_7$. By altering the Na/Fe stoichiometric ratio, $Na_{1.56}Fe_{1.22}P_2O_7$ exhibits a reversible capacity of 108 mAh g^{-1} at 363 K, which is 15% improvement compared with that of $Na_2FeP_2O_7$ at the same condition. Furthermore, a satisfactory cyclability (*ca*. 99% capacity retention after 300 cycles) is observed at 298–363 K, which can be attributed to both the small volume change upon cycling and the chemical stability of the IL electrolyte. This chapter demonstrates that

enhanced performance of polyanion-type electrodes can be achieved by optimizing the composition of the material.

In Chapter 7, the charge–discharge behavior of polyanionic compound Na_2MnSiO_4 has been investigated in the Na[FSA]–[C_3C_1pyrr][FSA] at 298–363 K. Using the same strategy of Li secondary batteries, carbon coating and elevation of operation temperature successfully improve the electrode performance. A reversible capacity of 125 mAh g^{-1} is achieved with an acceptably high rate capability at 363 K. Both Na_2MnSiO_4 and its desodiated form ($Na_{0.8}MnSiO_4$) possess remarkable thermal stability, suggesting their highly safe characteristic. This chapter demonstrates how technology developed initially for Li secondary batteries can be leveraged for rapid deployment of the Na analogs.

Generally, common knowledge learned from LIBs are applicable when designing and understating Na secondary batteries. It is considered that low-strain materials such as pyrophosphates will play an important role for realizing Na secondary batteries of ultra-long lifetime and low maintenance cost. It is also expected that IL electrolytes will show their high performances in the post Li-ion battery era, towards sustainable and versatile energy storage applications.

List of publications

Chapter 3

Chih–Yao Chen, Kazuhiko Matsumoto, Toshiyuki Nohira, Rika Hagiwara, Atsushi Fukunaga, Shoichiro Sakai, Koji Nitta, Shinji Inazawa

Journal of Power Sources 237 (2013) 52–57.

“Electrochemical and structural investigation of $NaCrO_2$ as a positive electrode for sodium secondary battery using inorganic ionic liquid NaFSA–KFSA”

Chapter 4

Chih–Yao Chen, Kazuhiko Matsumoto, Toshiyuki Nohira, Rika Hagiwara, Yuki Orikasa, Yoshiharu Uchimoto

Journal of Power Sources 246 (2014) 783–787.

“Pyrophosphate $Na_2FeP_2O_7$ as a low-cost and high-performance positive electrode material for sodium secondary batteries utilizing an inorganic ionic liquid”

Chapter 5

Chih–Yao Chen, Kazuhiko Matsumoto, Toshiyuki Nohira, Changsheng Ding, Takayuki Yamamoto, Rika Hagiwara

Electrochimica Acta 133 (2014) 583–588.

“Charge–discharge behavior of a $Na_2FeP_2O_7$ positive electrode in an ionic liquid electrolyte between 253 and 363 K”

Chapter 6

Chih–Yao Chen, Kazuhiko Matsumoto, Toshiyuki Nohira, Rika Hagiwara

Submitted.

“Full utilization of the intrinsic charge–discharge characteristics of a $Na_{1.56}Fe_{1.22}P_2O_7$ positive electrode by using an ionic liquid electrolyte”

Chapter 7

Chih–Yao Chen, Kazuhiko Matsumoto, Toshiyuki Nohira, Rika Hagiwara

Electrochemistry Communications 45 (2014) 63–66.

“Na_2MnSiO_4 as a positive electrode material for sodium secondary batteries using an ionic liquid electrolyte”

Acknowledgement

I would like to express my deepest gratitude to Professor Rika Hagiwara for allowing me to study under his supervision. The invaluable support, guidance and freedom he gave me throughout this study have been a true blessing. I am sincerely grateful to Associate Professor Toshiyuki Nohira for his enlightening instructions, constant encouragement and fruitful discussions. I would like to extend my heartfelt appreciation to Assistant Professor Kazuhiko Matsumoto. Without his immeasurable amount of coherent guidance and hearty encouragement, this thesis would not have reached its present form. I am grateful to Assistant Professor Kouji Yasuda for his educational instructions and helpful advices. I am also grateful to Assistant Professors Changsheng Ding and Xiao Yang for their kind assistance.

Special thanks are given to Professors Takashi Sagawa and Tetsuji Hirato for the fruitful discussions and suggestions.

I would like to thank Professor Yoshiharu Uchimoto and Assistant Professor Yuki Orikasa for the fruitful discussion on X-ray absorption spectroscopy.

Special thanks are given to Ms. Hisami Okuda, Ms. Naoko Sakamoto, Ms. Hiroko Kitayama, Ms. Yuko Yamamura, Ms. Keiko Ema, Mr. Junichi Imaru, Ms. Hitomi Arai and Ms. Rie Deguchi for their various helps and heedful care. I must express my appreciation to all the present and former members in Energy Chemistry Laboratory. They make my stay in Japan enjoyable and unforgettable, no matter good or bad times. Especially, Dr. Fei Xu, Dr. Ryosuke Taniki and Mr. Takayuki Yamamoto have not only taught a lot about the experimental methods but also provided countless assistance in my daily life.

I wish to express my sincere appreciation to the Yoshida Scholarship Foundation for their financial support for my living in Japan.

I want to thank all my friends and family for their encouragement. Their devoted love

and unfailing support are the real strength behind my accomplishments. Not all acknowledgements are described here and I thank all related to this study.

Chih–Yao Chen

August 2014